

# **Simulation of Topological Transport of Colloidal Particle Assemblies above Magnetic Patterns**

Von der Universität Bayreuth  
zur Erlangung des Grades eines  
Doktors der Naturwissenschaften (Dr. rer. nat.)  
genehmigte Abhandlung

von

**Adrian Friedo Ernst**

aus Hof

1. Gutachter: Prof. Dr. Thomas Fischer

2. Gutachter: Prof. Dr. Werner Köhler

Tag der Einreichung: 15.12.2022

Tag des Kolloquiums: 09.03.2023



## Abstract

This cumulative thesis studies the topological transport of colloidal particles subject to an external magnetic field that changes its direction along a loop. The paramagnetic colloidal particles respond by moving on top of periodic magnetic patterns. I investigate five physical questions for various different situations using Brownian Dynamics simulations. The simulations are corroborated by experiments from other members in my group. I show how to build an adiabatic topologically protected discrete time crystal with three colloidal particles that interact via dipolar interactions and reside on a flower shaped periodic pattern. I extend this motive to various space time crystalline structures. I discuss the difference between a topologically protected and a geometric form of transport. I show how the transport changes from topological toward geometrical as a function of the particle number in an ensemble of several colloidal particles per unit cell. Dipolar interactions enforce the assembly of  $n$  colloidal particles into a biped. I developed a topological protected polyglot programming of the biped walking on square patterns that lets bipeds of different length simultaneously walk into different predefined directions. I analyze the walking on square and hexagonal patterns with the center of mass gauge and the instantaneous center of rotation gauge, which allows me to decompose the motion into passive and active components. Finally at non-adiabatic speeds of driving I show how hydrodynamic interaction suppresses passive motion, stalls single colloidal particles unless still active bipeds assist their passive motion.



# Kurzdarstellung

Diese kumulative Dissertation untersucht den topologischen Transport von kolloidalen Teilchen, die einem externen Magnetfeld ausgesetzt sind, das seine Richtung entlang einer Schleife ändert. Die paramagnetischen kolloidalen Teilchen reagieren darauf, indem sie sich auf periodischen magnetischen Mustern bewegen. Ich untersuche fünf physikalische Fragen für verschiedene Situationen mit Hilfe von Brownian-Dynamics-Simulationen. Die Simulationen werden durch Experimente anderer Mitglieder meiner Gruppe untermauert. Ich zeige, wie man einen adiabatischen, topologisch geschützten diskreten Zeitkristall mit drei kolloidalen Teilchen baut, die über dipolare Wechselwirkungen interagieren und sich auf einem blumenförmigen periodischen Muster befinden. Ich erweitere dieses Motiv auf verschiedene kristalline Raum-Zeit-Strukturen. Ich diskutiere den Unterschied zwischen topologisch geschütztem und geometrischem Transport. Ich zeige, wie sich der Transport als Funktion der Teilchenzahl in einem Ensemble von mehreren kolloidalen Teilchen pro Einheitszelle von topologisch zu geometrisch verändert. Dipolare Wechselwirkungen erzwingen den Zusammenbau von  $n$  kolloidalen Partikeln zu einem Zweibeiner. Ich habe eine topologisch geschützte polyglotte Programmierung für Zweibeiner, welche auf quadratischen Mustern laufen, entwickelt. Das polyglotte Programm zwingt Zweibeiner unterschiedlicher Länge gleichzeitig in verschiedene vordefinierte Richtungen zu laufen. Ich analysiere das Laufen der Zweibeiner auf quadratischen und sechseckigen Mustern in der Schwerpunkts- und der instantanen Drehzentrumseichung, mit der ich die Bewegung in passive und aktive Komponenten zerlegen kann. Schließlich zeige ich bei nicht-adiabatischen Steuergeschwindigkeiten, wie die hydrodynamische Wechselwirkung die passive Bewegung unterdrückt und die Bewegung einzelner kolloidaler Partikel unterdrückt, wenn sie nicht von aktiven Zweibeinern beim Laufen unterstützt werden.



# Contents

<b>I Topological protected motion of interacting magnetic particles</b>	
1 Introduction . . . . .	3
2 Time crystals . . . . .	13
3 Adiabatic driving, geometrical physics and topological transitions . .	15
4 Polyglot programming . . . . .	17
5 Gauge dependent and gauge invariant aspects of topological walks .	19
6 Non-adiabatic walking . . . . .	21
7 Brownian dynamics simulations of magnetic colloidal particles on magnetic patterns . . . . .	23
<b>II Publications</b>	
Publication 1	
Adiabatic and irreversible classical discrete time crystals . . . . .	P1
Publication 2	
Hard topological versus soft geometrical magnetic particle transport	P2
Publication 3	
Simultaneous polydirectional transport of colloidal bipeds . . . . .	P3
Publication 4	
Gauge invariant and gauge dependent aspects of topological walking colloidal bipeds . . . . .	P4
Publication 5	
Colloidal trains . . . . .	P5
<b>III Methods</b>	
8 Simulations . . . . .	101
9 Transcription Matrix . . . . .	105
<b>IV Summary</b>	109
<b>Bibliography</b>	113



## Part I

---

# **Topological protected motion of interacting magnetic particles**



# Chapter 1

## Introduction

When I was young I was fascinated by magic. A magician would take his wand, waver with the tip of his wand, make a mysterious spell and make things happen that took me away in the world of wonders[1]. Now that I am adult, of course I would explain those wonders in a different way. From a perspective of physics we might discard this magic as fake, however, from a mathematical point of view, the phenomena described is clearly topological[2]. We might describe the tip of the wand as moving on a closed curve. To better distinguish an open curve from a closed curve, we call a closed curve a loop. So the tip of the wand moves on a closed curve. The spell of the magician, of course, is solely made for dramatical reasons and does not affect the outcome of the phenomenon at all. So the mathematical heart of the mystery is that the response of the rest of the world to this closed loop is not a closed loop, but a real change to what was before. Mathematical speaking, we replace the word mysterious by the word topologically non-trivial.

Imagine me as a kid trying to repeat the spell, mimicking the motion of my magical hero, albeit, since I was a kid at that time, on a smaller scale.

It didn't work!

Why didn't it? We may answer this question in a way a physicist would: Lets try experiments with kids at each stage of development. The small kid is unsuccessful, mathematical speaking the loop is topological trivial, we could as well shrink the loop to a point (it is zero-homotopic) and the effect on the rest of the world would be the same: no change! At which scale of a human, or at which scale of the size of the loop, does the magic work for the first time? This is when a topological transition occurs, we are at a tipping (bifurcation) point, and once this point is enclosed by the loop, suddenly it works, our spell changes the world as compared to what it was before the loop started. The loop is no longer topologically trivial, but topologically non-trivial.

Why would I tell you this little anecdote? Well, in the present work I will show that there is a topological non-trivial system, a magnetic colloidal model system[3], that is real, where all the wonders described above work according to the laws of physics. I must admit, the system is real to my fellow experimental friends in Thomas' group, but somewhat virtual to me, since I only had the honor to simulate the response of the colloids to the topological non-trivial loops designed by me to change the colloidal world and make my experimental fellows (Mahla, Anna, Farzaneh, Jonas, Jonas, Thomas, Thomas and Thomas) happy.

I will not hand my wand over to you. The wand is part of my world, that I call the *control space*  $\mathcal{C}$ . The name control space is for obvious reasons. The loop in control space controls the response of the rest of the world. The rest of the world is in a different space. I will describe different colloidal worlds, and depending on the complexity of the colloidal world (the number of different degrees of freedom), the other world will have various different dimensions and aspects. In simple circumstances I just call the colloidal world (the plane where the colloids move) the *action space*  $\mathcal{A}$ . In more complex situations I will divide the colloidal world into degrees of freedom of further spaces, and the colloidal world then consist of a *product space*  $\mathcal{A} \otimes \mathcal{T}_p$  of action space  $\mathcal{A}$  and *transcription space*  $\mathcal{T}_p$ .

Since my loop, lets call it  $\mathcal{L}_\mathcal{C}$ , causes an effect in the colloidal world  $\mathcal{A} \otimes \mathcal{T}_p$ , there must be an interaction between my wand (living in  $\mathcal{C}$ ) and the colloidal world (in  $\mathcal{A}$ ). I will have to describe the interaction of my wand with the colloids in the entire world, i.e. in the product space  $\mathcal{C} \otimes \mathcal{A}$ , respectively in  $\mathcal{C} \otimes \mathcal{A} \otimes \mathcal{T}_p$ .

If you want to be a good magician: Never tell anyone about the details of your wand. Well, I am a physicist, and therefore let me tell you about the physical nature of my wand. The wand I use to interact with the magnetic colloids is a homogeneous external magnetic field  $\mathbf{H}_\mathcal{C}$ . What else should it be? The colloids are, as mentioned before, paramagnetic colloids, or to be more precise core shell colloidal particles of diameter  $2.8 \mu\text{m}$  with a core filled with a lot of superparamagnetic magnetite and maghemite grains and a shell made of polystyrene[4]. Maybe I should also tell you that the surface of the colloids is functionalized with carboxylate groups, that dissociate when put into water and thus render the colloidal surface negatively charged. In most of the cases described in this thesis my external field is very large (of the order of a few 1000 A/m), hence the exact strength of the field does not matter, only the orientation of the field does. My control space of the external field is thus the surface of a sphere. As topology is what matters here, if you look up the topological

properties of a spherical surface you will realize that the topology of a sphere is trivial. The sphere has *genus*  $g = 0$ , i.e. the sphere is a surface having no hole. An example of a topological non-trivial surface is a torus of  $g = 1$  that has a hole. Any loop  $\mathcal{L}_{\mathcal{C}}$  on a sphere is topologically trivial, it is zero-homotopic and we can continuously deform the loop to a single point on the sphere without the loop ever leaving the surface of the sphere during the deformation. Not so for a torus. A torus is topologically non-trivial and a loop on a torus that winds around its hole is topologically non-trivial loop. It cannot be deformed into a point without leaving the surface of the torus during the deformation. It is funny that of all possible choices of (two-dimensional) control spaces we ended up with the only one, a sphere, that is topologically trivial.

Well, actually the control space is not a sphere. It is a punctured sphere. There are specific orientations of the external magnetic field for which I will lose deterministic control in my simulations, and my fellow experimentalists will have a probabilistic outcome of the motion of the colloids. For full control of what is going on, we forbid the encounter of a loop with those problematic points, and here we go, the punctured sphere is topologically non-trivial. Sometimes it is important to know what to do, sometimes it is even better knowing what not to do. The problematic points on the sphere are few, if the colloidal world is sufficiently simple. One of the tasks I had in my PhD-work was figuring out sufficiently simple, but topologically non-trivial colloidal worlds, that allow the computation of those problematic points in my control space. It is then straightforward to predict which loops in control space will cause a topologically non-trivial response for the colloids. These are the loops that wind around one or more of the problematic points.

I have described to you the physical nature of my world, the control space  $\mathcal{C}$ . Lets talk about the colloidal world. You already know the physical properties of the colloidal particles. Let me tell you about the colloidal world and of course about its topological properties. The colloidal particles, as proper colloidal particles, are immersed into a liquid, my fellow experimentalists use water as the liquid. For me the only important thing about the liquid is its viscosity. The embedding of the colloids into the liquid renders the system an overdamped system and I can use *Brownian dynamics* simulations that neglect inertial effects for describing their response to the topological non-trivial loops of control space. In fact, the colloidal particles are non-proper colloidal particles. They sediment in the liquid (proper colloidal particles wouldn't sediment). In order to prevent them from sedimenting for ever, there is a lower surface, where the sedimentation of the colloids abruptly stops. It does not stop when the colloids touch the surface, but it stops a few nanometers above this surface. My

fellow experimentalists cover the surface with a negatively charged electrolyte if the surface is not negatively charged in the first place. The colloidal particles are repelled from the surface when approaching closer than the Debye length of our ultrapure water and therefore hover above the surface. This trick prevents the adhesion of the particles to the surface, and thus renders our colloidal particles into obedient servants, following each command given by my external loop, by laterally moving into the desired position above the surface.

How can I tell the particles, where to go? Well, I have forgotten to tell you, that the surface is not only negatively charged but below a spacer layer of photoresist there is a thin (nanometer) ferrimagnetic exchange bias film. The magnetic layer is made from gold and cobalt sputtered onto a substrate by yet another set of experimentalists from Poznań. After magnetization the films have a net magnetization perpendicular to the film surface. I am delighted the folks from Poznań provided us with those films and you will therefore find them as coauthors on the publications appended to this thesis. Well, they did not provide us with their magnetic films. Prior to the arrival of the films in Bayreuth, the films made a little detour via Kassel, where there is a collection of further experimentalists, who also appear on the publications in this thesis. The Kassel experimentalists bombarded the film with Helium ions, not everywhere, but only on specific areas that were not blocked by a photolithographically applied mask. The bombarded regions of the film become vulnerable to remagnetization (the bombardment with ion lowers their coercive field) and the Kassel experimentalists remagnetize the bombarded regions such now the blocked regions are magnetized in one direction and the non blocked regions are magnetized the other way[5–8]. The film is now a magnetic pattern with up and down magnetized domains of the area  $A_{\text{domain}} \approx (5 \mu\text{m})^2$ .

In Bayreuth my fellow experimentalists cover the film with regions of up and down magnetized domains with a photoresist. This serves as a spacer and blurs the magnetic field experienced by the colloidal particles into a field that is significantly smoother than the field right at the magnetic film surface.

In figure 1.1 you can see a scheme of the control space  $\mathcal{C}$  of the external field together with a typical loop applied to the system. To the right, you see a scheme of the magnetic film, the spacer, and the sedimented colloidal suspension on top of it.

So far I have told you everything about the experimental system. Wait! I forgot to tell you about the choice of the pattern imprinted into the mask used to bombard the film in Kassel. The masks have been designed in Bayreuth, some

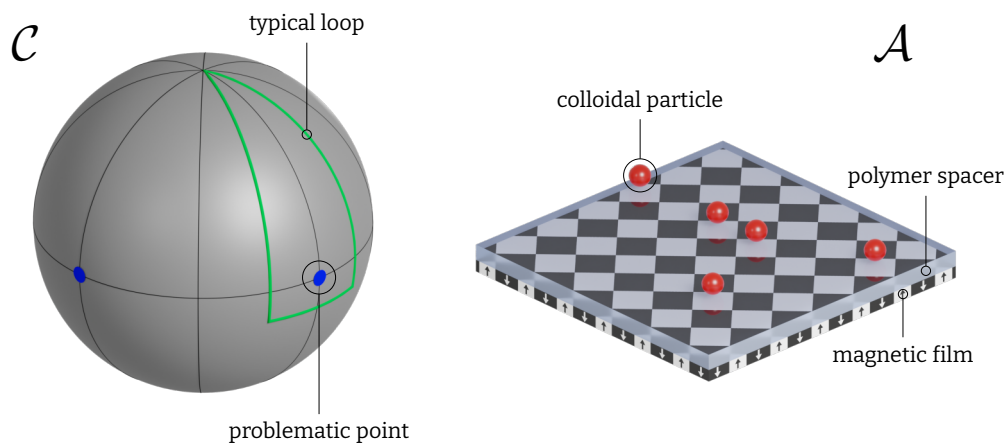


Figure 1.1: Scheme of the control space  $\mathcal{C}$  and of the action space  $\mathcal{A}$ .

of them by my predecessor Johannes Loehr and some of them by me as well as by Anna one of my fellow experimentalists. The design of the pattern is super important. The choice of pattern defines the location and the amount of problematic points in my world, the control space  $\mathcal{C}$ . It is obvious that I wanted to have a say, which patterns to prepare. I made a variety of stupid choices of patterns, but luckily not all the choices I made were bad. Some of the choices worked quite well and let me and my experimental fellows explore some physically interesting topological transport problems.

In figure 1.2 I present a few good and some bad choices of patterns together with the problematic points in control space. You will realize that periodic patterns in figures 1.2a-c seem to be particularly simple what concerns the problematic points in control space. Periodic systems are characterized by just one unit cell. By identifying opposite boundaries of the unit cell of a periodic pattern, the whole pattern becomes topologically a torus, a mathematical trick that I stole from solid state physics. As already mentioned, a torus is topologically non-trivial. More complex patterns cannot be more trivial than a periodic system and many of them can be described topologically with a torus of higher dimension (A two dimensional torus is the product of two one dimensional circular spaces, an  $n$  dimensional torus is the product of  $n$  circular spaces). Well organized patterns such as the five fold symmetric quasi crystalline pattern in figure 1.2d produces a dense mess of problematic points in control space. The good patterns with simple control space have been used for the publications appended to this thesis.

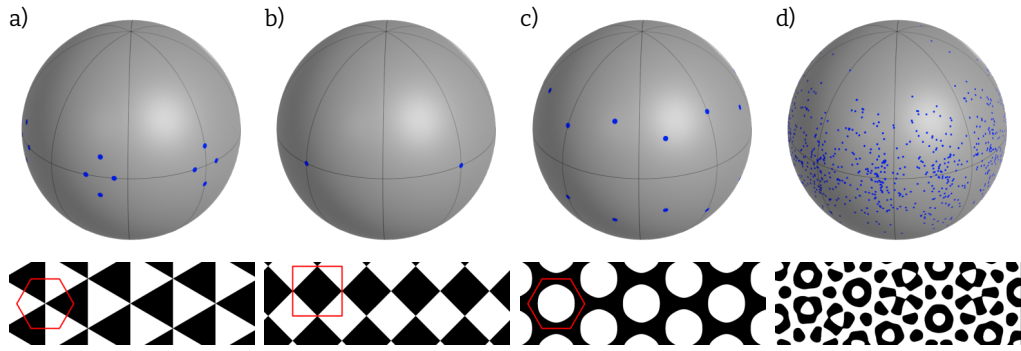


Figure 1.2: The bifurcation points (blue) on control space  $\mathcal{C}$  for different patterns. For periodic patterns (a-c), the boundary of a unit cell is drawn in red.

The discovery of a good pattern, however, is not all I needed to find. There are a multitude of topologically non-trivial loops causing non-trivial transport behavior, the colloidal particles can remain separated at low density, but they assemble to more complex structures like bipeds, or into demixed droplets if using magnetite nanoparticle solutions that do not mix with another majority liquid. All of these variations cause a multitude of interesting physics problems. My thesis will focus on four major systems:

- single particle systems on periodic patterns
- topological transport of bipeds built from a finite set of colloids
- the topological transport of three individual colloidal particles per unit cell that remain separated even when residing in one unit cell, and
- the behavior of a macroscopic assembly of colloidal nano-particles

Physical interesting questions arise when proper balancing the different forces at work in the system. There is a pattern potential, that describes the interaction of single colloidal particles with the internal magnetic field created by the magnetic pattern. Since we superpose this field with the external magnetic field from my control space, this potential parametrically depends on the orientation of the external magnetic field. When we have the colloidal particles separated from the pattern by an elevation of the order of the domain size, the colloidal potential takes the simple form

$$V \propto \mathbf{H}_C \cdot \mathbf{H}_p$$

where  $\mathbf{H}_p$  is the field generated by the pattern. Compare this simple potential with the spin orbit interaction

$$V \propto \mathbf{L} \cdot \mathbf{S}$$

of electrons in a semiconductor. The spin orbit coupling was the first interaction used by Kane[9, 10] to explain topological non-trivial motion of electrons in a semi conductor. The similarity in the mathematical structure of both interactions explains why many of the effects known in topologically non-trivial electronic systems can be directly transferred to colloidal systems.

Colloidal particles are solid and there is an excluded volume interaction, van der Waals interaction plus short range electrostatic repulsion. For reasons of simplicity these interactions are modeled via a Weeks-Anderson-Chandler potential[11]. We can use such simplifications since we are not interested in the details occurring when colloids come close to each other, other than the excluded volume effect.

A third interaction is the dipolar interaction of the colloids. The colloids themselves produce a dipolar magnetic field for one particular colloidal particle such that the magnetic moments of other dipoles are attracted or repelled from the first colloidal particle, depending on the relative orientation of both dipoles with respect to their separation vector. Since the magnetic moments of the particles are induced dipolar moments, the moments in turn depend on the magnetic field at the location of the dipole. In general this produces a convoluted self consistency problem between the dipole moments and the magnetic fields. When the dipolar interaction is weak and if the external field from my control space is strong, the magnetic moments can be treated as if only the external field were present.

Finally, the colloids experience fluctuating and hydrodynamic forces from the liquid they are immersed into[12]. Within the framework of Brownian dynamics, those forces are described by a hydrodynamic friction force into the direction opposing the particle velocity and a random force. Both forces must obey the fluctuation dissipation relation. The thermal forces and hydrodynamic forces play an important role in some of the examined systems but are irrelevant in other problems.

My Brownian dynamics simulation program allows to toggle or tune all these interactions and it automatically creates trajectories of the colloids subject to the control loops. The speed of the loop in control space determines the strength

of the hydrodynamic friction forces. A particular simple response of the colloids to our loop arises when adiabatically driving the loop at such a low speed that the result after a loop no longer depends on the time schedule with which we drive the loop. In this particular case, the change after the application of the loop is purely geometrical, it depends on the path of the loop but no longer on the time schedule. In my simulations I can tell whether the driving is adiabatic or not by looking for speeds that no longer alter the outcome significantly. The control loops within my simulation program can afterwards be automatically transferred to the wave generators that drive the real system investigated by my fellow experimentalists in Bayreuth.

Actually, my system cannot always be driven adiabatically. My system is non-ergodic, which means that there are one or more minima per unit cell of the colloidal potential generated by the pattern depending on the position of the external field in control space. The minima are generically separated by potential ridges much higher than the thermal energy and transitions from one minimum to a neighboring minimum are impossible. Since there may be a different number of minima in one region of control space than in another region, there are fences separating the regions of more minima from those with less.

The posts of those fences are hammered into control space exactly at our problematic points. The potential somehow prefers to have as little stationary points (minima, saddle points and maxima) as possible and fences always are curved into the excess regions, as if they were deformed by the balance of Laplace like pressure into the excess region and a fence tension (Segments of grand circles of the control space of course are straight and non curved). You can tell from the fence curvature on which side of the fence there are more stationary points than on the other side. If you cross a fence from an excess minimum region to the lower minimum number region, a minimum disappears via the collision with a saddle point. The collision partners change if you switch the segment of a fence at a problematic point. As the problematic points are right on a fence, in many cases it is necessary to cross a fence in order to circulate around a problematic point and cause topologically non-trivial motion. The transport is only adiabatic if you cross the fence with particles occupying minima that survive the crossing. Otherwise you temporarily loose control when the particle relaxes to a new minimum position.

You actually don't loose control because the relaxation into the new minimum is topologically protected and can be continuously deformed in an adiabatic motion by deforming the path in control space in a way such that you cross the

right but not the wrong neighboring fence segment. Note that the topological protection of an irreversible loop works only for one direction of the loop. The reversed loop is topologically protected by another adiabatic loop, such that back and forth driving of an irreversible loop does not necessarily cause transport into opposite directions.

You see that my control space has been decorated with quite some collection of geometrical objects, the areas, the fences, and the problematic points.

A lot of my work depended on the race who would have interesting results first, me in the simulations, or my fellows in their experiments. The results presented in the publications appended to the thesis are difficult to disentangle into results achieved by me or the experimentalists. They are rather a true result of the synergy occurring due to this form of collaboration.

Creating the simulation program and transferring the results to the experiments has been one task of my PhD work. It is probably a standard kind of program adapted to our needs. The real fun of the work was the search for interesting physical questions that might be attacked with this system and being able to solve them together with my experimental friends. In the following, I will raise but not solve those physical questions, but rather refer you to the solution presented in the different publications.



## Chapter 2

# Time crystals

I am son of clock makers, so I know how a clock works. A mechanical clock stores the energy used to run it in a spring, there is a harmonic oscillator in a clock running at its eigen-frequency. The escapement is used to keep the oscillator running at constant amplitude and thus not change its oscillation frequency. It also sets into a ratchet like motion a gearbox that then transfers the motion to the clock hands. While the harmonic oscillator of a mechanical clock oscillates at an eigenfrequency of typically a few Hz, the hour hand needs half a day to return to its position. The response of the hour hand is thus a subharmonic response to the driving oscillator. These things are quite old and they date back to the 17th century[13].

How suprised I was to learn that one of the most famous physicists, Nobel laureate Franck Wilczek, terms such a machine with a new name, i.e. a discrete time crystal[14–16]. A discrete time crystal is a system where the system response to a periodic drive is subharmonic such that the discrete time translation symmetry of the problem is spontaneously broken[17]. Franck Wilczek is interested in the topic of discrete quantum time crystals[18–20]. The question I posed myself is: Can we produce a discrete time crystal using our colloids? The answer is in a way simple and positive in another way it is not so easy and quite complex. Consider any nonlinear system, in which it is quite ordinary to have a higher order harmonic response[21]. Run the system adiabatically and if the response is still with a higher harmonic response, redefine the response coordinates into driving coordinates and redefine the responding system into the driving system. Such redefinition of cause and result is allowed in the quasistatic regime since then there is a reciprocity relation such that enforcing the motion in the responding system without touching the drive causes the same motion in the drive as if we would enforce its motion. With the redefinition of driving and responding system, we immediately have a system the has subharmonic instead of higher harmonic response. Our reasoning implies that our system looked upon from the product space  $\mathcal{C} \otimes \mathcal{A}$  must have a stationary manifold that is topologically nontrivial. The stationary manifold is those points in product

space, where neither the coordinates in one or the other subspaces  $\mathcal{A}$  and  $\mathcal{C}$  experiences any force, while the coordinates in the other space are enforced to keep constant. If you have found a curve on this stationary manifold where the projection of the curve in one space has a different period than the period in the other space you are done and have a time crystal. In our publication 1, I show how the use of a flower shaped sixfold pattern and a tuning of all the interactions at work in the proper way creates a system for which I can generate such topologically non-trivial manifold. The topology of a manifold of a manybody system[22–25], involving more than three colloids however, can become quite complex. What is new compared to the clocks is that the clock of my parents does not work in a quasistatic way. The ratchet effect in the escapement makes the clock an irreversible device, which can only move forwards but not backwards. In the discrete time crystal, the new result is that my time crystal's response is time reversal invariant, which is a direct consequence of the adiabatic driving. I close this section with a quote from Krzysztof Sacha[26, 27], available on SciPost Physics as comment to our time crystalline work[28]:

This work touches on an important problem of what we mean by classical time crystals. In the formation of quantum-time crystals, spontaneous breaking of the time translation symmetry is the key element. In classical mechanics the consequences of time translation symmetry are not that dramatic as in the quantum case. For example, time independent systems possess the continuous time translation symmetry, but any solution of classical equations of motion breaks this symmetry unless we consider a trivial situation of a particle at rest. Thus, breaking of the time translation symmetry in the classical case is not as surprising as spontaneous breaking of such a symmetry in the quantum many-body case. When we switch to periodically driven classical systems, especially many-body systems, then stable periodic evolution of the systems is highly nontrivial because it is related to ergodicity breaking. The present interesting work is related to such an important problem.

(Krzysztof Sacha, 1.5.2022)

## Chapter 3

# Adiabatic driving, geometrical physics and topological transitions

Geometrical physics is a way to look at solutions to physical problems that works once an outcome of some manipulation depends on the path of the modulation, but not at the speed, with which one drives the system through this path[29]. The physics depends on the geometry of the path, the dynamics are less relevant. Geometrical physics thus appears in all branches of physics, and often can be regarded as a gauge theory. The time schedule of driving through the path is one gauge, a different timetable another gauge. The physics however is gauge invariant.

Examples of gauge theories span from quantum field theories for elementary particles[30], electrodynamics[31], over low Reynolds number hydrodynamics, (Frank Wilczek, our nobel laureate and inventor of time crystals has been busy here as well[32, 33]), over the equation for Dirac electrons in a two-band semiconductor[34], toward the Foucault Pendulum of classical mechanics[35, 36]. According to Emmy Noether, an invariance of a system with respect to a change of the gauge is associated with a conserved quantity[37]. In electromagnetism, the result of the gauge freedom of the vector potential is the conservation of the charge, for the Dirac electrons, the conserved quantity is the Hall resistance. For low Reynolds number swimmers, the conserved quantity is the area in the abstract and multidimensional shape space of our low Reynolds number swimmers, and for the Foucault Pendulum it is the area enclosed by the path the Foucault pendulum moves during a day.

There are conserved quantities that continuously change when you continuously change the parameter of the system. For example, the angle of precession of the pendulum plane per revolution of the earth changes continuously with the latitude on earth where the Foucault pendulum is located. The area en-

closed by a loop is a geometric quantity. Imagine a loop around the equator, lying in the  $xy$ -plane of a sphere of radius one, centered at the origin. We want to continuously move the center of the sphere in the  $xy$ -plane together with the sphere and the loop, without the loop ever touching the origin. This is easy! You first rotate the loop on the sphere about the origin such that the loop now lies in the  $yz$ -plane and now you move the sphere in the  $x$ -direction. At no time there is any chance of the loop hitting the origin. The task, however, becomes impossible if you require that for symmetry reasons the loop and the center of the sphere have to remain in the  $xy$ -plane during the process. In the first case the winding number of a loop about the origin is a non-well defined quantity, while in the second example the winding number about the origin is a well defined integer, a topological invariant, that may not be changed continuously.

We thus can distinguish geometric conserved quantities from conserved quantities that are symmetry protected topological invariants. In the quantum Hall effect, the Hall-resistance is proportional to the product of fundamental physical constants and the Chern number, a specific topological invariant[38, 39]. The Hall resistance at zero temperature as a function of an external magnetic field therefore can take on only integer value multiples of the resistance quantum. At finite temperature the symmetry protection of the topological invariant becomes more and more broken and one observes a more and more continuous behavior of the Hall-resistance with the field. The Hall resistance becomes a geometric quantity and is no longer a topological invariant. The reason for the change from topological versus geometrical behavior are thermal excitations that break the symmetry and with it the topological protection[40].

How can we move from a topological protected transport of colloids toward a geometric transport in our colloidal system?

The answer to this question is given in my publication 2, where again via simulations and by experiments by my coauthors, we (the authors) show you that the answer differs from the one of the quantum Hall system.

## Chapter 4

# Polyglot programming

I have told you that a topological transition is invoked once I deform the loop in control space such in the end it winds around one of the problematic points. What if I want to have different topological classes of transport without moving the loop to wind around a problematic point? Well, if the mountain won't come to Mohammed, Mohammed must go to the mountain! Can we move the problematic point into the fixed loop? Indeed we can. If we have an assembly of colloidal particles the problematic point can depend on the conformation of the assembly. If dipolar interactions between our beads are strong, they assemble into a biped, a stick of  $n$  colloids that has two ends that we call the two feet.

The dependence of the problematic points on the biped length was discovered by Mahla, my experimental coworker. We worked out the location of the problematic points as a function of the length and orientation of the bipeds. Symmetry helps here and enslavement of the biped orientation to the external field simplifies the matter such that bipeds on square patterns can be understood in great detail. For a fixed loop we can sort bipeds of different length into different topological classes and transport them simultaneously in different ways.

If we do not fix the loop but search for the loop that sorts the bipeds into desired topological classes, one has to invert the problem. The inversion of the problem was my idea. As you might know in the meantime my strengths are my computer skills. So sometimes I scroll through the internet and encounter crazy ideas of computer scientists. One such crazy idea is the programming of complex polyglot programs. A polyglot program is a computer code that can be compiled with different computer languages. The usual polyglot can be compiled by several computer languages to perform the same task. On *Stack Exchange* I ran across a polyglot challenge to write a code that can be compiled for  $n$  computer languages and returns the number  $i$  for the  $i$ th computer language amongst the  $n$  different languages[41]. Challenge: who can write the code with the highest number  $n$  of languages? The challenge is ongoing, when submitting our polyglot paper 3, the record lay at 258 different languages. Time

#### *Chapter 4: Polyglot programming*

has progressed and while writing my thesis 2 years later,  $n$  has increased to 377 computer languages. The funny part of the polyglot program the result for each of the languages is different.

Could we do something similar, i.e. program a loop that results in  $n$  predefined different moves of bipeds of  $n$  different length? The answer is yes and  $n$  can be large (not as large as in the challenge) if the moves are adapted to the specific abilities of different length bipeds. Larger bipeds walk with larger step width for simple loops. When we want the bipeds to move in a way not particularly accommodated to the skills of the bipeds, things become more involved. If you want to know how to make bipeds write different letters simultaneously or if you want to know how to use such polyglot programming to control addition polymerization reactions of bipeds, you will find out how far we got in the task of predefining the path of bipeds and looking for the loop in control space to robustly perform the desired task in my publication 3.

## Chapter 5

# Gauge dependent and gauge invariant aspects of topological walks

In chapter 3 I have told you that adiabatic driving renders the physics a geometric property, with a freedom of choice that is called a gauge. I also told you that a control loop in control space transports bipeds in a topological protected way. What exactly is transported in a biped? Define a specific reference point within (or not within) the biped, and observe its motion. The choice of reference point is a gauge. We can choose the center of mass in the middle of the biped as reference point. This is in fact a good choice for the topological description as you will find out when reading publication 4. The choice lets us easily emphasize the topological aspects of the problem.

If you have ever actively walked, however, you know that the description of walking is not particular well described when focussing on your belly. Your feet seem much more appropriate to describe a walking motion. You as I, probably have two feet. Which foot of the two should one choose as a reference point? Simple! The foot that is on the ground! But we swap the foot that is on the ground while walking. Sometimes it is the left foot, later it is the right foot. Well, choose a more abstract point of reference, that is not fixed to the body. Choose the instant center of rotation. The instant center of rotation oscillates between the left and the right foot, remains on one foot while it is grounded and hops to the other foot via a path no longer on your body while you ground your second foot and raise the first.

The path from one foot toward the other while swapping the grounded foot is an interesting geometric property characterizing the way of walking. If you are walking on solid ground the path is the direct connection between the two feet. If you are however also sliding like on ice you will be translated by the sliding. A translation of the body is a rotation of the body about a center of rotation far

away. So sliding will be visible in the path through how far the path between the feet moves away from the actual walker. If you are sliding down into a potential minimum on a slippery slope I would call such motion a passive motion as compared to your walking that is active. With the path of the instant center of rotation during one loop, we therefore have a measure to divide the motion into active and passive components.

The total motion remains gauge invariant. If we go back to another gauge, another reference point will be transported by the same translation over the period of the loop. The decomposition into active and passive motion is something that holds only within the instant center of rotation gauge. I wonder whether the current focus on active matter can be gauged away.

You will read more details about gauge dependent and gauge invariant aspects of walking bipeds on various patterns in my publication 4.

## Chapter 6

# Non-adiabatic walking

You might be a little confused about whether active motion is actually active motion with what I wrote in the end of chapter 5. Remember that gauge invariance is due to the adiabatic character of the motion. As soon as our bipeds walk faster since we increase the speed of the loop in control space, our colloidal bipeds and any other physical entity will experience hydrodynamic resistance, especially when put in a dissipative environment such as a viscous liquid. Low speeds are topologically protected against change and cannot change from the adiabatic motion result if the hydrodynamic perturbation is weak. The result is, as we already learned, a topological invariant and therefore an integer. Hydrodynamic forces however can change the topological class of motion once they are strong enough. Most common in our system is the ignorance of a winding number of the loop about a problematic point in control space that is close to the loop.

When the result depends on the speed, the behavior ceases to be gauge invariant and one gauge, the instant center of rotation gauge, becomes the one grabbing the physics much better than the others. The distinction between active and passive motion suddenly becomes highly relevant. Passive sliding motion is suppressed by the hydrodynamic forces much more than active walking motion.

Single colloids only slide and do not walk. In contrast to bipeds of more than one colloidal spherical particles single colloids lack the two feet of the other bipeds. Spherical single particles move entirely passive. It is the passive motion that is rendered topologically trivial first. If hydrodynamic forces begin to matter at higher driving speeds, only active motion of non-single-particle bipeds remain. It is similar to humans where babies are not yet able to walk. That is why we help and carry babies from one place to the other when they are young. We assist the babies in their desire to move from a point A to a point B.

Can we, adult bipeds, I mean bipeds of length longer than one single particle,

## *Chapter 6: Non-adiabatic walking*

assist single colloidal particles to move by a non-trivial unit vector of the lattice? We (the authors of the paper) will show in publication 5 how young adults, i.e. doublet bipeds consisting of two colloidal particles, firmly grab a baby biped such that it doesn't fall off while carrying it, and carry them along with the doublet walking. A doublet will have a maximum number of babies it can carry. Interesting stuff happens when a young adult is overloaded with babies he has to carry along. I will not tell here what, you better read my publication 5.

## Chapter 7

# Brownian dynamics simulations of magnetic colloidal particles on magnetic patterns

In the previous chapters, I introduced you to the real magnetic colloidal particle systems above magnetic patterns. I hope to have convinced you that this system is a neat model system to study a rich variety of fundamental transport problems that are all related to topology. The fundamental questions can be studied of course with experiments. To my opinion, they must also be studied with simulations. Both ways of attacking the theoretical understanding of the motion, whether one investigates with experiments like my experimental fellows or with simulations like myself, can cause synergistic effects such that finding good physical problems and their solutions can be achieved faster as compared to working alone.

The separation of tasks is clear, the merit of who is responsible for which part of understanding is convoluted and should not be disentangled in the publications that are shared with my experimental fellows. I will append the five publications that I participated during my PhD work after this extended abstract in part II, write about details of my simulation program in part III and summarize the major answers to the questions posed here in part IV.



## Part II

---

# Publications



# Publication 1

---

## Adiabatic and irreversible classical discrete time crystals

*SciPost Physics* **13**, 091 (2022)

**Adrian Ernst**, Anna M. E. B. Rossi, & Thomas M. Fischer

Experimental Physics X, Department of Physics, University of Bayreuth,  
95447 Bayreuth, Germany.

---

This paper introduces time crystalline edge states that are related to the edge states that I found during my master's thesis[42]. However, it did not show any time crystalline behaviour which is the main focus here.

### My Contribution

I had the original idea of creating a time crystalline system using more than one particle per unit cell on a periodic magnetic pattern. For designing and optimizing the different specialized patterns used in the paper we carried out various simulations and experiments. I did simulations and Anna Rossi did experiments, whereas the guidance of the project via the interpretation of the respective results was done together. The further theoretical understanding of the system and the writing of the paper was done in collaboration with all three authors.



# Adiabatic and irreversible classical discrete time crystals

Adrian Ernst, Anna M. E. B. Rossi and Thomas M. Fischer\*

Experimental Physics X, Universität Bayreuth, 95440 Germany

\* [thomas.fischer@uni-bayreuth.de](mailto:thomas.fischer@uni-bayreuth.de)

## Abstract

We simulate the dynamics of paramagnetic colloidal particles that are placed above a magnetic hexagonal pattern and exposed to an external field periodically changing its direction along a control loop. The conformation of three colloidal particles above one unit cell adiabatically responds with half the frequency of the external field creating a time crystal at arbitrary low frequency. The adiabatic time crystal occurs because of the non-trivial topology of the stationary manifold. When coupling colloidal particles in different unit cells, many body effects cause the formation of topologically isolated time crystals and dynamical phase transitions between different adiabatic reversible and non-adiabatic irreversible space-time-crystallographic arrangements.



Copyright A. Ernst *et al.*

This work is licensed under the Creative Commons

[Attribution 4.0 International License](https://creativecommons.org/licenses/by/4.0/).

Published by the SciPost Foundation.

Received 09-03-2022

Accepted 24-08-2022

Published 11-10-2022

doi:[10.21468/SciPostPhys.13.4.091](https://doi.org/10.21468/SciPostPhys.13.4.091)



Check for updates

## Contents

<b>1</b>	<b>Introduction</b>	<b>1</b>
1.1	Time Crystals	1
<b>2</b>	<b>Adiabatic response</b>	<b>2</b>
2.1	Action-, control-, and product-space, and the stationary manifold	2
2.2	Dissection of the stationary manifold	2
2.3	Projection of paths on the stable manifold into loops in control space	3
<b>3</b>	<b>Mesoscopic system</b>	<b>4</b>
3.1	The colloidal model	4
3.2	Brownian dynamics simulations	5
<b>4</b>	<b>Breaking the time translational symmetry</b>	<b>6</b>
4.1	Conformations of three particles in a unit cell	6
4.2	Different ways of locking the orientation of three particles	7
4.3	Topologically trivial and non-trivial loops	7
4.4	A three body time crystal	7
<b>5</b>	<b>Breaking the space and time translational symmetry</b>	<b>9</b>
5.1	Space-time crystalline order	10
5.2	Topologically isolating time crystals	10

5.3 Time crystalline phase transitions	14
<b>6 Conclusion</b>	<b>15</b>
<b>A Numerical details and parameters</b>	<b>15</b>
<b>References</b>	<b>16</b>

---

## 1 Introduction

### 1.1 Time Crystals

Time crystals [1,2] are non-equilibrium [3] periodically driven quantum [4,5] or classical [6,7] systems with subharmonic response [8,9]. Discrete time crystals [10–14] are systems coupled to a power supply with a driving frequency that is a higher harmonic of the intrinsic frequency of the isolated few body system. The eldest scientific report of such subharmonic response are the parametric oscillations observed by Michael Faraday in the ripples of a singing wine glass [15]. Such parametric resonance phenomena have been well described with Mathieu’s differential equation. Later on discrete time crystals have been realized with phase modulated atomic de Broglie waves or cold atoms [16–23]. Time crystals are also found in an interacting spin chain of trapped atomic ions [5], in a disordered ensemble of about one million dipolar spin impurities in diamond at room temperature [24], in molecular spin systems [25], in an ordered spatial crystal [8], and in a superfluid quantum gas [26]. Recently the possibility of continuous time crystals has been also reconsidered [27,28]. Here we report on a dissipative classical system [29] that lacks an intrinsic frequency such that the driving can be with arbitrary low frequency and the response is always at half the driving frequency:

$$\omega_{\text{response}} = \omega_{\text{drive}}/2. \quad (1)$$

As we show, the reason for such behavior lies in the non-trivial topology of the stationary manifold. In previous work, we have used such non-trivial topology for mesoscopic magnetic colloidal systems [30–35] and macroscopic magnetic systems [36,37] to transport magnetic particles across a periodic pattern. This shows that the topological discrete time crystals shown in this work are intimately connected to other classical [38–44] and quantum mechanical [45,46] topological transport phenomena.

## 2 Adiabatic response

### 2.1 Action-, control-, and product-space, and the stationary manifold

The generalized coordinates  $\mathbf{H}_{\mathcal{C}}$  of the drive vary in control space  $\mathcal{C}$ , while the generalized coordinates  $\mathbf{x}_{\mathcal{A}}$  of the few body system vary in what we call the action space  $\mathcal{A}$  (see Fig. 1a) and c). The coordinates  $\mathbf{H}_{\mathcal{C}}$  in control space (in the colloidal example of section 3 the direction of an external magnetic field) can be manipulated externally and the coordinates in action space  $\mathbf{x}_{\mathcal{A}}$  (in section 3 the positions of the colloidal particles) respond to the external modulation. We impose a periodic variation of the coordinates in control space with its trajectory forming a loop  $\mathcal{L}_{\mathcal{C}}$ . For nonzero response, the potential energy  $U(\mathbf{x})$  must couple the driving coordinates

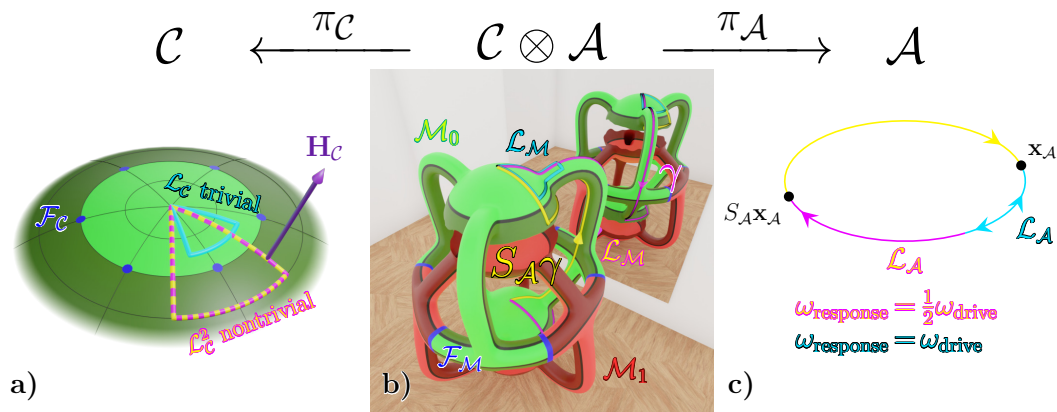


Figure 1: **a)** Control space  $\mathcal{C}$ , with fence points  $\mathcal{F}_{\mathcal{C}}$  (blue) and a trivial (cyan) and non-trivial (yellow/magenta) driving control loop  $\mathcal{L}_{\mathcal{C}}$ . **b)** The stationary manifold  $\mathcal{M}$  in our example is a two dimensional manifold in a three dimensional curved space  $\mathcal{C} \otimes \mathcal{A}$ . We can visualize the stationary manifold only by deforming it in a way that preserves its topology such that it fits into Euclidian space. Such deformed version is shown in b). Because of the symmetry  $S_{\mathcal{A}}$  to each (bright and dark green) region in  $\mathcal{C}$  there are two corresponding regions of minima with the same color on the stationary manifold  $\mathcal{M}$  in  $\mathcal{C} \otimes \mathcal{A}$  and two regions of red color that are maxima. Minima (green) together forming  $\mathcal{M}_0$  and maxima (red) forming  $\mathcal{M}_1$  of the stationary manifold are separated by fence lines  $\mathcal{F}_{\mathcal{M}}$  (blue). Staying on  $\mathcal{M}_0$  it is not possible to reach the lower bright green region from the upper without passing through one of the two dark green regions. A trivial loop  $\mathcal{L}_{\mathcal{C}}$  in  $\mathcal{C}$  causes a trivial loop  $\mathcal{L}_{\mathcal{M}}$  (cyan) in  $\mathcal{M}$  that does not leave the bright green region. The two symmetric paths  $\gamma$  (magenta) and  $S_{\mathcal{A}}\gamma$  (yellow) that connect the two different bright green regions of  $\mathcal{M}$  via a dark green region are concatenated to form a non-trivial closed loop  $\mathcal{L}_{\mathcal{M}}$ , that is projected into  $\mathcal{L}_{\mathcal{C}}^2$  in control space and  $\mathcal{L}_{\mathcal{A}}$  in action space. **c)** Action space  $\mathcal{A}$  is a non simply connected space and the loop  $\mathcal{L}_{\mathcal{A}}$  circulates around a hole of  $\mathcal{A}$ . Points on opposite sites of action space share the same potential  $U(\mathbf{H}_{\mathcal{C}}, \mathbf{x}_{\mathcal{A}}) = U(\mathbf{H}_{\mathcal{C}}, S_{\mathcal{A}}\mathbf{x}_{\mathcal{A}})$ . The yellow/pink non-trivial loop  $\mathcal{L}_{\mathcal{M}}$  in b) can neither be continuously deformed into a point nor into the cyan trivial loop but can be continuously deformed into one of the fences  $\mathcal{F}_{\mathcal{M}}$ .

to the coordinates in action space. The pair of both coordinates  $\mathbf{x} = (\mathbf{H}_{\mathcal{C}}, \mathbf{x}_{\mathcal{A}})$  therefore varies in the product space  $\mathcal{C} \otimes \mathcal{A}$ <sup>1</sup>. For a fixed value of the driving coordinate  $d\mathbf{H}_{\mathcal{C}}/dt = \mathbf{0}$ , i.e. vanishing frequency of the driving modulation  $\omega_{\text{drive}} = 0$ , the action coordinates remain stationary when residing on the stationary manifold  $\mathcal{M} = \{\mathbf{x} \in \mathcal{C} \otimes \mathcal{A} | \nabla_{\mathcal{A}} U(\mathbf{x}) = 0\} \subset \mathcal{C} \otimes \mathcal{A}$ . The stationary manifold is the set of coordinates  $\mathbf{x}$  for which all forces in action space vanish. The gradient  $\nabla_{\mathcal{A}}$  denotes the partial derivative with respect to  $\mathbf{x}_{\mathcal{A}}$ . Here we show that for quasistatic driving ( $\omega_{\text{drive}} \rightarrow 0$ ) it is the topology of the stationary manifold that determines the subharmonicity (equ. 1) of the response in  $\mathcal{A}$ .

## 2.2 Dissection of the stationary manifold

We call  $\mathcal{F}_{\mathcal{M}} = \{\mathbf{x} \in \mathcal{M} | \text{eigenvalue}[\nabla_{\mathcal{A}} \nabla_{\mathcal{A}} U(\mathbf{x})] = 0\} \subset \mathcal{M}$  the fence on  $\mathcal{M}$ . The fence dissects  $\mathcal{M}$  into regions  $\mathcal{M}_i, i = 0, 1, \dots, \dim \mathcal{A}$  of different index of the Hessian of the potential,  $\nabla_{\mathcal{A}} \nabla_{\mathcal{A}} U(\mathbf{x})$ . The index  $i$  counts the number of linearly independent directions that are unstable. In the stable stationary manifold,  $\mathcal{M}_0$ , the index is zero and all forces in the vicinity of

<sup>1</sup>The product space  $\mathcal{C} \otimes \mathcal{A}$  is defined as the set of coordinates  $\{\mathbf{x} = (\mathbf{H}_{\mathcal{C}}, \mathbf{x}_{\mathcal{A}}) | \mathbf{H}_{\mathcal{C}} \in \mathcal{C} \text{ and } \mathbf{x}_{\mathcal{A}} \in \mathcal{A}\}$

the stable manifold drive the action coordinates back to the stable stationary manifold. In Fig. 1b the stable manifold  $\mathcal{M}_0$  is colored in green, while the unstable manifold  $\mathcal{M}_1$  is colored in red. In the adiabatic limit  $\omega_{\text{drive}} \rightarrow 0$  kinetic energy terms and dissipative loss terms become negligible and the response of the system follows a path on the stable stationary manifold  $\mathcal{M}_0$  that is independent of the speed of driving as long as we do not hit the fence. When staying inside  $\mathcal{M}_0$  the response of a system to periodic driving is solely determined by the topology of the stable stationary manifold. If we drive the system across the fence, the action coordinates become unstable. Irreversible processes independent of the driving coordinates  $\mathbf{H}_C$  then let the action coordinates  $\mathbf{x}_A$  leave the stationary manifold and relax back via  $\mathcal{C} \otimes \mathcal{A}$  into the interior of the stable stationary manifold  $\mathcal{M}_0$ .

### 2.3 Projection of paths on the stable manifold into loops in control space

Let  $\pi_C : \mathcal{C} \otimes \mathcal{A} \rightarrow \mathcal{C}$  with  $\pi_C(\mathbf{H}_C, \mathbf{x}_A) = \mathbf{H}_C$  denote the projection from product space into control space and  $\pi_A : \mathcal{C} \otimes \mathcal{A} \rightarrow \mathcal{A}$  with  $\pi_A(\mathbf{H}_C, \mathbf{x}_A) = \mathbf{x}_A$  denote the projection from product space into action space. Suppose there is a two fold fix point free symmetry operation  $S_A$  ( $S_A^2 = \mathbb{1}$ ) acting on the coordinates in the action space such that  $U(\mathbf{H}_C, \mathbf{x}_A) = U(\mathbf{H}_C, S_A \mathbf{x}_A)$  and  $S_A \mathbf{x}_A \neq \mathbf{x}_A$  for all points  $\mathbf{x}_A \in \mathcal{A}$ , then the potential is invariant under the symmetry operation. If the stationary manifold  $\mathcal{M}_0$  is path-connected we can choose a path  $\gamma \subset \mathcal{M}_0$  from any point  $(\mathbf{H}_C, \mathbf{x}_A) \in \mathcal{M}_0$  to its symmetry partner point  $(\mathbf{H}_C, S_A \mathbf{x}_A) \in \mathcal{M}_0$  and concatenate it with its symmetry partner path  $S_A \gamma$  to form a loop (a closed path)  $\mathcal{L}_M = (S_A \gamma) * \gamma \subset \mathcal{M}_0$  (here  $*$  denotes the concatenation of two paths see Fig. 1b). We note that  $\gamma$  is a path but not a loop (magenta in Fig. 1b). Because of the symmetry  $S_A$  in contrast to the path  $\gamma$  its projection  $\mathcal{L}_C = \pi_C(\gamma) = \pi_C(S_A \gamma)$  into control space  $\mathcal{C}$  is a loop. The projection  $\mathcal{L}_C^2 = \mathcal{L}_C * \mathcal{L}_C = \pi_C(\mathcal{L}_M)$  is a loop circulating twice along the same path in  $\mathcal{C}$  and causing a closed loop response  $\mathcal{L}_A = \pi_A(\mathcal{L}_M)$  that closes only after the second circulation of  $\mathcal{L}_C$ . The requirement that there is no fixed point  $\mathbf{x}_A^*$  for which  $S_A \mathbf{x}_A^* = \mathbf{x}_A^*$  may be only fulfilled if  $\mathcal{A}$  is not a simply connected space (in the example of Fig. 1c  $\mathcal{A}$  is a circle). The loop  $\mathcal{L}_A$  thus circulates around a hole of  $\mathcal{A}$ . For this reason also its preimage  $\mathcal{L}_M$  must circulate around a hole in  $\mathcal{M}_0$ . If  $\mathcal{C}$  is a simply connected space (in Fig. 1a  $\mathcal{C}$  is the surface of a sphere and thus simply connected) then  $\mathcal{L}_C^2 = \pi_C(\mathcal{L}_M)$  must circulate around something other than a hole. In fact  $\mathcal{L}_C$  must circulate around the cusps  $\mathcal{B}_C$  of the fence  $\mathcal{F}_C = \pi_C(\mathcal{F}_M)$ . The cusps  $\mathcal{B}_C$  (bifurcation points) of the fence  $\mathcal{F}_C$  are points in  $\mathcal{C}$  where the components of tangent vector  $\mathbf{t} = (\mathbf{t}_C, \mathbf{t}_A) = (\mathbf{0}, \mathbf{t}_A)$  to the fence  $\mathcal{F}_M$  in the tangent control space vanishes. The punctured control space  $\mathcal{C}/\mathcal{B}_C$  is no longer simply connected and any loop  $\mathcal{L}_C \subset \mathcal{C}/\mathcal{B}_C$  with non vanishing winding number around one of the cusps  $\mathbf{H}_C^B \in \mathcal{B}_C \subset \mathcal{F}_C \subset \mathcal{C}$  of the fence, causes a half frequency adiabatic response loop  $\mathcal{L}_A$  in action space.

In Fig. 1, we depict the three spaces  $\mathcal{C}$ , a deformed version of  $\mathcal{C} \otimes \mathcal{A}$  with a deformed but topologically equivalent version of the stationary manifold  $\mathcal{M}$ , and  $\mathcal{A}$ . We draw the different loops and paths in the three spaces to visualize the arguments made in this section. We use these arguments in section 3 to construct a colloidal adiabatic time crystal.

## 3 Mesoscopic system

### 3.1 The colloidal model

Let us use the knowledge from section 2 to suggest an example of a classical adiabatic discrete time crystal. Our model system consists of a two-dimensional mesoscopic hexagonal magnetic pattern made of up- and down-magnetized domains, see Fig. 2. Such patterns can be produced experimentally using e.g. exchange bias films [47, 48]. The pattern, that is covered

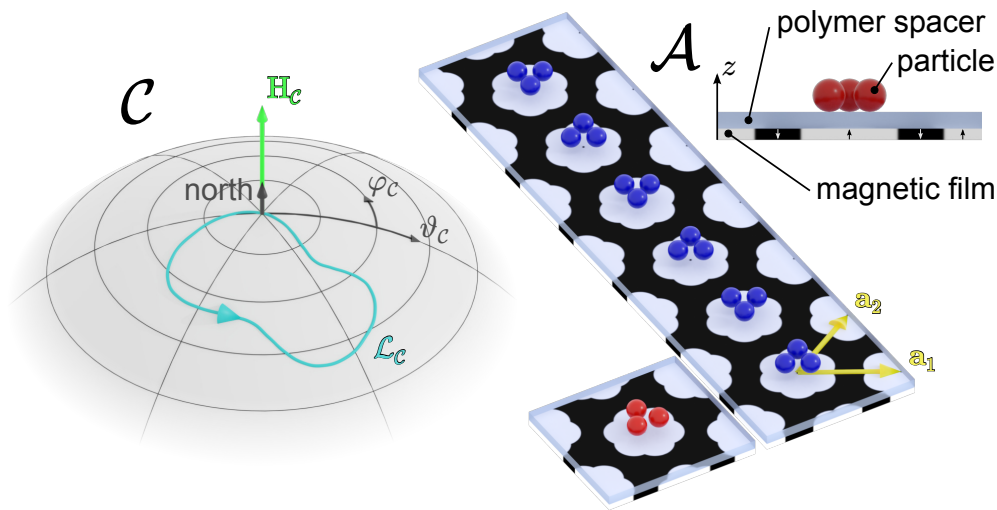


Figure 2: Scheme of the control space  $\mathcal{C}$  that is the set of possible orientations of the external magnetic field  $\mathbf{H}_C$  that we parametrize with the spherical coordinates  $\vartheta_C$  and  $\varphi_C$  measured with respect to the north direction perpendicular to the magnetic film. Within  $\mathcal{C}$  we periodically and adiabatically apply a loop  $\mathcal{L}_C$  that we either apply to an ensemble of 3 paramagnetic colloidal particles in one unit cell (red colloids, here shown for a flower shaped domain in the a-conformation) or to 3 paramagnetic colloidal particles per unit cell (blue colloids, here shown for flower shaped domains in the Q-conformation). In both cases the particles are placed on a spacer above a periodic hexagonal magnetic pattern with primitive unit vectors  $\mathbf{a}_1$  and  $\mathbf{a}_2$  consisting of flower shaped annular up magnetized domains within a counter magnetized surroundings. The equilibrium conformation of the colloids in the flower shaped domains for an external field perpendicular to the magnetic film is an equilateral triangle that can take on two different orientations with corners centered in direction of the lobes of the flower. A time crystalline phase where the colloids respond in a subharmonic way by switching the two orientations after each driving period requires a topologically non-trivial control loop  $\mathcal{L}_C$ .

with a spacer, creates a two-dimensional magnetic potential that acts on an ensemble of paramagnetic colloidal particles. The colloidal particles sediment due to gravity onto the spacer. An electrostatic levitation from this spacer by roughly the Debye length ensures the mobility of the colloidal particles in action space  $\mathcal{A}$ . The potential is a function of the positions  $\mathbf{x}_A \in \mathcal{A}$  of the particles in action space  $\mathcal{A}$ , which is the plane parallel to the pattern in which the paramagnetic particles are located. We treat the paramagnetic colloidal particles as being confined to action space. A uniform time dependent external magnetic field  $\mathbf{H}_C(t) \in \mathcal{C}$  is also applied to the system. Hence, the total potential depends parametrically on the direction of the superimposed external magnetic field. Our control space  $\mathcal{C}$  is a sphere parametrized with coordinates  $\vartheta_C$  and  $\varphi_C$ . In practice we only use the northern polar region of  $\mathcal{C}$  where the second Legendre polynomial  $P_2(\sin \vartheta_C) < 0$  of the tilt angle of the field is negative and thus lateral dipole-dipole interactions are always repulsive. The paramagnetic particles move in action space  $\mathcal{A}$  when we adiabatically modulate the total potential by changing the direction of the uniform external field in control space.

Our two dimensional magnetic hexagonal lattice with primitive unit vectors  $\mathbf{a}_1$  and  $\mathbf{a}_2$  is built from an arrangement of up and down magnetized domains of a magnetic film. The primitive unit cell of the lattice is a six fold symmetric  $C_6$  hexagon containing a down magnetized

matrix that is interrupted by a flower shaped annular up magnetized domain, see Fig. 2. The flower shaped annular domain respects the  $C_6$  symmetry of the Wigner Seitz cell, but breaks the continuous rotation symmetry around the central down magnetized domain. We use two different orientations of the flower shaped annulus, that are related by rotating the flower by  $2\pi/12$ , while keeping the unit cell fixed. In the  $a$ -conformation the lobes of the flower are located in direction of the primitive unit vectors of the lattice, whereas in the  $Q$ -conformation the lobes of the flower are located in direction of the primitive reciprocal unit vectors of the reciprocal lattice.

The total magnetic field is the sum of the pattern  $\mathbf{H}_p$  and the external  $\mathbf{H}_c$  contributions. The potential energy of one paramagnetic particle in the total magnetic field  $\mathbf{H} = \mathbf{H}_p + \mathbf{H}_c$  assumes the form  $U \propto -\mathbf{H}_c(t) \cdot \mathbf{H}_p(\mathbf{x}_A, z)$  [30] if we apply an external field larger than the pattern field  $H_c(t) \gg H_p(\mathbf{x}_A, z)$ . For elevations of the particles above the pattern larger than the modulus  $a$  of the primitive unit vector, i.e.  $z > a$ , the potential assumes a universal shape independent of the elevation and independent of the shape of the up magnetized domain. The purpose of the spacer (Fig. 2) is thus to render the potential close to universal such that only the symmetry and not the fine details of the pattern are important. We therefore distinguish thick spacers that render the potential universal from thinner spacers. The case of the flower shaped domain for thinner spacers in the  $Q$ -conformation topologically deviates from the universal high elevation case. The behavior in the  $Q$ -conformation thus is more subtle and will be discussed in subsection 5.3.

### 3.2 Brownian dynamics simulations

We use Brownian dynamics to simulate the dynamics of paramagnetic colloidal particles. The particles are subject to the single particle potential  $U$  from the interference of the external magnetic field with that of the magnetic pattern and they are coupled via dipolar interactions with a pair potential with magnetic moments enslaved to the external magnetic field  $\mathbf{H}_c$  (for quantitative details see appendix A). We use inertia free over-damped equations of motion that include a friction force proportional to the particle velocity together with a random force that fulfills the fluctuation dissipation theorem. The particles are confined to the two dimensional action space and the integration of the equations of motion is done using a simple Euler algorithm.

## 4 Breaking the time translational symmetry

### 4.1 Conformations of three particles in a unit cell

In the simulations we place three paramagnetic particles on top of the spacer above the flower shaped annulus domain. The paramagnetic particles are coupled via strong repulsive dipolar interactions. We then switch on a time dependent homogeneous external field  $\mathbf{H}_c(t)$ .

When the external field points north  $\mathbf{H}_c = H_c \mathbf{e}_z$  the single particle potential has a six fold symmetry. The competition of the single particle potential with the repulsive dipolar interactions lets the paramagnetic particles position themselves in form of an equilateral triangle with corners in the direction of every second lobe of the flower shaped domain (see Fig. 3a). Because of the  $C_6$ -symmetry of the pattern there are two conformational choices for the orientation of the equilateral triangle. One stable conformation is obtained from the other by a  $C_6$ -rotation operation. Hence the symmetry operation in action space introduced in section 2 for the particular model of section 3 takes on the form of a  $S_A = C_6$ -rotation. The conformations obtained by a  $C_{12}$ -rotation of the stable conformation results in another stationary but unstable conformation in which the particles occupy a saddle point of the total energy.

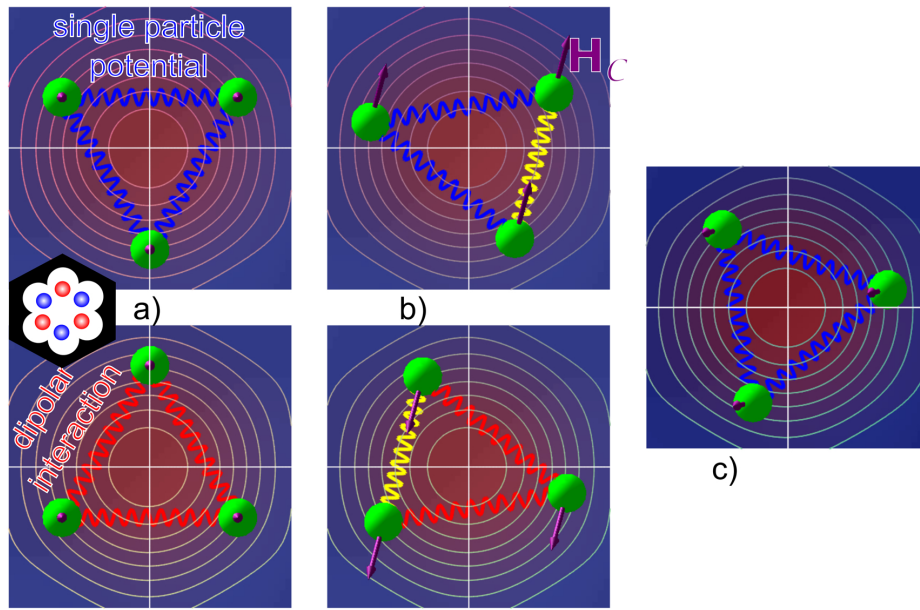


Figure 3: The competition of the single particle pattern potential and the dipole-dipole interaction can lock the orientation of the three particle conformation to the lobes of the single particle pattern potential **a)**, or lock the edge of the triangle of three spheres that experience a reduced dipolar interaction (yellow) to the orientation of the lateral component of the external field **b)**. For both forms of locking there are two possible conformations. One conformation is converted to the other via an inversion operation at the center of the domain. **c)** The third form of locking is with the triangle corner opposite to the lateral component of the external field  $H_C$ . This single conformation has no symmetry partner conformation and it is favored for high tilt angles of the field and for weak dipolar interactions.

#### 4.2 Different ways of locking the orientation of three particles

The dipolar interaction between paramagnetic particles is highly anisotropic. This becomes apparent in Fig. 3b when we redirect the external field  $H_C$  by tilting it slightly from the north pole. The repulsion between paramagnetic particles is then reduced when two interacting paramagnetic particles of the triangle are separated in a direction of the in plane component of  $H_C$ . The three paramagnetic particles thus must find a compromise conformation that is either a preference to orient themselves with respect to the single particle potential as shown in Fig. 3a, or to orient two of the three colloidal particles with respect to the in plane external field direction, see Fig. 3b. The preference for the single particle potential becomes stronger when the tilt of the field is small. In such situation the triangle orientation remains locked to the single particle potential as we turn the azimuth of the external magnetic field. Contrary to this, for high tilt angles one edge of the triangle remains locked to the in plane external field direction as we turn the azimuth of the magnetic field. We thus find two topologically distinct classes (cyan respectively yellow/magenta) of loops in control space as shown in Fig. 1a. Both classes of loops consist of starting with an external magnetic field direction at the north pole, tilting the field at constant azimuth, then rotating the azimuth at fixed tilt and returning to the north pole by reducing the tilt at fixed azimuth. The determination to which class the loop belongs is made by the winding numbers of the loop around the six bifurcation points  $H_C^B \in \mathcal{B}_C = \mathcal{F}_C \subset \mathcal{C}$  that for strong dipolar interaction are identical to the fences in control space and thus are a Goldstone mode. The position of the bifurcation points changes with the dipolar interaction strength and with the elevation.

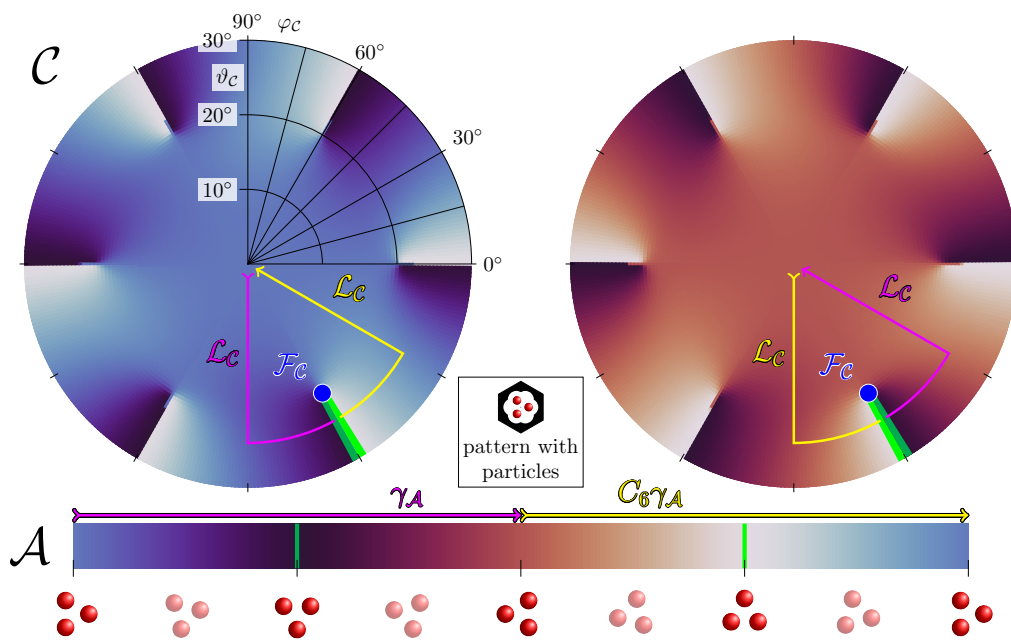


Figure 4: Color-coded equilibrium orientation of the triangle of paramagnetic colloids in action space as a function of the external field orientation in  $C$ . Circulating the (blue) fence point  $\mathcal{F}_C$  twice with a purple and yellow loop  $\mathcal{L}_C^2$  causes the sub-harmonic time crystalline loop  $\mathcal{L}_A = \gamma_A * C_6 \gamma_A$  in action space  $A$  shown in the lower part of the figure together with the three particle conformation. Highlighted particle configurations are stationary for a magnetic field pointing north. Those at the beginning and at the end of  $\gamma_A$  or  $C_6 \gamma_A$  are stable for the magnetic field pointing north. Those stable at the magnetic field of the cut would be unstable for the magnetic field pointing north. Two video clips of the trivial and non-trivial dynamics are provided with the videos [adFig4trivial](#) and [adFig4nontrivial](#).

The continuous symmetry of the Goldstone mode becomes broken when dipolar interactions are much weaker than the single particle potential. The potential has a  $C_6$  symmetry only for the external field  $H_C$  pointing north. For weak dipolar interactions the symmetry broken parts of the single particle potential at finite tilt of the external field  $H_C$  dominate near the bifurcation point. What has been a fence point develops into a fence line surrounding the region around the bifurcation point in control space. Inside the fence it is energetically advantageous to orient the triangle with a corner antiparallel to the external field, see Fig. 3c. In contrast to the former conformations there is no symmetry partner conformation to this third conformation. Entering such a fenced region kills all attempts to construct a time crystal. The dipolar interaction therefore must be sufficiently strong to enable us constructing a time crystal.

### 4.3 Topologically trivial and non-trivial loops

For the rest of section 4 we assume that the dipolar interaction is strong. A loop not winding around a bifurcation point is a trivial loop causing the conformation to respond with the same period as the driving loop. In contrast a loop winding around a bifurcation point adiabatically connects one stable triangle conformation to the distinct orientation rotated by  $2\pi/6$  and the conformation of the paramagnetic particles responds with half the frequency of the frequency in control space.

#### 4.4 A three body time crystal

In Figure 4 we show the color coded equilibrium orientation  $\varphi_{\mathcal{A}}(\varphi_C, \vartheta_C)$  of the triangle of the paramagnetic colloids in action space  $\mathcal{A}$  as a function of the external field orientation, expressed with the spherical angular coordinates  $(\varphi_C, \vartheta_C)$  in control space. We define the orientation angle  $\varphi_{\mathcal{A}} = \left( \arccos \frac{\mathbf{a}_1 \cdot (2\mathbf{r}_3 - \mathbf{r}_2 - \mathbf{r}_1)}{a|2\mathbf{r}_3 - \mathbf{r}_2 - \mathbf{r}_1|} \bmod 2\pi/3 \right)$  as the angle modulo  $2\pi/3$  between the vector from the triangle center to the corner  $\mathbf{r}_3$  farthest from the triangle center and the primitive unit vector  $\mathbf{a}_1$  of the periodic lattice. The corners closer to the triangle center are  $\mathbf{r}_1$  and  $\mathbf{r}_2$ . The parameters of the simulations are as listed in table 1 of appendix A. The triangle orientation  $\varphi_{\mathcal{A}}(\varphi_C, \vartheta_C)$  is a double valued function and there are two leaflets of orientations. Both leaflets are glued together at the light/dark green cuts where the orientation is continuous when switching the leaflet at the cut. The non-trivial purple loop  $\mathcal{L}_C$  starts on the first blue leaflet and switches onto the second brown leaflet where it returns to the original external field orientation while the orientation  $\varphi_{\mathcal{A}}$  follows the open path  $\gamma_{\mathcal{A}}$  to a different orientation than at the beginning of  $\mathcal{L}_C$ , the second yellow revolution of  $\mathcal{L}_C$  concatenates the path  $\gamma_{\mathcal{A}}$  in  $\mathcal{A}$  with  $C_6\gamma_{\mathcal{A}}$  such that the concatenation  $\mathcal{L}_{\mathcal{A}} = \gamma_{\mathcal{A}} * C_6\gamma_{\mathcal{A}}$  is a subharmonic loop causing a discrete time crystalline response. The non-trivial behavior occurs whenever one circulates around the fence  $\mathcal{F}_C$  in control space. For trivial control loops with vanishing winding numbers around each of the six fence points, the response in action space remains trivial, causing no time crystalline behavior. On the arxiv we provide two videos ([adFig4trivial](#) and [adFig4nontrivial](#)<sup>2</sup>) of Brownian dynamics simulations of trivial and non-trivial control loops together with their trivial and non-trivial response. Albeit being stored on the arXiv these videos are an integral part of this work.

An external field that points into the direction of a bifurcation point may be viewed as a loop of infinitesimal radius around the bifurcation point, for which each possible orientation is taken. The orientational degree of freedom becomes a Goldstone mode [49] at the bifurcation point, where it obeys a generalized statistical mechanics Noether theorem [50]. As already mentioned the continuous symmetry of the Goldstone mode becomes broken when dipolar interactions are much weaker than the single particle potential.

## 5 Breaking the space and time translational symmetry

The control loops of the homogeneous external field in control space of section 4 had a discrete time translational symmetry that was broken by the dynamics of the paramagnetic particles. If we arrange several magnetic annular domains into a periodic pattern, the magnetic field of the potential has a discrete translational symmetry in space. In this section we use Brownian dynamics simulations to show that there are ways to break or not break some or all of the discrete symmetries, once we fill some of the neighboring flower shaped annular domains with three paramagnetic particles in a periodic manner. We use two different orientations of the flower shaped annulus, that are related by rotating the flower by  $2\pi/12$ , while keeping the unit cell fixed (see Fig. 5). In the  $a$ -conformation the lobes of the flower are located in direction of the primitive unit vectors of the lattice, in the  $Q$ -conformation the lobes of the flower are located in direction of the primitive reciprocal unit vectors of the reciprocal lattice. The dipolar interaction is long range and anisotropic and there are intercellular interactions between the paramagnetic particles of neighboring annular domains. We have to distinguish the behavior of flowers in the  $a$ - and in the  $Q$ -conformation, if working at lower than universal elevations. Note that the differences between both patterns become irrelevant at universal

<sup>2</sup>supplementary videos, are provided in the ancillary directory <https://arxiv.org/src/2203.04063/anc>. These videos are essential for understanding the dynamics of our time crystals.

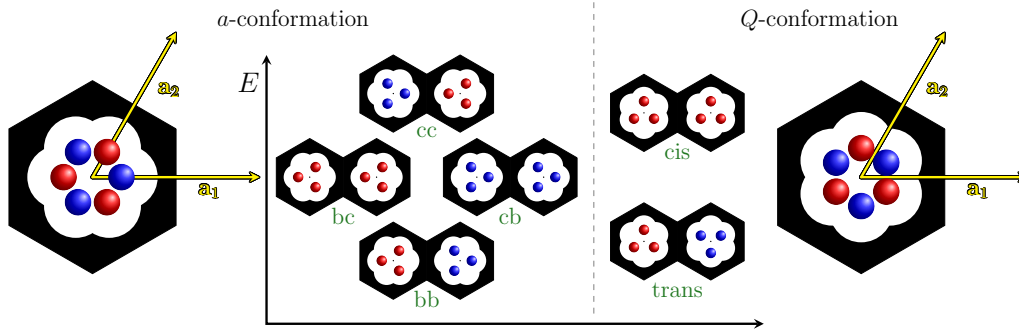


Figure 5: The two configurations of paramagnetic particles in red and blue within a unit cell for an external magnetic field  $\mathbf{H}_C$  pointing north (normal) to the pattern in the  $a$ -conformation and in the  $Q$ -conformation. Intercellular dipolar interactions lead to a splitting of the energy. We distinguish  $cc$ ,  $cb$ ,  $bc$ , and  $bb$  bonds in the  $a$ -conformation and  $trans$  and  $cis$  bonds in the  $Q$ -conformation. The energy splittings cause many body interactions that induce various kinds of spatio-temporal order.

elevations. We can continuously move from the  $a$ - toward the  $Q$ -conformation by joining both conformations at a universal height. In subsections 5.2 and 5.3 we will show that the  $a$ -conformation suppresses the space-time crystalline behavior in the bulk, but not the time crystalline response at the spatial edge of the crystal, while the  $Q$ -conformation supports a bulk-space-time crystalline response.

### 5.1 Space-time crystalline order

The magnetic pattern has primitive unit vectors  $\mathbf{a}$  and primitive reciprocal unit vectors  $\mathbf{Q}$ . Together with the period  $T = 2\pi/\omega_{drive}$  of the external magnetic field loop in control space, we can define 4-vectors  $\mathbf{r}^4 = (t, \mathbf{r})$  and primitive unit vectors  $\mathbf{a}^4$  in space-time. A trivial response of the paramagnetic particles is when the reciprocal (angular frequency, wave vector) lattice of the response is the same as the reciprocal lattice of the drive  $(\omega_{response}, \mathbf{Q}_{response}) = (\omega_{drive}, \mathbf{Q}_{drive})$ . Depending on the strength of the intra- and inter-cellular dipolar interactions, on the conformation of the flower shape annular domain, and on the elevation of the paramagnetic particles above the pattern we find different disordered phases. For example we find orientation disordered time crystalline phases, for which the orientation order parameter  $O = \cos(3\varphi_A)$  between neighboring unit cells is completely uncorrelated  $\langle O(\mathbf{r}^4 + \mathbf{a}^4)O(\mathbf{r}^4) \rangle = 0$  for any primitive unit vector  $\mathbf{a}^4$  of the space-time lattice. Here  $\varphi_A$  denotes the orientation angle of one of the three particles in a unit cell. We find frozen disordered phases, for which the orientation order parameter between neighboring unit cells is uncorrelated  $\langle O(\mathbf{r}^4 + \mathbf{a}_D^4)O(\mathbf{r}^4) \rangle = 0$  for the disordered primitive unit vector  $\mathbf{a}_D^4$  direction but completely correlated (anticorrelated)  $\langle O(\mathbf{r}^4 + \mathbf{a}_F^4)O(\mathbf{r}^4) \rangle = \pm 1$  along the frozen lattice direction  $\mathbf{a}_F^4$  of the space-time lattice. The time translational symmetry of those frozen disordered phases is not broken if all primitive unit vectors, having a non-vanishing time component, are positively correlated frozen primitive unit vectors. These phases thus are not discrete time crystalline phases. In any other case the order is either a disordered time crystalline frozen space or a disordered space sub harmonic time crystalline order.

We also find completely ordered phases that are correlated (anticorrelated) in any of the space-time lattice directions. If the primitive unit vectors can be separated into primitive unit vectors along time and primitive unit vectors along space, we find non time crystals for which the order parameter correlation along the time direction is positive. Depending on the correlation in space we find positively correlated order of neighboring cells in which case the order is

*ferromagnetic* and neither the time nor the space translational symmetry is broken, or we find at least one anticorrelated space direction in which case the order is *antiferromagnetic* and the space translational symmetry is broken with an ordered primitive unit cell twice the size of a primitive unit cell of the driving lattice. If the order is antiferromagnetic in the direction of time we get a time crystal again with a unit cell twice the size of the primitive unit cell of the driving lattice. For a spatially ferromagnetic time crystal the primitive time unit vector of the order is double the primitive time unit vector of the drive. For a spatially antiferromagnetic time crystal the primitive unit vectors of the lattice are no longer separable into spatial and time-like unit vectors but they point along the diagonals between space and time similar to a sodium chloride structure in a spatial crystal.

Given the multitude of crystalline structures in space it should not surprise us that we also find a multitude of different more or less complex space-time structures. Next, we will show how to attain some of those structures in our colloidal model system.

## 5.2 Topologically isolating time crystals

The dipolar interaction is long range and anisotropic. Hence we can change the time crystalline behavior by filling unit cells of the pattern in an anisotropic way. We must avoid weak dipolar interaction because under such circumstance the regions where the unique conformation shown in Fig. 3c is adopted connects all bifurcation points and can no longer be circulated. When the dipolar interaction is moderate the inter-cellular interactions do not matter and the colloidal particles in one cell respond independently of those in the other cell. We hence find a time crystal with frozen spatial disorder. For the *a*-conformation at stronger dipolar interactions the degeneracy of the two distinct triangular conformations is broken and we can distinguish three types of bonds between neighboring cells (see Fig. 5). A *cc*-bond with two corners of neighboring triangles facing each other has a higher energy than the lowest energy *bb*-bond where two triangular bases face each other. A *bc*-bond has intermediate energy. Strong dipolar interactions can therefore also destroy the subharmonic response in ensembles of filled cells. The *a*-conformation is therefore not a good conformation for time crystals if all the flower shaped domains are occupied.

We consider fillings of cells such each filled cell has only bonds to filled neighboring cells where the bonds form an angle of  $2\pi/3$  or  $4\pi/3$ . Filled cells form a Kagome lattice (see Fig. 6) consisting of Kagome Wigner Seitz cells built from two filled (green and yellow) unit cells and one empty (gray) unit cell of the magnetic pattern. Under these conditions each filled cell is either a *b*-bonding or *c*-bonding cell exposing the same type of bond toward each of its occupied neighbor cells. When the splitting of bond energies due to intercellular dipole interactions are pronounced, a *bb*-bond cannot be converted into any other bond. This domination occurs for external fields that point in the surroundings of the single cell fence points in control space, where the symmetry of the continuously degenerate Goldstone mode can be easily broken by the intercellular dipole interactions. The inter-cellular dipole interaction perturbed fences in control space thus no longer coincide with the single cell unperturbed fence points but form closed curves  $\mathcal{F}_C^i(z_i)$ , that contain bifurcation points and that depend on the type  $i = 1, 2$  of the filled cell in the Kagome lattice as well as the number  $z_i$  of filled neighboring cells. Inside the fence of one cell only one minimum, namely the *b*-bond orientation of the triangles of the cell, exists and whenever crossing inside to this unique region the space-time crystal no longer responds with half the driving frequency.

For intermediate intercellular dipolar interaction strength, the same loop can enter the interior of the fence for one unit cell but not for another unit cell. In such cases one still finds a triangle in one cell responding with half the driving frequency and the triangle in the other cell responding with a trivial loop. The dynamics of the trivial responding cell is no longer adiabatic: When a *c*-bonding triangle is driven inside the unique *b*-bonding fenced region an

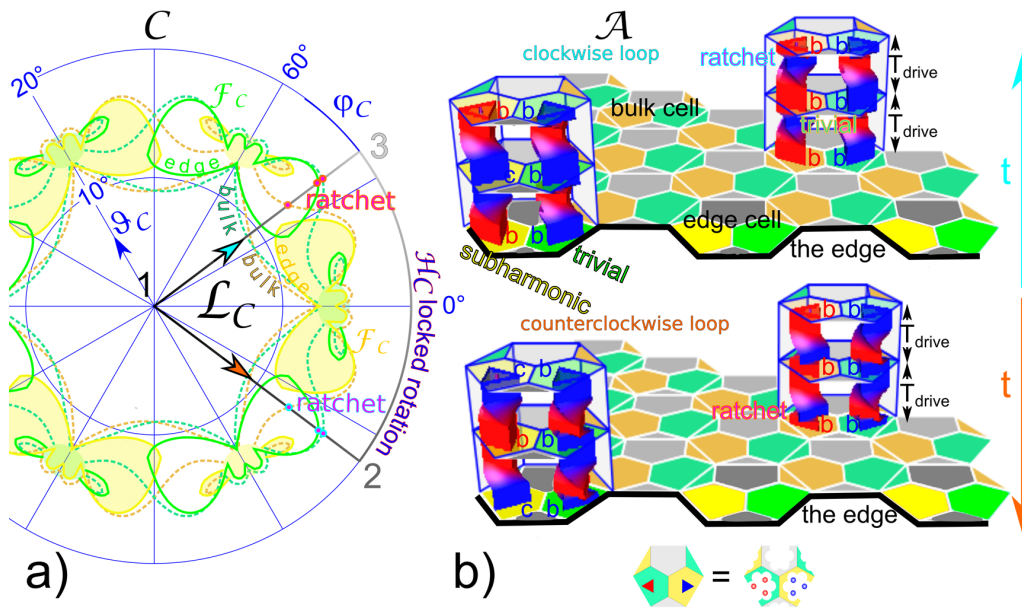


Figure 6: A complex topologically isolated space-time crystal in the a-conformation: **a)** A counterclockwise (clockwise) loop  $\mathcal{L}_C$  in control space  $\mathcal{C}$  circulates the solid yellow  $\mathcal{F}_C$ -edge fences, but cuts through the solid green  $\mathcal{F}_C$  edge-fences as well as through all dashed bulk fences. **b)** Snapshot of a space-time crystal of a hexagonal pattern with a Kagome-lattice of filled cells including the spatial edge of the lattice at the time when the loop is at the north pole. The space-Wigner-Seitz-cell of the Kagome lattice consists of two (green and yellow) filled cells and one empty (gray) cell. At the spatial edge (there is no edge in the direction of time) of the Kagome-ribbon, filled cells have a reduced  $z = 2$  configuration number. The bulk cells as well as the green edge cells relax into a spatial antiferromagnetic order of only  $b$ -bonding cells when the loop returns to the north-pole. The response of the yellow edge cells is subharmonic in time and the spatial disorder is frozen repeating in time with every second loop. We have depicted one edge-space-time Wigner-Seitz-cell and one bulk-space-time Wigner-Seitz-cell onto the Kagome lattice to show the dynamics of the triangle conformation. The sequence of conformations in the yellow edge cell is time reversal invariant, while the sequence of conformations in all other cells are not time reversal invariant. Two space-time-Wigner-Seitz edge cells can be packed side by side in space or with a symmorphic translation by one lattice vector in space and half a primitive vector in time creating the frozen disordered topological time crystalline edge wave in a). On the arXiv two video clips of the dynamics are provided with the videos [adFig6clockwise](#) and [adFig6counterclockwise](#).

irreversible ratchet jump of the triangle from the no longer stable  $c$ -bonding toward the  $b$ -bonding orientation occurs. The jump cannot be undone by backing up on the loop across the fence into the twofold orientation region outside the fenced region.

The response of the conformation of three colloidal particles in a particular unit cell  $i$  then depends on the configuration number  $z_i$ , i.e. the number of neighboring cells being also filled with three colloidal particles. The time crystalline topological response is robust for small configuration numbers  $z < 2$ . However the response changes for colloidal particles sitting in a bulk cell  $z = 3$  or at an arm-chair edge cell  $z = 2$  of a Kagome lattice. For intermediate dipolar interaction strength  $bb$ -bonds are converted to  $bb$ -,  $bc$ -, and  $cb$ -bonds rather than into  $cc$ -bonds, because only one of the edge cells responds as a subharmonic time crystal, while all

bulk cells and the other edge cell show trivial harmonic responses. Note that at the edge of a Kagome lattice the translation symmetry normal to the edge is explicitly broken, while the translation symmetry in time parallel to the edge is only broken due to the time crystalline response of the colloids inside the lattice. Within the bulk of the filled Kagome-lattice we distinguish 2 different filled ( $z = 3$ ) unit cells depending on the two possible directions of the neighboring cell triple. At an arm-chair edge of the Kagome lattice the configuration number of the outermost two cells reduces to  $z = 2$ . Each of these two cells have a somewhat different fence in control space for each of their possible configuration number. A triangle subject to a magnetic field  $\mathbf{H}_C$  tilted into a certain direction is displaced from the center of a flower in the same direction. If the tilt is toward a neighboring filled cell, then the unique  $b$ -bonding fenced region is larger than when the tilt is pointing away from the filled cell. For the same region in control space therefore the unique fenced region alternates in size as we move from one to a neighboring cell that has its bonds into the opposite directions. It is then easy to create a time crystal where e.g. only one of the edge cells has subharmonic response while the other cells respond in a trivial irreversible way. We can use these results to form an irreversible, i.e non-time reversal invariant, non-time bulk crystal, with time-crystalline edge states where the response in time and in space is quite complex.

In Fig. 6 we show the response of Kagome-lattice ribbon of two filled (green and yellow) cells and one empty (gray) cell to a control loop  $\mathcal{L}_C$  that consist of three sections. The control loop starts at the north pole (position 1) and moves at constant azimuth  $\varphi_C^i$  (measured with respect to the  $\mathbf{a}_1$  direction) toward the tilt angle  $\vartheta_C^{max}$  (position 2) where it turns to the final azimuth  $\varphi_C^f$  (position 3) before it returns to position 1 (the north pole). The values of  $\varphi_C^i$ ,  $\varphi_C^f$ , and  $\vartheta_C^{max}$  are chosen (simulation parameters see table 1 in appendix A) such that the loop circulates around the (yellow) numerically computed  $\mathcal{F}_C$ -edge-fences, but cutting through the green  $\mathcal{F}_C$ - edge-fences with the 12, and 31-sections of the loop. The loop also cuts through all the bulk fences but avoids unique regions inside the yellow edge-fences causing the adiabatic subharmonic response of the yellow edge cells, The triangles of paramagnetic particles in all bulk cells and in the green edge cells, however, perform a ratchet jump from a  $c$ -orientation toward a  $b$ -orientation whenever the particles in these cells are in the unstable  $c$ -orientation prior to the fence passing segment resulting in a trivial harmonic response to the loop. The irreversibility of the dynamics in the bulk cells and in the green edge cells becomes apparent when we reverse the driving loop causing the irreversible triangles of the time crystal to follow a sequence of orientations that is not the reversed sequence of the forward loop  $\mathcal{L}_A(\mathcal{L}_C^{-2}) \neq (\mathcal{L}_A(\mathcal{L}_C^2))^{-1}$ . Adiabatic response is time reversal invariant, while irreversible non-adiabatic motion is not. On the arXiv we show with the videos [adFig6clockwise](#) and [ad-Fig6counterclockwise](#) the full dynamics of the topological insulating time crystal shown in Fig. 6 for the counterclockwise  $\mathcal{L}_C$  as well as for the clockwise  $\mathcal{L}_C^{-1}$  driving loops.

The behavior of the irreversible cells is synchronized for all cells. Bulk cells and the green edge cells are all  $b$ -bonding when the loop returns to the north pole. The adiabatic (yellow) edge cells follow a subharmonic response whatever the initial order of the adiabatic cells were in the beginning. The adiabatic cells therefore are generically spatially disordered but time crystalline frozen as a function of time. The trivial edge cells and all bulk cells are spatially ordered in an antiferromagnetic order. It is an antiferromagnetic crystal with topologically protected time crystalline edge states.

### 5.3 Time crystalline phase transitions

In the  $Q$ -conformation at lower than universal elevation paramagnetic colloidal particles in neighboring unit cells can be arranged in either the trans-conformation (bond direction crossing the primitive unit vector connecting the neighboring cells) or in the cis-configuration (bond

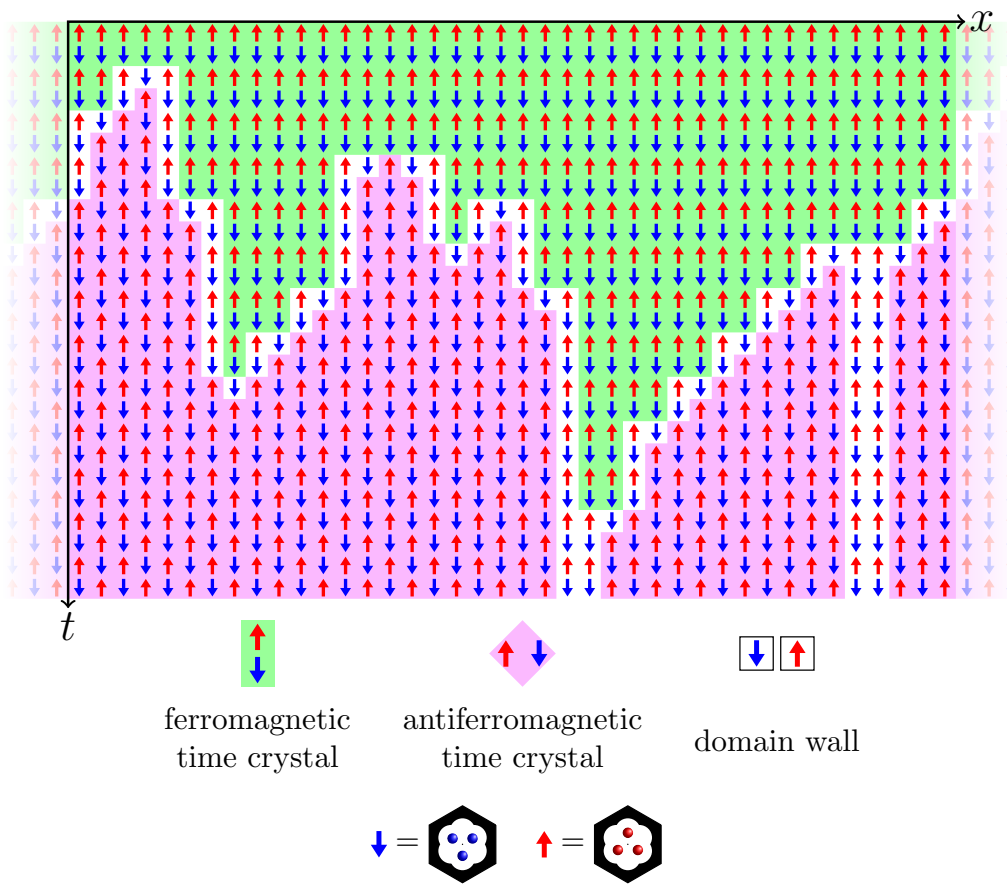


Figure 7: Stroboscopic development of a chain of honeycomb cells filled with three colloidal particles each. The initially ferromagnetic ordered time crystal undergoes a topological transition towards an antiferromagnetic time crystal. Space-time Wigner Seitz cells of the various orders are shown at the bottom. The spatial order in each cell is abbreviated by a blue or red arrow as indicated. A video clip of the dynamics is provided with the video [adFig7](#)

parallel to the cell connecting primitive unit vector) see Fig. 5. The trans-conformation has a lower energy than the cis-conformation. Hence, an antiferromagnetic ordering of the triangles along a row of unit cells is preferred. Neither a ferromagnetic nor an antiferromagnetic ordering suppress the time crystalline subharmonic behavior since in contrast to the behavior in the previous section, intercellular bonds between colloidal particles before and after an adiabatic driving cycle remain equivalent. In Fig. 7 we show the evolution of a ferromagnetic time crystal at time zero towards an antiferromagnetic time crystal for the simulation parameters listed in table 1 of appendix A. One row of neighboring cells along the  $\mathbf{a}_1$ -direction are filled with three particles each. The originally ferromagnetic time crystal remains in the ferromagnetic time crystalline order for a typical correlation time until a few antiferromagnetic time crystalline nuclei are formed. These nuclei grow and two more stable antiferromagnetic time crystalline ordered phases (of the same order but connected via a non-symmorphic translation that is part of the unbroken but not of the broken symmetry) separated by space like domain walls appear. They thus replace the old order with the new antiferromagnetic time crystalline order. The transition from the ferromagnetic towards the antiferromagnetic ordering is irreversible. In contrast to the time crystalline order in the a-conformation the space-time-bulk of the antiferromagnetic time crystal shows fully adiabatic response, and a forward or backward

loop  $\mathcal{L}_C$  or  $\mathcal{L}_C^{-1}$  results in a sequence of orientations that are the time reversed version of the other. A video clip of the full dynamics is shown in the video [adFig7](#).

The dipolar interaction couples the particles and broadens the one dimensional fence  $\mathcal{F}_C$  to a two dimensional object of control space. Here the intercellular dipolar interactions are strong enough to destroy the path connection of the ferromagnetic and antiferromagnetic conformations on  $\mathcal{M}_0$ . We can hence distinguish the fences  $\mathcal{F}_{\mathcal{M}_0^{a,f}}$  of the antiferromagnetic and the ferromagnetic stable conformations and the path disconnected subsets  $\mathcal{M}_0^{a,f}$  of the stable stationary manifolds enclosed by those fences. The only way to dynamically move from the ferromagnetic region  $\mathcal{M}_0^f$  toward the antiferromagnetic region  $\mathcal{M}_0^a$  is by driving the system toward the ferromagnetic fence  $\mathcal{F}_{\mathcal{M}_0^f} = \pi_C(\mathcal{F}_{\mathcal{M}_0^f})$  where a ratchet jump from  $\mathcal{F}_{\mathcal{M}_0^f}$  via  $\mathcal{C} \otimes \mathcal{A}$  into the lower potential subsection  $\mathcal{M}_0^a$  occurs. In our simulations the control loop  $\mathcal{L}_C$  circles around the ferromagnetic fence  $\mathcal{F}_{\mathcal{M}_0^f}$  by almost touching it such that the thermal fluctuation forces eventually drive the system across the fence. The persistence time of the ferromagnetic phase therefore sensitively depends on the proximity of the loop to the ferromagnetic fence as well as on the never truly adiabatic speed in passing this sensitive section of the loop. Once in the antiferromagnetic time crystalline phase one cannot return to the ferromagnetic conformation because there is no point of the antiferromagnetic fence that has a higher potential than the corresponding point of the ferromagnetic stable manifold  $\mathcal{M}_0^f$ . The antiferromagnetic phase therefore persists.

## 6 Conclusion

We have shown that the topology of the stationary manifold embedded in the product space of the external control variables and the quasistatic response variables determines whether a time crystalline driving is possible or not. Small thermal or quantum fluctuations will not change the topological phenomena since these are robust against weak perturbations. As long as transition or tunneling rates between the distinct minima are tiny, the time crystalline behavior will prevail also for a quantized version of the model. The essential requirement for the adiabatic time crystal to work is the non-ergodicity, i.e. the population of only one of the well separated minima. For these type of topological time crystals the quantum respectively classical nature of the phenomenon seems to be of minor importance. On a mesoscopic scale, proper cooling, necessary for any motor, whether in a quasi-equilibrated reversible cycle or driven far from thermal equilibrium is not a problem such that over heating [51–56] of the time crystal can be prevented. A rich variety of topologically induced non-time crystalline and time crystalline phases can be found both in the bulk or at the edge when playing with the competition of intra- and intercellular dipolar interactions between the paramagnetic colloidal particles of the many body ensemble.

## Acknowledgements

We thank Daniel de las Heras for scientific discussion, critical comments and help.

**Funding information** We acknowledge funding by the Deutsche Forschungsgemeinschaft (DFG, German Research Foundation) under project number 440764520.

## A Numerical details and parameters

The pattern magnetic field at the elevation  $z$  above the pattern reads

$$\mathbf{H}_p(\mathbf{x}_A, z) = \int \frac{(\mathbf{x}_A + z\mathbf{e}_z - \mathbf{x}'_A)}{4\pi((\mathbf{x}_A - \mathbf{x}'_A)^2 + z^2)^{3/2}} M_z(\mathbf{x}'_A) d^2\mathbf{x}'_A, \quad (2)$$

where

$$M_z(\mathbf{x}_A)\mathbf{e}_z = \begin{cases} +M_s\mathbf{e}_z & \text{if } |\mathbf{x}_A - \mathbf{a} - r_M\hat{\mathbf{e}}_i| < r_K \\ & \text{for one lattice vector } \mathbf{a} \\ & \text{and one normed primitive} \\ & \text{lattice vector } \hat{\mathbf{e}}_i (i = 1..6) \\ -M_s\mathbf{e}_z & \text{else} \end{cases}, \quad (3)$$

is the magnetization of the thin magnetic film with  $M_s$  the saturation magnetization,  $r_M = 0.2a$ ,  $r_K = 0.19a$ , and  $\hat{\mathbf{e}}_i = \mathbf{a}_i/a(\mathbf{Q}_i/Q)$  are normed vectors in the direction of the primitive unit vectors of the direct (reciprocal) lattice for the flower domains in the a-conformation (Q-conformation).

The single particle potential is

$$U = -\mu_0\mathbf{H}_p(\mathbf{x}_A, z) \cdot \mathbf{m}, \quad (4)$$

with  $\mathbf{m} = \chi_{eff}V\mathbf{H}_C$  the magnetic moment of the paramagnetic particle with volume  $V$  and effective magnetic susceptibility  $\chi_{eff}$ . The dipolar interaction reads

$$U_{dipol} = \frac{\mu_0}{4\pi} \frac{(\mathbf{x}_A - \mathbf{x}'_A)^2 \mathbf{m}^2 - 3((\mathbf{x}_A - \mathbf{x}'_A) \cdot \mathbf{m})^2}{|\mathbf{x}_A - \mathbf{x}'_A|^5}. \quad (5)$$

We use dimensionless units of length normalized to the lattice constant  $a$ , of the magnetic field normalized to the effectively attenuated magnetization  $M_{eff} = \gamma(\mathbf{Q}_1)M_s e^{-Qz}$  of a fictive universal pattern at elevation  $z$  with  $M_s$  the saturation magnetization of the real pattern,  $Q = 4\pi/\sqrt{3}a$  the modulus of the primitive reciprocal unit vectors, and  $\gamma(\mathbf{Q}_1) = \int_{WZ} e^{i\mathbf{Q}_1 \cdot \mathbf{x}_A} M_z(\mathbf{x}_A) d^2\mathbf{x}_A / M_s \frac{\sqrt{3}}{2} a^2 \approx 0.3$  the leading reciprocal lattice Fourier coefficient of both patterns, where the Fourier integral is taken over the Wigner Seitz cell  $WZ$  of each pattern. Units of energy are normalized to  $\mu_0 M_s^2 a^3$  and non dimensional effective magnetic susceptibilities  $\chi_{eff} V/a^3$ . Our control loops start at the north pole and move at constant azimuth  $\varphi_C^i$  (measured with respect to the  $\mathbf{a}_1$  direction) toward the tilt angle  $\vartheta_C^{max}$  where they turn to the final azimuth  $\varphi_C^f$  before they return to the north pole. In table 1 we list the parameters used to compute the time crystals shown in Figs. 4, 6, and 7.

Table 1: Simulation parameters

	$\frac{H_C \chi_{eff} V e^{4\pi z/\sqrt{3}a}}{\gamma(\mathbf{Q}_1) M_s a^3}$	$z/a$	$\varphi_C^i$	$\varphi_C^f$	$\vartheta_C^{max}$	conformation
Figure 4	$1.64 \cdot 10^{-1}$	universal	$-90^\circ$	$-30^\circ$	$23^\circ$	a, single cell
Figure 6	$1.09 \cdot 10^{-2}$	universal	$-37^\circ$	$37^\circ$	$20^\circ$	a
Figure 7	$6.5 \cdot 10^{-1}$	1/3	$71.7^\circ$	$124^\circ$	$33.2^\circ$	Q

All integrations were performed numerically using an Euler algorithm. Loops were followed adiabatically by reducing the speed of modulation to values that do no longer affect the outcome.

## References

- [1] F. Wilczek, *Quantum time crystals*, Phys. Rev. Lett. **109**, 160401 (2012), doi:[10.1103/PhysRevLett.109.160401](https://doi.org/10.1103/PhysRevLett.109.160401).
- [2] K. Sacha and J. Zakrzewski, *Time crystals: A review*, Rep. Prog. Phys. **81**, 016401 (2017), doi:[10.1088/1361-6633/aa8b38](https://doi.org/10.1088/1361-6633/aa8b38).
- [3] H. Watanabe and M. Oshikawa, *Absence of quantum time crystals*, Phys. Rev. Lett. **114**, 251603 (2015), doi:[10.1103/PhysRevLett.114.251603](https://doi.org/10.1103/PhysRevLett.114.251603).
- [4] J. Zhang et al., *Observation of a discrete time crystal*, Nature **543**, 217 (2017), doi:[10.1038/nature21413](https://doi.org/10.1038/nature21413).
- [5] T. Li, Z.-X. Gong, Z.-Q. Yin, H. T. Quan, X. Yin, P. Zhang, L.-M. Duan and X. Zhang, *Space-time crystals of trapped ions*, Phys. Rev. Lett. **109**, 163001 (2012), doi:[10.1103/PhysRevLett.109.163001](https://doi.org/10.1103/PhysRevLett.109.163001).
- [6] A. Shapere and F. Wilczek, *Classical time crystals*, Phys. Rev. Lett. **109**, 160402 (2012), doi:[10.1103/PhysRevLett.109.160402](https://doi.org/10.1103/PhysRevLett.109.160402).
- [7] T. L. Heugel, M. Oscity, A. Eichler, O. Zilberberg and R. Chitra, *Classical many-body time crystals*, Phys. Rev. Lett. **123**, 124301 (2019), doi:[10.1103/PhysRevLett.123.124301](https://doi.org/10.1103/PhysRevLett.123.124301).
- [8] J. Rovny, R. L. Blum and S. E. Barrett, *Observation of discrete-time-crystal signatures in an ordered dipolar many-body system*, Phys. Rev. Lett. **120**, 180603 (2018), doi:[10.1103/PhysRevLett.120.180603](https://doi.org/10.1103/PhysRevLett.120.180603).
- [9] N. Y. Yao, A. C. Potter, I.-D. Potirniche and A. Vishwanath, *Discrete time crystals: Rigidity, criticality, and realizations*, Phys. Rev. Lett. **118**, 030401 (2017), doi:[10.1103/PhysRevLett.118.030401](https://doi.org/10.1103/PhysRevLett.118.030401).
- [10] D. V. Else, B. Bauer and C. Nayak, *Floquet time crystals*, Phys. Rev. Lett. **117**, 090402 (2016), doi:[10.1103/PhysRevLett.117.090402](https://doi.org/10.1103/PhysRevLett.117.090402).
- [11] D. V. Else, B. Bauer and C. Nayak, *Prethermal phases of matter protected by time-translation symmetry*, Phys. Rev. X **7**, 011026 (2017), doi:[10.1103/PhysRevX.7.011026](https://doi.org/10.1103/PhysRevX.7.011026).
- [12] A. Libál, T. Balázs, C. Reichhardt and C. J. O. Reichhardt, *Colloidal dynamics on a choreographic time crystal*, Phys. Rev. Lett. **124**, 208004 (2020), doi:[10.1103/PhysRevLett.124.208004](https://doi.org/10.1103/PhysRevLett.124.208004).
- [13] A. Kuroś, R. Mukherjee, W. Golletz, F. Sauvage, K. Giergiel, F. Mintert and K. Sacha, *Phase diagram and optimal control for n-tupling discrete time crystal*, New J. Phys. **22**, 095001 (2020), doi:[10.1088/1367-2630/abb03e](https://doi.org/10.1088/1367-2630/abb03e).
- [14] K. Giergiel, A. Kosior, P. Hannaford and K. Sacha, *Time crystals: Analysis of experimental conditions*, Phys. Rev. A **98**, 013613 (2018), doi:[10.1103/PhysRevA.98.013613](https://doi.org/10.1103/PhysRevA.98.013613).
- [15] M. Faraday, *On a peculiar class of acoustical figures; and on certain forms assumed by groups of particles upon vibrating elastic surfaces*, Phil. Trans. R. Soc. **121**, 299 (1831), doi:[10.1098/rstl.1831.0018](https://doi.org/10.1098/rstl.1831.0018).
- [16] A. Steane, P. Szriftgiser, P. Desbiolles and J. Dalibard, *Phase modulation of atomic de Broglie waves*, Phys. Rev. Lett. **74**, 4972 (1995), doi:[10.1103/PhysRevLett.74.4972](https://doi.org/10.1103/PhysRevLett.74.4972).

- [17] T. M. Roach, H. Abele, M. G. Boshier, H. L. Grossman, K. P. Zetie and E. A. Hinds, *Realization of a magnetic mirror for cold atoms*, Phys. Rev. Lett. **75**, 629 (1995), doi:[10.1103/PhysRevLett.75.629](https://doi.org/10.1103/PhysRevLett.75.629).
- [18] N. Westbrook et al., *New physics with evanescent wave atomic mirrors: The van der Waals force and atomic diffraction*, Phys. Scripta **T78**, 7 (1998), doi:[10.1238/physica.topical.078a00007](https://doi.org/10.1238/physica.topical.078a00007).
- [19] D. C. Lau, A. I. Sidorov, G. I. Opat, R. J. McLean, W. J. Rowlands and P. Hannaford, *Reflection of cold atoms from an array of current-carrying wires*, Eur. Phys. J. D - Atomic, Molecular and Optical Physics **5**, 193 (1999), doi:[10.1007/s100530050244](https://doi.org/10.1007/s100530050244).
- [20] K. Bongs, S. Burger, G. Birkl, K. Sengstock, W. Ertmer, K. Rzazewski, A. Sanpera and M. Lewenstein, *Coherent evolution of bouncing Bose-Einstein condensates*, Phys. Rev. Lett. **83**, 3577 (1999), doi:[10.1103/PhysRevLett.83.3577](https://doi.org/10.1103/PhysRevLett.83.3577).
- [21] A. I. Sidorov, R. J. McLean, F. Scharnberg, D. S. Gough, T. J. Davis, B. J. Sexton, G. I. Opat and Hannaford, *Permanent-magnet microstructures for atom optics*, Acta Phys. Pol. B **33**, 2137 (2002).
- [22] J. Fiutowski, D. Bartoszek-Bober, T. Dohnalik and T. Kawalec, *Evanescent wave mirror for cold atoms—A quasi-resonant case*, Optics Communications **297**, 59 (2013), doi:[10.1016/j.optcom.2013.01.066](https://doi.org/10.1016/j.optcom.2013.01.066).
- [23] T. Kawalec, D. Bartoszek-Bober, R. Panaś, J. Fiutowski, A. Pławecka and H.-G. Rubahn, *Optical dipole mirror for cold atoms based on a metallic diffraction grating*, Opt. Lett. **39**, 2932 (2014), doi:[10.1364/OL.39.002932](https://doi.org/10.1364/OL.39.002932).
- [24] S. Choi et al., *Observation of discrete time-crystalline order in a disordered dipolar many-body system*, Nature **543**, 221 (2017), doi:[10.1038/nature21426](https://doi.org/10.1038/nature21426).
- [25] S. Pal, N. Nishad, T. S. Mahesh and G. J. Sreejith, *Temporal order in periodically driven spins in star-shaped clusters*, Phys. Rev. Lett. **120**, 180602 (2018), doi:[10.1103/PhysRevLett.120.180602](https://doi.org/10.1103/PhysRevLett.120.180602).
- [26] J. Smits, L. Liao, H. T. C. Stoof and P. van der Straten, *Observation of a space-time crystal in a superfluid quantum gas*, Phys. Rev. Lett. **121**, 185301 (2018), doi:[10.1103/PhysRevLett.121.185301](https://doi.org/10.1103/PhysRevLett.121.185301).
- [27] V. K. Kozin and O. Kyriienko, *Quantum time crystals from Hamiltonians with long-range interactions*, Phys. Rev. Lett. **123**, 210602 (2019), doi:[10.1103/PhysRevLett.123.210602](https://doi.org/10.1103/PhysRevLett.123.210602).
- [28] R. Hurtado-Gutiérrez, F. Carollo, C. Pérez-Espigares and P. I. Hurtado, *Building continuous time crystals from rare events*, Phys. Rev. Lett. **125**, 160601 (2020), doi:[10.1103/PhysRevLett.125.160601](https://doi.org/10.1103/PhysRevLett.125.160601).
- [29] J. Dai, A. J. Niemi and X. Peng, *Classical Hamiltonian time crystals-general theory and simple examples*, New J. Phys. **22**, 085006 (2020), doi:[10.1088/1367-2630/aba8d3](https://doi.org/10.1088/1367-2630/aba8d3).
- [30] J. Loehr et al., *Lattice symmetries and the topologically protected transport of colloidal particles*, Soft Matter **13**, 5044 (2017), doi:[10.1039/C7SM00983F](https://doi.org/10.1039/C7SM00983F).
- [31] D. de las Heras, J. Loehr, M. Loenne and T. M. Fischer, *Topologically protected colloidal transport above a square magnetic lattice*, New J. Phys. **18**, 105009 (2016), doi:[10.1088/1367-2630/18/10/105009](https://doi.org/10.1088/1367-2630/18/10/105009).

- [32] J. Loehr, M. Loenne, A. Ernst, D. de las Heras and T. M. Fischer, *Topological protection of multiparticle dissipative transport*, Nat. Commun. **7**, 11745 (2016), doi:[10.1038/ncomms11745](https://doi.org/10.1038/ncomms11745).
- [33] H. Massana-Cid et al., *Edge transport at the boundary between topologically equivalent lattices*, Soft Matter **15**, 1539 (2019), doi:[10.1039/C8SM02005A](https://doi.org/10.1039/C8SM02005A).
- [34] J. Loehr et al., *Colloidal topological insulators*, Commun. Phys. **1**, 4 (2018), doi:[10.1038/s42005-017-0004-1](https://doi.org/10.1038/s42005-017-0004-1).
- [35] M. Mirzaee-Kakhki, A. Ernst, D. de las Heras, M. Urbaniak, F. Stobiecki, J. Gördes, M. Reginka, A. Ehresmann and T. M. Fischer, *Simultaneous polydirectional transport of colloidal bipeds*, Nat. Commun. **11**, 4670 (2020), doi:[10.1038/s41467-020-18467-9](https://doi.org/10.1038/s41467-020-18467-9).
- [36] A. M. E. B. Rossi, J. Bugase and T. M. Fischer, *Macroscopic Floquet topological crystalline steel and superconductor pump*, Europhys. Lett. **119**, 40001 (2017), doi:[10.1209/0295-5075/119/40001](https://doi.org/10.1209/0295-5075/119/40001).
- [37] A. M. E. B. Rossi, J. Bugase, T. Lachner, A. Ernst, D. de las Heras and T. M. Fischer, *Hard topological versus soft geometrical magnetic particle transport*, Soft Matter **15**, 8543 (2019), doi:[10.1039/C9SM01401B](https://doi.org/10.1039/C9SM01401B).
- [38] M. C. Rechtsman, J. M. Zeuner, Y. Plotnik, Y. Lumer, D. Podolsky, F. Dreisow, S. Nolte, M. Segev and A. Szameit, *Photonic Floquet topological insulators*, Nature **496**, 196 (2013), doi:[10.1038/nature12066](https://doi.org/10.1038/nature12066).
- [39] M. Xiao, G. Ma, Z. Yang, P. Sheng, Z. Q. Zhang and C. T. Chan, *Geometric phase and band inversion in periodic acoustic systems*, Nat. Phys. **11**, 240 (2015), doi:[10.1038/nphys3228](https://doi.org/10.1038/nphys3228).
- [40] A. Murugan and S. Vaikuntanathan, *Topologically protected modes in non-equilibrium stochastic systems*, Nat. Commun. **8**, 13881 (2017), doi:[10.1038/ncomms13881](https://doi.org/10.1038/ncomms13881).
- [41] C. L. Kane and T. C. Lubensky, *Topological boundary modes in isostatic lattices*, Nat. Phys. **10**, 39 (2013), doi:[10.1038/nphys2835](https://doi.org/10.1038/nphys2835).
- [42] J. Paulose, B. Gin-ge Chen and V. Vitelli, *Topological modes bound to dislocations in mechanical metamaterials*, Nat. Phys. **11**, 153 (2015), doi:[10.1038/nphys3185](https://doi.org/10.1038/nphys3185).
- [43] L. M. Nash, D. Kleckner, A. Read, V. Vitelli, A. M. Turner and W. T. M. Irvine, *Topological mechanics of gyroscopic metamaterials*, Proc. Natl. Acad. Sci. U.S.A. **112**, 14495 (2015), doi:[10.1073/pnas.1507413112](https://doi.org/10.1073/pnas.1507413112).
- [44] S. D. Huber, *Topological mechanics*, Nat. Phys. **12**, 621 (2016), doi:[10.1038/nphys3801](https://doi.org/10.1038/nphys3801).
- [45] M. Z. Hasan and C. L. Kane, *Colloquium: Topological insulators*, Rev. Mod. Phys. **82**, 3045 (2010), doi:[10.1103/RevModPhys.82.3045](https://doi.org/10.1103/RevModPhys.82.3045).
- [46] S.-Q. Shen, *Topological insulators*, Springer Berlin Heidelberg, Berlin, Heidelberg, ISBN 9783642328572 (2012), doi:[10.1007/978-3-642-32858-9](https://doi.org/10.1007/978-3-642-32858-9).
- [47] C. Chappert et al., *Planar patterned magnetic media obtained by ion irradiation*, Science **280**, 1919 (1998), doi:[10.1126/science.280.5371.1919](https://doi.org/10.1126/science.280.5371.1919).
- [48] P. Kuświk et al., *Colloidal domain lithography for regularly arranged artificial magnetic out-of-plane monodomains in Au/Co/Au layers*, Nanotechnology **22**, 095302 (2011), doi:[10.1088/0957-4484/22/9/095302](https://doi.org/10.1088/0957-4484/22/9/095302).

- [49] J. Goldstone, *Field theories with “superconductor” solutions*, Nuovo Cim. **19**, 154 (1961), doi:[10.1007/BF02812722](https://doi.org/10.1007/BF02812722).
- [50] S. Hermann and M. Schmidt, *Noether’s theorem in statistical mechanics*, Commun. Phys. **4**, 176 (2021), doi:[10.1038/s42005-021-00669-2](https://doi.org/10.1038/s42005-021-00669-2).
- [51] T. Prosen, *Time evolution of a quantum many-body system: Transition from integrability to ergodicity in the thermodynamic limit*, Phys. Rev. Lett. **80**, 1808 (1998), doi:[10.1103/PhysRevLett.80.1808](https://doi.org/10.1103/PhysRevLett.80.1808).
- [52] T. Prosen, *Ergodic properties of a generic nonintegrable quantum many-body system in the thermodynamic limit*, Phys. Rev. E **60**, 3949 (1999), doi:[10.1103/PhysRevE.60.3949](https://doi.org/10.1103/PhysRevE.60.3949).
- [53] L. D’Alessio and M. Rigol, *Long-time behavior of isolated periodically driven interacting lattice systems*, Phys. Rev. X **4**, 041048 (2014), doi:[10.1103/PhysRevX.4.041048](https://doi.org/10.1103/PhysRevX.4.041048).
- [54] A. Lazarides, A. Das and R. Moessner, *Equilibrium states of generic quantum systems subject to periodic driving*, Phys. Rev. E **90**, 012110 (2014), doi:[10.1103/PhysRevE.90.012110](https://doi.org/10.1103/PhysRevE.90.012110).
- [55] M. Bukov, L. D’Alessio and A. Polkovnikov, *Universal high-frequency behavior of periodically driven systems: From dynamical stabilization to Floquet engineering*, Adv. Phys. **64**, 139 (2015), doi:[10.1080/00018732.2015.1055918](https://doi.org/10.1080/00018732.2015.1055918).
- [56] B. Ye, F. Machado and N. Y. Yao, *Floquet phases of matter via classical prethermalization*, Phys. Rev. Lett. **127**, 140603 (2021), doi:[10.1103/PhysRevLett.127.140603](https://doi.org/10.1103/PhysRevLett.127.140603).

# Publication 2

---

## Hard topological versus soft geometrical magnetic particle transport

*Soft Matter* **15**, 8543–8551 (2019)

Anna M. E. B. Rossi,<sup>a1</sup> Jonas Bugase,<sup>a1,b</sup>  
Thomas Lachner,<sup>a1</sup> **Adrian Ernst**,<sup>a1</sup>  
Daniel de las Heras,<sup>a2</sup> & Thomas M. Fischer<sup>a1</sup>

<sup>a1</sup> Experimental Physics X and <sup>a2</sup> Theoretical Physics II, Department of Physics, University of Bayreuth, 95447 Bayreuth, Germany.

<sup>b</sup> Department of Applied Physics, University for Development Studies, Tamale, Ghana.

---

I did previously work on single particles using the sixfold lattice[43] where the topological protection was lost with very high thermal noise, making the transport directions statistically distributed. I was curious if the topological character of the transport can get lost in other ways. The following publication describes such a phenomenon, the transition from the topological towards a geometrical transport.

### My Contribution

Anna Rossi built the device and performed the experiments together with Jonas Bugase and Thomas Lachner. I performed the simulations of the transport of  $n > 1$  particles per unit cell. Daniel de las Heras supervised the simulations and Thomas Fischer the experiments. The preparation and writing of the paper was done by all authors.





Cite this: *Soft Matter*, 2019,  
15, 8543

## Hard topological *versus* soft geometrical magnetic particle transport†

Anna M. E. B. Rossi,<sup>a</sup> Jonas Bugase,<sup>ab</sup> Thomas Lachner,<sup>id</sup><sup>a</sup> Adrian Ernst,<sup>a</sup>  
Daniel de las Heras<sup>id</sup><sup>c</sup> and Thomas M. Fischer<sup>id</sup><sup>\*a</sup>

The question of how a dissipative geometrical transport system changes towards a topological transport system is important to render a fragile transport into a robust transport. We show how a macroscopic magnetic topological transport of solid state spheres changes to a geometrical transport of ferrofluid droplets, when instead of a solid state object, soft matter is transported. The key difference when comparing solid objects with fluid droplets is the possibility to split a ferrofluid droplet into two droplets. It is shown how this fundamental difference also fundamentally changes the transport properties. Hence, experimentally and theoretically the transport on top of a periodic two-dimensional hexagonal magnetic pattern of (i) a single macroscopic steel sphere, (ii) a doublet of wax/magnetite composite spheres, and (iii) an immiscible mixture of ferrofluid droplets with a perfluorinated liquid is analyzed. The transport of all these magnetic objects is achieved by moving an external permanent magnet on a closed modulation loop around the two-dimensional magnetic pattern. The transport of one and also that of two objects per unit cell is topologically protected and characterized by discrete displacements of the particles as we continuously scan through a family of modulation loops. The direction and the type of transport are characterized by the winding numbers of the modulation loops around special objects in control space, which is the space for the possible directions of the external magnetic field. The winding numbers necessary for characterizing the topological transport increase with the number of particles per unit cell. The topological character of the transport is destroyed, when transporting a large collection of particles per unit cell, like it is in the case of a macroscopic assembly of magnetic nanoparticles in a ferrofluid droplet for which the transport is geometrical and no longer topological. To characterize the change in the transport from topological to geometrical, we perform computer simulations of the transport of an increasing number of particles per unit cell.

Received 10th July 2019,  
Accepted 4th October 2019

DOI: 10.1039/c9sm01401b

rsc.li/soft-matter-journal

## 1 Introduction

When a system is driven adiabatically, its state changes slower than any relaxation time. The state of a classical system then follows the same path independently of the speed of driving. If driven adiabatically at different speeds, the state of a quantum system also follows the same path up to the global dynamic phase<sup>1</sup> of its wave function that cannot be measured. Measurable quantities are geometrical in the adiabatic limit, since they can be deduced from the path without the knowledge of a particular time table with which one drives the system along this path. For a

periodically driven system, the transport of particles over a period then is proportional to the geometric quantity of the loop of the driving field.<sup>2–4</sup> For example, autonomous low Reynolds number swimmers propel by a distance proportional to the area of the driving control loop in shape space.<sup>5,6</sup> Adiabatic quantum two-band electrons propel by an amount proportional to the area enclosed by the  $SU(2)$ , respectively  $SO(3) \cong SU(2)/\mathbb{Z}_2$  matrices of the periodic control loop induced by the external field.<sup>1,7</sup>

The area of a loop is a geometric quantity that continuously changes when the driving control loop is altered. When symmetries or other conditions constraint the driving loop, the geometrical properties might become discrete global properties, called topological invariants. Then, the transport no longer changes continuously with the loop since families of loops share the same topological invariant. The transport changes discretely between two families of loops with different values of the topological invariant.<sup>7</sup> The transport is robust because it is

<sup>a</sup> *Experimentalphysik X, Physikalisches Institut, Universität Bayreuth, D-95440 Bayreuth, Germany. E-mail: Thomas.Fischer@uni-bayreuth.de*

<sup>b</sup> *University for Development Studies, Department of Applied Physics, Tamale, Ghana*

<sup>c</sup> *Theoretische Physik II, Physikalisches Institut, Universität Bayreuth, D-95440 Bayreuth, Germany*

† Electronic supplementary information (ESI) available. See DOI: 10.1039/c9sm01401b

topologically protected. For example, in a nucleus one nucleon must rotate by multiples of  $2\pi$  when it propels by one lattice constant above the lattice of the crystallized nucleons that form the rest of the nucleus.<sup>8</sup>

Understanding how a system changes from geometrical towards topological is important. With this knowledge we can change a fragile, geometric transport into a robust topological transport. For example, in the quantum Hall effect steps between the plateaus in the conductivity can be created either by lowering the temperature or by using clean systems with fewer impurities.<sup>9</sup> Both methods decrease the probability of exciting unoccupied bulk Landau levels and thus make the system topological. For many quantum and classical systems,<sup>10–15</sup> the transition from geometric towards topological transport can be understood *via* the amount of dissipation occurring due to the scattering between states. It has, however, been shown that there exist non-Hermitian quantum and dissipative classical topological transport systems,<sup>16–20</sup> where it is precisely the dissipation that causes the topological character of the transport. For these systems the transition from topological towards geometrical must be different.

The purpose of this work is to show how topological transport phenomena also play a role in soft matter systems. We show experimentally and with computer simulations that a macroscopic topological magnetic particle pump,<sup>21</sup> which transports paramagnetic or soft magnetic particles across a magnetic lattice, is topological when transporting a small number of particles per unit cell. The transport is robust for the modulation loops of a driving homogeneous external field that share the same topological invariant. Subclasses of modulation loops appear for a loading with two or more particles per unit cell, increasing

the number of discrete steps. However, for loadings with a macroscopic ensemble of magnetic nanoparticles, such as a ferrofluid droplet, the topological nature of the transport is destroyed and becomes geometrical.

## 2 Topogeometrical pump

The system consists of a two-dimensional hexagonal magnetic pattern made of up- and down-magnetized magnets, see Fig. 1a. The pattern creates a two-dimensional magnetic potential that acts on paramagnetic objects located above the pattern at fixed elevation. The potential is a function of the position  $\mathbf{x}_A \in \mathcal{A}$  of the paramagnetic object in action space  $\mathcal{A}$ , which is the plane parallel to the pattern in which the objects are located. A uniform external magnetic field is also applied to the system. Hence, the total potential depends parametrically on the direction of the superimposed external magnetic field. Paramagnetic objects, such as soft magnetic spheres and ferrofluid droplets move in action space when we adiabatically modulate the total potential by changing the direction of the uniform external field.

Our two dimensional magnetic hexagonal lattice is built from an arrangement of NbB-magnets<sup>21</sup> (Fig. 1a). The arrangement is such that the primitive unit cell of the lattice is a sixfold symmetric  $C_6$  hexagon with corners centered within the smaller magnets, see Fig. 1b. Each unit cell thus contains one large magnet and two small magnets. The total magnetic field is the sum of the pattern  $\mathbf{H}_p$  and the external  $\mathbf{H}_{\text{ext}}$  contributions

$$\mathbf{H} = \mathbf{H}_p + \mathbf{H}_{\text{ext}}. \quad (1)$$

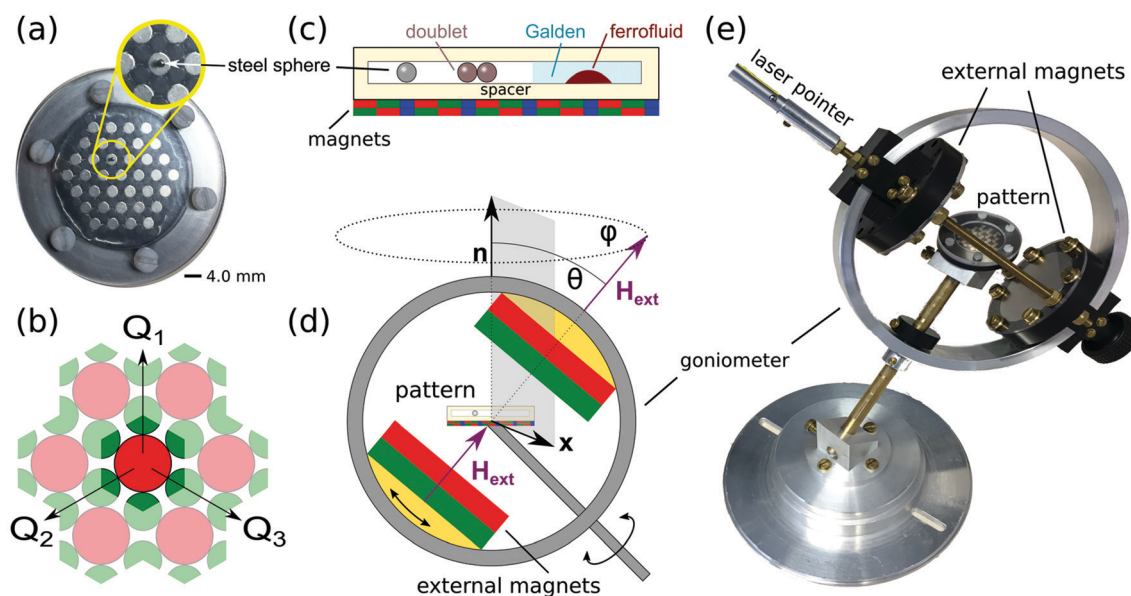


**Fig. 1** Experimental setup: (a) top view of the hexagonal magnetic pattern. The inset is a close view of the transported steel sphere. (b) Scheme of the position and the orientation of the magnets. The silver areas in the sample (red areas in the scheme) are magnetized up. The black (green) areas are magnetized down. One unit cell is emphasized in full colors. The vector  $\mathbf{Q}_1$  is one of the primitive reciprocal lattice vectors. (c) Side view of the pattern and the compartment holding either one steel sphere, two wax spheres, or Galden and a ferrofluid. (d) Schematic of the goniometer and the external magnets surrounding the sample. (e) A photo of the setup.

The potential energy of a paramagnetic object in the total magnetic field  $H$  is proportional to the square of the magnetic field

$$U(\mathbf{x}_A) \propto -\mathbf{H}^2, \quad (2)$$

and it can be decomposed into a discrete Fourier series of contributions from reciprocal lattice vectors.<sup>17,23</sup> The Fourier series of the potential evaluated in a plane above the pattern and parallel to it is the square of the Fourier series of the magnetization of the pattern augmented by the external field. As a function of elevation, the higher Fourier coefficients are attenuated more than those with lower reciprocal vectors. At the experimental elevation (comparable to the length of the unit cell of the pattern), only the “universal” contributions to the potential from the lowest non-zero reciprocal lattice vectors remain relevant.<sup>17,23</sup> The purpose of the spacer (Fig. 1c) is thus to render the potential universal such that only the symmetry and not the fine details of the pattern are important.

We either place one steel sphere or two spheres consisting of a mixture of wax and magnetite on top of the spacer. Alternatively, we fill a closed compartment with a mixture of a nonmagnetic fluid (Galden) and an aqueous ferrofluid, immiscible with the Galden. The choice of particles and ferrofluids to be transported is made in a way as to suppress dipolar interactions and fingering instabilities<sup>24,25</sup> that are known to govern the behavior of ferrofluids at stronger magnetic fields. The magnetic pattern with the transported paramagnetic object on top is then placed in the center of a goniometer. Both, a sketch and an actual picture of the setup are shown in Fig. 1d and e, respectively. The goniometer holds two large NbB-magnets that generate the external field. The magnets are aligned parallel to each other and create an external magnetic field of magnitude  $\mu_0 H_{\text{ext}} = 45$  mT that penetrates the two-dimensional pattern, the steel sphere, the wax/magnetite spheres, and the ferrofluid droplets. The dipolar interactions between two wax/magnetite spheres or between ferrofluid nanoparticles are weak compared to the interaction with the pattern and the external field.

The gradient of the magnitude of the external field at the position of the transported objects  $\nabla H_{\text{ext}} \approx M_{\text{ext}} t_{\text{ext}} d_{\text{ext}}^2 / R^4$  is at least two orders of magnitude smaller than that of the magnetic field of the pattern  $\nabla H_p \approx (M_1 + M_s) / a$ . Hence, the field created by the external magnets is effectively uniform. The two external magnets can be oriented to produce an arbitrary direction of the external magnetic field with respect to the pattern. A laser pointing along  $H_{\text{ext}}$  is mounted on the goniometer, see Fig. 1e, to create a stereographic projection of the instantaneous external magnetic field direction on the recording plane.

### 3 Topologically nontrivial transport loops

The parametric dependence of the potential acting on a paramagnetic object (eqn (2)) was studied in detail in ref. 17. The potential has a hexagonal symmetry and the number of minima per unit cell of the potential can be one or two, depending on the orientation of the uniform external field. The set of possible

orientations of the external field forms a sphere that we call the control space  $\mathcal{C}$  (see Fig. 2b). Two minima exist in the excess region of  $\mathcal{C}$  (see Fig. 2b) in which the orientation of the external field is roughly antiparallel to the magnetization  $\mathbf{M}_1$  of the silver magnets in Fig. 2a. Only one minimum of the potential exists for the orientations of the external field roughly parallel to the magnetization of silver magnets (see the green region of the control space in Fig. 2b). The boundary in  $\mathcal{C}$  between the excess region and the region of one single minimum is a closed curve in  $\mathcal{C}$  that we call the fence  $\mathcal{F}$ . The fence consists of twelve segments (red and blue in Fig. 2b) meeting in twelve bifurcation points. These bifurcation points ( $\mathcal{B}_{+a_i}$ , and  $\mathcal{B}_{+Q_i}$ ) are located in the southern hemisphere of  $\mathcal{C}$  on longitudes running through the directions  $\pm \mathbf{a}_i$  and  $\pm \mathbf{Q}_i$  ( $i = 1, 2, 3$ ) of the primitive unit vectors of the direct and reciprocal lattice, respectively (see Fig. 2a and b). The fence segments are of two types  $+\mathbf{Q}$ -segments (red segments in Fig. 2b) and  $-\mathbf{Q}$ -segments (blue segments in Fig. 2b).

We reorient the external magnets by moving along a closed reorientation loop that starts and ends at the same orientation. (See the black point in Fig. 2b marked as the starting point between  $\mathbf{Q}_2$  and the  $\mathbf{a}_3$  longitude in the southern unique minimum region.) As a result of the reorientation loop of the external field, the steel sphere, the wax/magnetite spheres, and the ferrofluid droplets move above the magnetic lattice. A motion of the steel sphere is topologically trivial when the sphere responds to a closed reorientation loop with a closed loop on the lattice. Not every closed reorientation loop causes such a trivial response of the steel sphere. There are topologically nontrivial trajectories, where the steel sphere ends at a position differing from the initial position by one unit vector of the magnetic lattice. Nontrivial closed reorientation loops in control space are those loops that have loop segments in both the excess region and the region of the unique minimum.<sup>17,21</sup> Here, the reorientation loop enters the excess region with a longitude  $\phi_{\text{entry}}$  between the  $\mathbf{Q}_2$  and the  $-\mathbf{a}_2$  directions and exits the excess region between the  $\mathbf{Q}_2$  and the  $\mathbf{a}_3$  longitudes at  $\phi_{\text{exit}} = 4.4\pi/6$ . The schematic reorientation loops in control space are depicted in Fig. 2b.

#### 3.1 Single steel sphere transport

We have reported in ref. 17, 21 and 22 how the transport of a single paramagnetic particle changes as we move the entry longitude  $4.4\pi/6 < \phi_{\text{entry}} < 8.5\pi/6$  of the reorientation closed loop. Here we briefly repeat the findings which are important for this work. The steel sphere adiabatically returns to its initial position (performs a closed loop above the lattice) if the reorientation loop enters and exits the excess region *via* the same fence segment. As an example of such a loop we have drawn the loop  $a$  in Fig. 2b for which  $\phi_{\text{entry}} = \phi_{\text{exit}} = 4.4\pi/6$ . The sphere also returns to the same position when the reorientation loop encloses only the bifurcation point  $\mathcal{B}_{a_3}$  or the two bifurcation points  $\mathcal{B}_{a_3}$  and  $\mathcal{B}_{-Q_1}$  in  $\mathcal{C}$  such as in the case of loops b–e ( $5\pi/6 < \phi_{\text{entry}} < 7\pi/6$  and  $\phi_{\text{exit}} = 4.4\pi/6$ ) in Fig. 2b. However, as the modulation loop encloses  $\mathcal{B}_{a_3}$  the motion is no longer adiabatic. Instead, an irreversible ratchet jump occurs as the modulation loop exits the excess region through the fence.

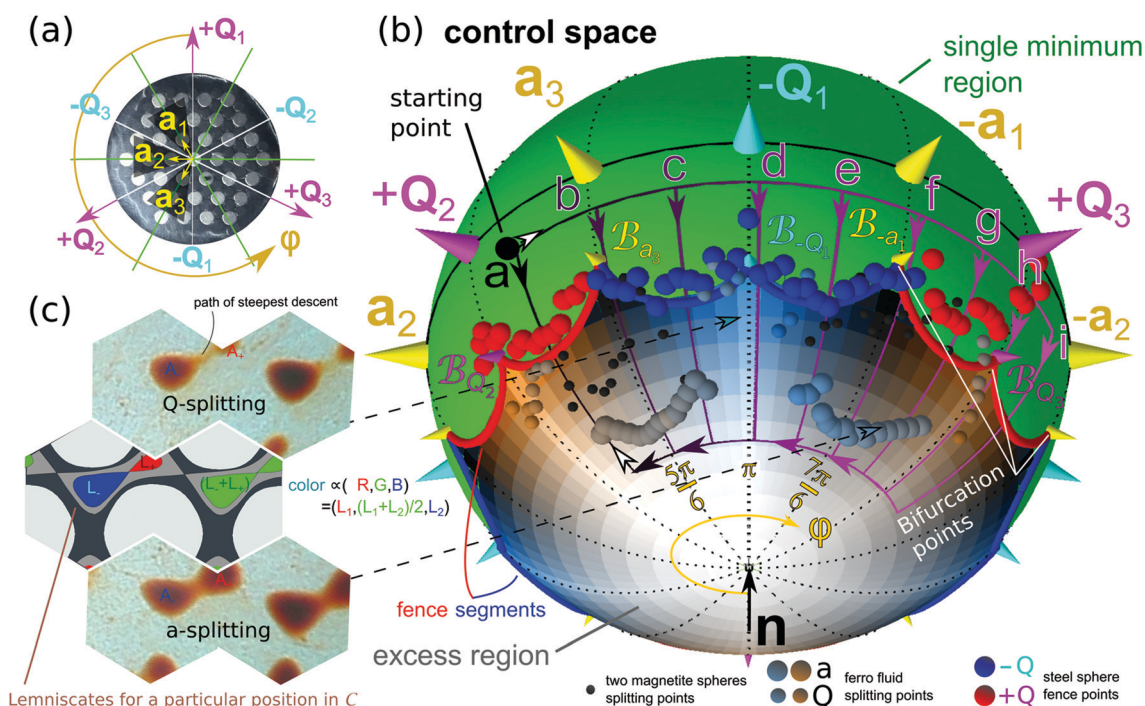


**Fig. 2** Orientation of the pattern, the corresponding orientations of the external field in control space and the different events occurring for single steel spheres, wax/magnetite-doublers, and ferrofluid droplets upon the family of modulation loops applied in the experiments. (a) Direction of the primitive unit vectors  $\mathbf{a}_1$ ,  $\mathbf{a}_2$ , and  $\mathbf{a}_3$  of the direct lattice and direction of the primitive unit vectors  $\mathbf{Q}_1$ ,  $\mathbf{Q}_2$ , and  $\mathbf{Q}_3$  of the reciprocal lattice. (b) Control space of the hexagonal lattice. Theoretical fences between the region of one unique minimum (green) and the excess region for paramagnetic objects are shown as red ( $+\mathbf{Q}$  segments) and blue ( $-\mathbf{Q}$  segments) lines. The experimental fence data from the single steel spheres are shown as red and blue spheres. The experiments are performed with modulation loops (a–i) that start at the big black circle (starting point) and enter the excess region in the south of  $\mathcal{C}$  along a longitude between the  $\mathbf{Q}_2$  and the  $-\mathbf{a}_2$  longitudes through either a red or blue fence segment. The loops exit this region and return to the starting point through the red fence along a longitude between  $\mathbf{a}_3$  and  $\mathbf{Q}_2$ . We also used the time reversed loop  $-i$  of the loop  $i$ . We measure the transport of paramagnetic objects on the pattern as a function of the entry longitude that we continuously vary as a function of the azimuthal angle  $\phi_{\text{entry}}$ . The experimentally color coded spheres show the measured splitting location of the ferrofluid droplets and of wax/magnetite doublers, see the legend. The color decodes the different sizes of the split objects according to eqn (3). The same color coding with the droplet areas replaced by the subareas of the theoretical lemniscates is used for the background in the excess region. The unit vector  $\mathbf{n}$  is normal to the pattern. (c) Two unit cells with experimental ferrofluid droplets at a  $\mathbf{Q}$ -splitting line for  $\phi_{\text{entry}} \approx \pi$  (top). Two unit cells of the pattern with theoretical lemniscates (equipotential lines through saddle points), computed from the magnetic potential for an external field in the excess region (middle). Two unit cells with experimental ferrofluid droplets at an  $\mathbf{a}$ -splitting line on the loop  $g$  for  $\phi_{\text{entry}} \approx 7.5\pi/6$  (bottom). The dashed arrows point at the corresponding orientations of the external field in  $\mathcal{C}$ . A video clip clarifying the details of this figure is provided in the ESI† (adfig2.mp4).

A ratchet occurs if the entry and the exit fence segments are of different types. The motion is always adiabatic if the control loop enters and exits the excess region *via* the same type of fence segments, either  $+\mathbf{Q}$ -segments or  $-\mathbf{Q}$ -segments.<sup>17,21</sup> Here, the motion of the steel sphere returns to adiabatic when enclosing the third bifurcation point  $B_{-\mathbf{a}_1}$  (loops f–i  $7\pi/6 < \phi_{\text{entry}} < 9\pi/6$  in Fig. 2b) with a total displacement of the sphere by one unit vector  $-\mathbf{a}_2$ . Since this reorientation loop is adiabatic, the time reversed loop (e.g. the inverse loop  $-h$  with  $4\pi/6 < \phi_{\text{entry}} < 5\pi/6$  and  $7\pi/6 < \phi_{\text{exit}} < 8\pi/6$ ) transports into the opposite, *i.e.* the  $\mathbf{a}_2$  direction compared to the direct loop. We have measured the position of the fence in control space *via* the ratchet jumps of the steel sphere. The blue and red spheres in Fig. 2b are the experimental data of these measurements.

### 3.2 Ferrofluid droplet transport

In Section 3.1, we described the limiting case of one particle being transported. Here, we describe the opposite limit, namely

the transport of a macroscopic ensemble of particles. The particle numbers in between describe the transition from topological towards geometrical and they are discussed in Sections 3.3 and 3.4. To mimic the transport in a system with hundreds of tiny particles per unit cell, we consider the motion of ferrofluid droplets. Hence, the transported object can no longer be considered a point particle. To understand the motion, we need to consider the equipotential lines around the minima of the total magnetic potential that drives the motion. In Fig. 3 we collect images that show the motion of a ferrofluid droplet along some of the control modulation loops displayed in Fig. 2. The loops enclose from zero up to four bifurcation points. At the starting point, the steel sphere and the ferrofluid droplets reside above the central magnet of the unit cell. The sphere/droplet moves away from this location as the external magnetic field enters into the excess region of  $\mathcal{C}$ . Nothing special occurs when the external field crosses the fence, and nothing particular happens to the single steel sphere as the

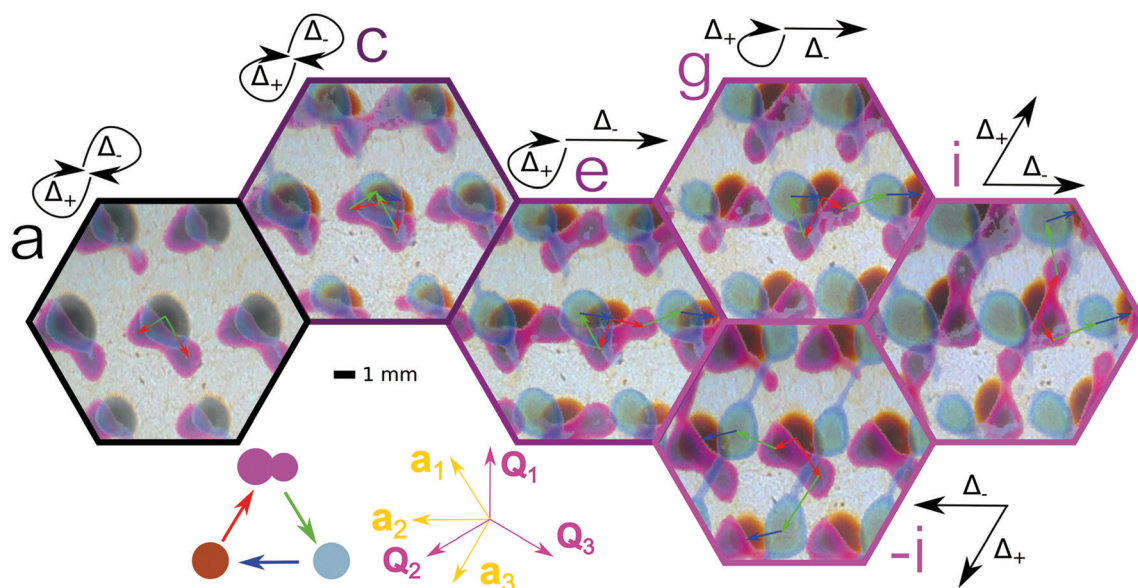


**Fig. 3** Dynamics of the ferrofluid droplets subject to the modulation loops a-i, and -i of Fig. 2. In each image we overlay an image of the droplet before the entry into the excess region (brown), at the splitting line (purple) and after recombination at the end of the loop (turquoise). The different images correspond to different loops depicted in Fig. 2b with loop a  $\phi_{\text{entry}} = \phi_{\text{exit}} = 4.4\pi/6$ , loop c  $\phi_{\text{entry}} = 5.5\pi/6$ ,  $\phi_{\text{exit}} = 4.4\pi/6$ , loop e  $\phi_{\text{entry}} = 6.5\pi/6$ ,  $\phi_{\text{exit}} = 4.4\pi/6$ , loop g  $\phi_{\text{entry}} = 7.5\pi/6$ ,  $\phi_{\text{exit}} = 4.4\pi/6$  loop i  $\phi_{\text{entry}} = 8.5\pi/6$ ,  $\phi_{\text{exit}} = 4.4\pi/6$  and the inverse loop -i  $\phi_{\text{entry}} = 4.4\pi/6$ ,  $\phi_{\text{exit}} = 8.5\pi/6$ . For loops a and c, two trivial modes coexist. In loops e and g, a transport mode into the  $-\mathbf{a}_2$  direction coexists with a trivial mode. In loop i, a transport mode in the  $-\mathbf{a}_2$  direction coexists with a transport mode into the  $-\mathbf{a}_3$  direction. The control loop of -i is the inverse of loop i with two transport modes along  $\mathbf{a}_2$  and  $\mathbf{a}_3$ . The red arrows show the transport directions during the splitting of the brown droplet towards the purple droplets. The green arrows show the motion of the two purple droplets as they rejoin into the turquoise droplet. The blue arrow shows the adiabatic motion upon closing the loop in control space by returning to the starting point. The displacement after one control loop is the coexistence of the two displacements  $\Delta_+$  and  $\Delta_-$  of the two split droplets. The black arrows are sketches of the motion of the droplets. The scale bar is 1 mm. A video clip showing the motion of the droplets is provided in the ESI† (adfig3.mp4).

field moves deeper into the excess region. The ferrofluid droplet, however, deforms into a dogbone-like shape and eventually splits into two smaller droplets when the modulation loop crosses a droplet splitting line in  $C$ . Some of the shapes of such droplets are shown in Fig. 2c. Their shape and size agree very well with the shape and size of the lemniscates, which are simply the equipotential lines of the colloidal potential passing through the saddle point between both minima (see Fig. 2c). The two separated ferrofluid droplets reside in a region above the two different minima, where the potential is in the excess region of  $C$ . The droplets are in general transported into different directions. When the modulation loop is closed (returns to the starting point), the two split ferrofluid droplets must return to either the original position above the same central silver magnet or to an equivalent position in a different unit cell. The transport over one period is therefore the coexistence of two different types of transport directions. The total transport is the sum of the two coexisting displacements, weighted with the two areas of the droplets when they split.

The splitting of a ferrofluid droplet occurs either in an adiabatic way (a-splitting) or irreversibly (Q-splitting). Both types of splitting are schematically represented in Fig. 4. The ferrofluid droplet covers a certain area  $A$  of action space when the external field enters the excess region of  $C$ . A “minor” excess minimum and an excess saddle point are created in the magnetic potential upon the entry of the external field into the excess region.<sup>17</sup>

The equi-potential line passing through the excess saddle point is a lemniscate that first winds around the preexisting “major” minimum, then passes through the saddle point, and next winds around the minor excess minimum. Hence, the lemniscate defines a closed curve of area  $L = L_+ + L_-$  where each of the two sub areas,  $L_+$  and  $L_-$ , surrounds a minimum of the potential. At the fence in  $C$ , the sub lemniscate area of the minor minimum,  $L_+ = 0$  ( $L_- = 0$ ) for a  $-\mathbf{Q}$ -fence segment ( $+\mathbf{Q}$ -fence segment) vanishes. At the fence  $L_+ = 0$  or  $L_- = 0$  and the area occupied by the ferrofluid droplet can be either larger  $A > L_+ + L_-$  or smaller  $A < L_-$  ( $A < L_+$ ) than that of the preexisting major minimum.

In the case  $A > L_+ + L_-$  (a-splitting), which occurs if the loop enters the excess region of  $C$  close to a  $B_a$  bifurcation point, the ferrofluid droplet assumes the shape of an equipotential line containing both minima (see Fig. 2c bottom and Fig. 4a). When the loop enters deeper into the excess region of  $C$ , the area of the lemniscate grows (Fig. 4(a1) and (a2)). At the point where the area of the lemniscate is the same as the area of the droplet,  $L = L^a = A$ , both lemniscate subareas  $L_+^a$  and  $L_-^a$  are fully filled with a ferrofluid (Fig. 4(a3)). When the area of the lemniscate grows beyond that of the droplet,  $L > A$ , then the droplet splits into two droplets of areas  $A_+ = L_+^a$  and  $A_- = L_-^a$  (Fig. 4(a4)). The areas of both droplets do not change until the droplets coalesce again, *i.e.* no further splitting occurs. The splitting is reversible if the control loop is reversed and crosses the splitting line  $L^a = A$  at exactly the same point.

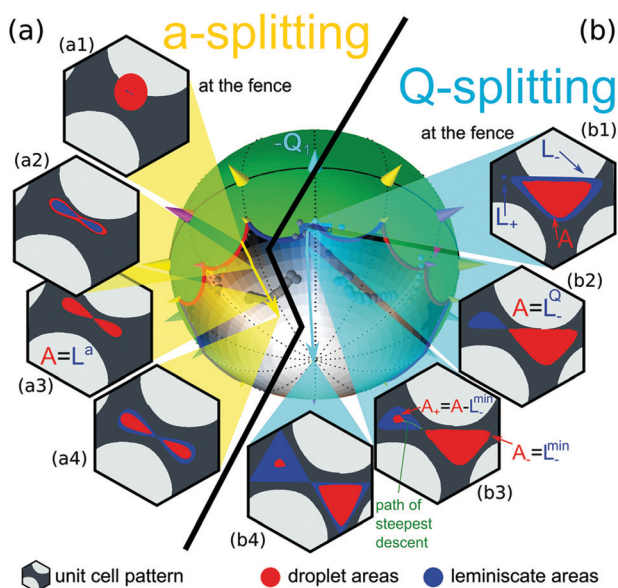


Fig. 4 Schematics of the **a**-splitting (a) and the **Q**-splitting (b) of a ferrofluid droplet. In each case a unit cell (hexagon) with the droplets (red) and the lemniscates (blue) is represented for four different orientations of the external field along a control loop that enters the excess regions of  $\mathcal{C}$  near a  $\mathcal{B}_a$ -bifurcation point (a1)–(a4) and a  $\mathcal{B}_{-Q}$ -bifurcation point (b1)–(b4). The loop segments of both loops in control space are indicated in the control space in the center of the image. The positions of the large (small) magnets in the unit cell are shown in light (dark) gray.

In Fig. 2b we have color coded the splitting ferrofluid droplets with a normalized RGB-color given by the triplet

$$(\mathbf{R}, \mathbf{G}, \mathbf{B}) = \frac{8}{A_{\text{UC}}}(A_+, (A_+ + A_-)/2, A_-), \quad (3)$$

where  $A_{\text{UC}}$  is the area of the unit cell, and the factor eight accounts for the fact that the maximum subarea of a lemniscate is one eighth of the area of the unit cell (see Fig. 4(b4)). We have also color coded the excess region of  $\mathcal{C}$  in Fig. 2b with the same criterion but replacing the subareas  $A_{\pm}$  with the subareas of the lemniscates  $L_{\pm}$ . Hence, the color of the experimental data points at the splitting lines in Fig. 2b matches the color of the control space only if  $A_{\pm} = L_{\pm}$ , *i.e.*, if the subareas of the theoretical lemniscates and those of the droplets are equal. In Fig. 2b, the color of the experimental **a**-splitting points is darker than the background, indicating that the experimental droplets split later than predicted by the theory. This is presumably because adhesive forces of the droplet prevent early splitting. The color discrepancy of the data below the  $\mathcal{B}_{-a_1}$  bifurcation points is likely due to scattering in the magnetization of the NbB magnets forming the pattern. The finite size of the pattern and the elevation of the particles above the pattern also have an effect on the experimental measurements.

In the case  $A < L_-$  (**−Q**-splitting), which occurs if the control loop enters the excess region close to a  $\mathcal{B}_{-Q}$  bifurcation point, the ferrofluid droplet assumes the shape of an equi-potential line surrounding only the preexisting major minimum but not the excess minor minimum. We show in Fig. 2c top the picture of a droplet just after a **−Q**-splitting (see also Fig. 4b). The largest

areas of  $L_-$  occur if the external field points at the south pole and at the  $\mathcal{B}_{-Q}$  bifurcation points of  $\mathcal{C}$ . Hence, a locally minimal area  $L_-^{\text{min}}$  occurs for external fields pointing along a longitude that connects the south pole and one of the  $\mathcal{B}_{-Q}$  bifurcation points. The subarea  $L_-$  of the preexisting minimum of the lemniscate shrinks as the control loop moves from the fence towards the south pole (Fig. 4(b1)). At some point, the subarea of the lemniscate  $L_-$  equals that of the droplet  $L_-^Q = A$  (provided that  $L_-^{\text{min}} < A < L_-$ ), Fig. 4(b2). There, the fluid completely fills the subarea  $L_-^Q$  while the other subarea  $L_+$  is completely empty. When the major area of the lemniscate shrinks below the droplet area, *i.e.*  $L_- < A$ , then the droplets split into two droplets of areas  $A_- = L_-$  and  $A_+ = A - L_-$  (Fig. 4(b3)). The fluid in  $L_-$  is expelled from the droplet through the saddle point and flows down the path of the steepest descent into the basin of the minor excess minimum. The areas of the droplet change until the decrease of  $L_-$  stops, Fig. 4(b4). The splitting process is irreversible and both droplets cannot be rejoined in a reversible way since the fluid in the excess minimum cannot flow up the path of the steepest descent back into the preexisting minimum.

We have placed  $\pm\mathbf{Q}$ -splitting experimental points at the location where the splitting starts. The points are colored according to eqn (3) with  $A_{\pm}$  being the subareas when the interchange of fluid between  $A_+$  and  $A_-$  stops. The agreement with the theoretical prediction given by the areas of the lemniscate (colored background) is excellent.

The splitting lines  $L^a = A$ ,  $L_-^Q = A$  and  $L_+^Q = A$  are the segments of a closed curve that are joined at the fence of  $\mathcal{C}$ . For  $A > L_-^{\text{min}}$ , any closed curve of a modulation loop in  $\mathcal{C}$  that penetrates the excess region deep enough must also pass the splitting curve. A nontrivial modulation therefore causes nontrivial transport that is the coexistence of two topological displacements weighted with the two split areas of the droplet. The splitting areas  $A_-$  and  $A_+$  continuously change along the splitting lines. A video clip (adfig3.mp4) showing more details of the ferrofluid transport is provided in the ESI.†

### 3.3 Doublet transport

We have experimentally studied the transport of two particles per unit cell. The area  $A$  enclosed by the two wax/magnetite spheres is smaller than the local minimum area, *i.e.*  $A < L_-^{\text{min}}$ . Hence, in contrast to the ferrofluid droplet, the **Q**-splitting cannot occur for these doublets. Both the ferrofluid droplet and the doublet exhibit **a**-splitting. A measurement of the **a**-splitting line  $L^a = A$  is shown for the wax/magnetite doublets in Fig. 2b. The doublets are transported together within the major minimum if the control loop enters the excess region in the vicinity of the  $\mathcal{B}_{\pm Q}$  bifurcation point. If the loop enters the excess region in the vicinity of the  $\mathcal{B}_a$  bifurcation point, then **a**-splitting occurs and both spheres are separated. One sphere is transported within the major minimum and the other one within the minor minimum. Two transport directions coexist.

Hence, depending on  $\phi_{\text{entry}}$  there are two different transport modes for the doublets: (i) no splitting and (ii) **a**-splitting. The

transition from one transport mode towards the other transport mode occurs at the doublet bifurcation points  $\mathcal{B}_{\text{doublet}}$  that are the intersections of the fence with the  $\mathbf{a}$ -splitting line  $L^a = A$  for doublets. Since the spheres have the same size, the areas of the  $\mathbf{a}$ -splitting transport are equal  $A_- = A_+ = A/2$ . Hence, the experimental data points for doublet  $\mathbf{a}$ -splitting all have the same color, see eqn (3) and Fig. 2b. The color is darker than the theoretical background color of the lemniscates. Hence, splitting occurs later in the experiment than predicted by the theory, presumably due to the dipolar attraction between the two spheres as well as due to friction with the bottom surface. Like the transport of a single sphere, the transport of doublets is discrete and therefore topological.

**Net displacement.** We next analyze the net displacement after the completion of one entire control loop for all three types of objects: single spheres, doublets, and ferrofluid droplets. For all objects, we define the vector of the net displacement

$\Delta$  as the area averaged sum of the two possible displacements. That is

$$\Delta = \frac{\Delta_+ A_+ + \Delta_- A_-}{A_+ + A_-}, \quad (4)$$

where  $\Delta_{\pm}$  are the net displacement vectors of the two minima in one control loop. Hence,  $\Delta_{\pm}$  are always lattice vectors and  $\Delta$  moves along a straight line between the two lattice vectors.

In Fig. 5a, we plot the net displacement of all magnetic objects as a function of  $\phi_{\text{entry}}$  for a family of loops with  $\phi_{\text{exit}} = 4.4\pi/6$  (loops similar to those in Fig. 2b). A video of the motion is presented in the ESI† (adfig5.mp4). The net displacement is zero when the loop encloses no bifurcation point. The displacement moves along the straight lines connecting the sequence of lattice vectors  $\mathbf{0}, -\mathbf{a}_2, -\mathbf{a}_3, \mathbf{a}_1$ , and  $\mathbf{0}$  (see the gray arrows in the center of Fig. 5a). The areas  $A_+$  and  $A_-$  are continuous functions of  $\phi_{\text{entry}}$  for the ferrofluid droplet. In contrast, the transported

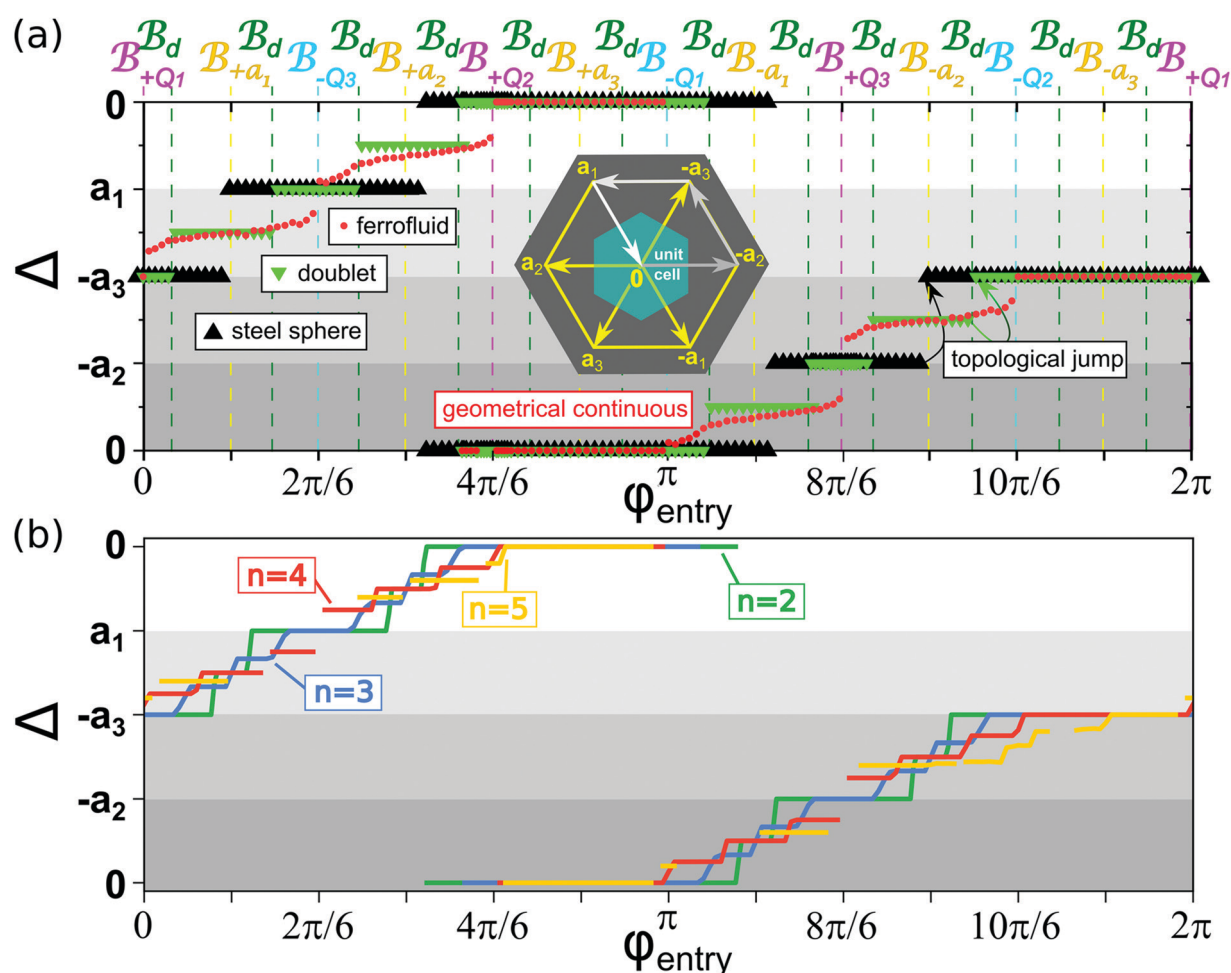


Fig. 5 Experimental and simulated displacements for the set of modulation loops characterized by  $\phi_{\text{entry}}$ . (a) Experimental measurements of the net displacement  $\Delta$  of the steel sphere, the wax/magnetite doublet, and the ferrofluid droplets as a function of  $\phi_{\text{entry}}$  for a family of loops with  $\phi_{\text{exit}} = 4.4\pi/6$ . The displacement changes correspond to the four gray arrows shown in the center of the image. The four gray shaded regions correspond to the arrows of the same color in the inset. The displacement is a discrete function of  $\phi_{\text{entry}}$  for the steel sphere and the wax/magnetite spheres but a continuous function for the ferrofluid droplets. The jumps in the displacement occur when the loop crosses the bifurcation points in control space (the position of the bifurcation points is indicated with vertical dashed lines). A video of the motion of a steel sphere, a wax magnetite doublet, and ferrofluid droplets subjected to two different control loops is shown in the ESI† adfig5.mp4. (b) Net displacement of a collection of  $n = 2, 3, 4$ , and  $5$  particles, as indicated, for the same family of control loops as in panel (a) according to computer simulations.

areas  $A_{\pm}$  for one steel sphere (a wax/magnetite doublet) can only be integer multiples  $n = 0, 1$  ( $n = 0, 1, 2$ ) of the area of one sphere. Contrary to the ferrofluid transport, the sphere and doublet net displacement change discretely with  $\phi_{\text{entry}}$ . The number of discrete steps for the doublets is twice that of a single steel sphere. Hence, the transport of one or two spheres is topological while the transport of the ferrofluid is geometrical.

### 3.4 Multiparticle transport

What is the minimum number of particles required for having geometrical transport? To address this fundamental question, we have simulated the transport of multiple spheres using overdamped Langevin dynamics (note that inertial effects are negligible). Each unit cell is filled with exactly  $n$  particles. Each particle is subject to the magnetic potential

$$U(\mathbf{x}_A, \mathbf{H}_{\text{ext}}(t)) \propto -\mathbf{H}_{\text{ext}}(t) \cdot \mathbf{H}_p(\mathbf{x}_A), \quad (5)$$

where  $\mathbf{H}_{\text{ext}}(t)$  is the external field at time  $t$  and  $\mathbf{H}_p(\mathbf{x}_A)$  is the magnetic field, created by the pattern at the position of the particle  $\mathbf{x}_A$  in action space  $\mathcal{A}$ , see ref. 22 and 23.

The particles interact *via* the purely repulsive Weeks–Chandler–Andersen potential

$$\phi(r) = \begin{cases} 4\varepsilon \left( \left( \frac{\sigma}{r} \right)^{12} - \left( \frac{\sigma}{r} \right)^6 + \frac{1}{4} \right) & r \leq 2^{1/6}\sigma \\ 0 & r > 2^{1/6}\sigma \end{cases}, \quad (6)$$

where  $r$  is the distance between the particles,  $\varepsilon$  fixes our unit and energy, and  $\sigma$  is the effective particle length that we fix to  $\sigma/a = 0.2$  which is the same as in the experiments (transport of single spheres). We integrate the equations of motion with a time step  $dt/T = 10^{-5}$ , with  $T$  being the period of a modulation loop. As the transport is topological the detailed features of the simulated particles are of minor importance and the behavior will not change using somewhat different parameters for the simulations. Fig. 5b shows the net displacement of  $n = 2, 3, 4, 5$  spheres. The number of plateaus in the displacement of  $n$  particles per unit cell is  $n$  times the number of plateaus of a single sphere. This is true provided that each unit cell is filled with precisely  $n$  particles since the results depend on the initial distribution of particles among the different unit cells. Our simulation results suggest therefore that if precisely the same number of equally sized ferrofluid particles could be deposited in each droplet, one would still observe topological transport, albeit with very fine splitting. However, if there is dispersion in the size of particles, the occupation of the unit cells, the number of plateaus and splittings might be significantly increased because the number of different geometrically distinguishable ways to split the droplets into subdroplets is increased. For broad dispersions of sizes we would expect that the transport is topological with a step size that scales with an other power than the inverse of the occupation of the site. Here, we have investigated only the case of monodisperse particles.

Note that the experimental  $\phi_{\text{entry}}$  and the  $\phi_{\text{entry}}$  in the simulations of the doublet bifurcation points (at which the net displacement jumps) differ (Fig. 5a and b). In the experiment, the

spheres do not only interact *via* excluded volume interactions, but are also subject to long range dipolar interactions. We tried to minimize the effect of dipolar interactions by using the wax/magnetite composite spheres. We have understood the transport properties under simple conditions, however an in depth understanding must also include studies of how the transport changes with polydisperse particle sizes, varying the occupation of unit cells, and with stronger dipolar interactions.

## 4 Conclusions

We have studied experimentally and with computer simulations the transport of paramagnetic particles on top of a magnetic lattice, driven by a uniform and time-dependent external magnetic field. The external field performs periodic closed loops. We have shown that increasing the number of particles within the unit cell of the lattice changes the transport from topological towards geometrical.

The transport as a function of a parameter that continuously characterizes a family of control loops is discrete for low particle densities and continuous for a macroscopic number of particles per unit cell (ferrofluid droplet). More possibilities to split or disjoin soft matter assemblies increase the number of bifurcation points in control space with more transport modes in action space that are separated by finer steps. It is the number of possibilities that eventually changes the transport from topological to geometrical.

A ferrofluid is a colloidal suspension of nanoparticles. Rendering the transport of this soft matter system as robust as the solid particle transport, the magnetic pattern must be downscaled to the nanometer range. In such downscaling studies, we have already shown the topological nature of the transport of a colloidal dispersion of micron-sized magnetic colloids.<sup>17,22</sup>

## Conflicts of interest

There are no conflicts to declare.

## Appendix

Here we provide some details of the experimental setup. The magnetic hexagonal lattice (Fig. 1a) consists of large (l) and small (s) cylindrical magnets of height  $h = 2$  mm, diameters  $d_l = 3$  mm and  $d_s = 2$  mm, and remanences  $\mu_0 M_l = 1.19$  T and  $\mu_0 M_s = 1.35$  T, with  $\mu_0$  being the permeability of free space. The resulting lattice with two primitive lattice vectors of length  $a = 4.33$  mm is mechanically metastable in zero external magnetic field. Therefore, we need to fix the metastable arrangement with an epoxy resin placed in the voids and in the two dimensional surroundings of the pattern. The pattern is then stable also in the presence of an external field. The pattern is put on a support and covered with a transparent PMMA spacer of thickness  $z = 1$ – $1.5$  mm (Fig. 1c). It may be sprayed with PTFE to suppress wetting with the ferrofluid

droplets. Additionally, a white illuminated foil can be placed underneath the PMMA.

We either place one steel sphere of diameter  $2r = 1$  mm or two spheres of diameter  $2r = 0.5$  mm consisting of a 10:1 weight percent mixture of wax and magnetite on top of the spacer. Alternatively, we place two fluids, a nonmagnetic fluid (Galden) and an aqueous ferrofluid immiscible with the Galden at a volume ratio Galden/ferrofluid of 152:1, on top of the PTFE and close to the compartment with a transparent lid.

The goniometer is set up at an angle of 45 degrees to ensure that the relevant motion is not affected by the restrictions of motion of the goniometer caused by the support. The two large NbB-magnets that generate the external field have a diameter  $d_{\text{ext}} = 60$  mm, a thickness  $t_{\text{ext}} = 10$  mm, and a remanence of  $\mu_0 M_{\text{ext}} = 1.28$  T and they are separated by a distance  $2R = 120$  mm.

## Acknowledgements

Scientific discussion with Michel Lönne is highly appreciated.

## References

- 1 S.-Q. Shen, *Topological insulators: Dirac equation in condensed matters*, Springer Science, and Business Media, 2013.
- 2 J. Anandan, J. Christian and K. Wanelik, Resource Letter GPP-1: Geometric Phases in Physics, *Am. J. Phys.*, 1997, **65**, 180–185.
- 3 M. V. Berry, Quantum phase factors accompanying adiabatic changes, *Proc. R. Soc. London, Ser. A*, 1984, **A392**, 45–57.
- 4 J. H. Hannay, Angle variable holonomy in adiabatic excursion of an integrable Hamiltonian, *J. Phys.*, 1985, **A18**, 221–230.
- 5 A. Shapere and F. Wilczek, Geometry of self-propulsion at low Reynolds number, *J. Fluid Mech.*, 1989, **198**, 557–585.
- 6 A. Shapere and F. Wilczek, Efficiency of self-propulsion at low Reynolds number, *J. Fluid Mech.*, 1989, **198**, 587–599.
- 7 M. Z. Hasan and C. L. Kane, Colloquium: Topological insulators, *Rev. Mod. Phys.*, 2010, **82**, 3045–3067.
- 8 D. Harland and N. S. Manton, Rolling Skyrmions and the nuclear spin-orbit force, *Nucl. Phys. B*, 2018, **935**, 210–241.
- 9 K. v. Klitzing, G. Dorda and M. Pepper, New method for high-accuracy determination of the fine-structure constant based on quantized Hall resistance, *Phys. Rev. Lett.*, 1980, **45**, 494–497.
- 10 M. C. Rechtsman, J. M. Zeuner, Y. Plotnik, Y. Lumer, D. Podolsky, F. Dreisow, S. Nolte, M. Segev and A. Szameit, Photonic Floquet topological insulators, *Nature*, 2013, **496**, 196–200.
- 11 M. Xiao, G. Ma, Z. Yang, P. Sheng, Z. Q. Zhang and C. T. Chan, Geometric phase and band inversion in periodic acoustic systems, *Nat. Phys.*, 2015, **11**, 240–244.
- 12 J. Paulose, B. G. Chen and V. Vitelli, Topological modes bound to dislocations in mechanical metamaterials, *Nat. Phys.*, 2015, **11**, 153–156.
- 13 C. L. Kane and T. C. Lubensky, Topological boundary modes in isostatic lattices, *Nat. Phys.*, 2014, **10**, 39–45.
- 14 L. M. Nash, D. Kleckner, A. Read, V. Vitelli, A. M. Turner and W. T. M. Irvine, Topological mechanics of gyroscopic metamaterials, *Proc. Natl. Acad. Sci. U. S. A.*, 2015, **112**, 14495–14500.
- 15 S. D. Huber, Topological mechanics, *Nat. Phys.*, 2016, **12**, 621–623.
- 16 A. Murugan and S. Vaikuntanathan, Topologically protected modes in non-equilibrium stochastic systems, *Nat. Commun.*, 2017, **8**, 13881.
- 17 J. Loehr, M. Loenne, A. Ernst, D. de las Heras and T. M. Fischer, Topological protection of multiparticle dissipative transport, *Nat. Commun.*, 2016, **7**, 11745.
- 18 Y. Xiong, Why does bulk boundary correspondence fail in some non-hermitian topological models, *J. Phys. Commun.*, 2018, **2**, 035043.
- 19 S. Yao and Z. Wang, Edge States and Topological Invariants of Non-Hermitian Systems, *Phys. Rev. Lett.*, 2018, **121**, 086803.
- 20 F. K. Kunst, E. Edvardsson, J. C. Budich and E. J. Bergholtz, Biorthogonal bulk-boundary correspondence in non-Hermitian systems, *Phys. Rev. Lett.*, 2018, **121**, 026808.
- 21 A. M. E. B. Rossi, J. Bugase and T. M. Fischer, Macroscopic Floquet topological crystalline steel and superconductor pump, *Europhys. Lett.*, 2017, **119**, 40001.
- 22 J. Loehr, D. de las Heras, M. Loenne, J. Bugase, A. Jarosz, M. Urbaniak, F. Stobiecki, A. Tomita, R. Huhnstock, I. Koch, A. Ehresmann, D. Holzinger and T. M. Fischer, Lattice symmetries and the topologically protected transport of colloidal particles, *Soft Matter*, 2017, **13**, 5044–5075.
- 23 D. de las Heras, J. Loehr, M. Loenne and T. M. Fischer, Topologically protected colloidal transport above a square magnetic lattice, *New J. Phys.*, 2016, **18**, 105009.
- 24 D. P. Jackson, R. E. Goldstein and A. O. Cebers, Hydrodynamics of fingering instabilities in dipolar fluids, *Phys. Rev. E: Stat. Phys., Plasmas, Fluids, Relat. Interdiscip. Top.*, 1994, **50**, 298.
- 25 N. Wilke, J. Bugase, L.-M. Treffenstädt and T. M. Fischer, Wrinkled labyrinths in critical demixing ferrofluid, *Soft Matter*, 2017, **13**, 7307–7311.



# Publication 3

---

## Simultaneous polydirectional transport of colloidal bipeds

*Nature Communications* **11**, 4670 (2020)

Mahla Mirzaee-Kakhki,<sup>a1</sup> **Adrian Ernst**,<sup>a1</sup>  
Daniel de las Heras,<sup>a2</sup> Maciej Urbaniak,<sup>b</sup>  
Feliks Stobiecki,<sup>b</sup> Jendrik Gördes,<sup>c</sup> Meike Reginka,<sup>c</sup>  
Arno Ehresmann,<sup>c</sup> & Thomas M. Fischer<sup>a1</sup>

<sup>a1</sup> Experimental Physics X and <sup>a2</sup> Theoretical Physics II, Department of Physics, University of Bayreuth, 95447 Bayreuth, Germany.

<sup>b</sup> Institute of Molecular Physics, Polish Academy of Sciences, 60-179 Poznań, Poland.

<sup>c</sup> Institute of Physics and Center for Interdisciplinary Nanostructure Science and Technology (CINSaT), University of Kassel, 34132 Kassel, Germany.

---

### My Contribution

Mahla Mirzaee-Kakhki discovered the topological nature of the biped transport and performed the experiments. I had the idea to use polyglot commands and wrote a computer program inverting the loop transport problem for finding compact and robust loops for the various tasks shown in the paper. Daniel de las Heras supervised the simulations and Thomas Fischer the experiments. The authors from Poznań grew the magnetic films and the authors from Kassel Helium bombarded them to create the magnetic patterns. The preparation and writing of the paper was done by all authors.



# Simultaneous polydirectional transport of colloidal bipeds

Mahla Mirzaee-Kakhki<sup>1</sup>, Adrian Ernst <sup>1</sup>, Daniel de las Heras <sup>2</sup>, Maciej Urbaniak <sup>3</sup>, Feliks Stobiecki <sup>3</sup>, Jendrik Gördes <sup>4</sup>, Meike Reginka <sup>4</sup>, Arno Ehresmann <sup>4</sup> & Thomas M. Fischer <sup>1</sup>✉

Detailed control over the motion of colloidal particles is relevant in many applications in colloidal science such as lab-on-a-chip devices. Here, we use an external magnetic field to assemble paramagnetic colloidal spheres into colloidal rods of several lengths. The rods reside above a square magnetic pattern and are transported via modulation of the direction of the external magnetic field. The rods behave like bipeds walking above the pattern. Depending on their length, the bipeds perform topologically distinct classes of protected walks. We design parallel polydirectional modulation loops of the external field that command up to six classes of bipeds to walk on distinct predesigned paths. Using such loops, we induce the collision of reactant bipeds, their polymerization addition reaction to larger bipeds, the separation of product bipeds from the educts, the sorting of different product bipeds, and also the parallel writing of a word consisting of several letters. Our ideas and methodology might be transferred to other systems for which topological protection is at work.

<sup>1</sup>Experimentalphysik X, Physikalisches Institut, Universität Bayreuth, D-95440 Bayreuth, Germany. <sup>2</sup>Theoretische Physik II, Physikalisches Institut, Universität Bayreuth, D-95440 Bayreuth, Germany. <sup>3</sup>Institute of Molecular Physics, Polish Academy of Sciences, 60-179 Poznań, Poland. <sup>4</sup>Institute of Physics and Center for Interdisciplinary Nanostructure Science and Technology (CINSaT), Universität Kassel, D-34132 Kassel, Germany. ✉email: [Thomas.Fischer@uni-bayreuth.de](mailto:Thomas.Fischer@uni-bayreuth.de)

A time-dependent energy landscape can transport objects with different properties into different directions. This is the basic idea behind any sorting process, including sieving. On a microscopic level, an optical lattice can be used to sort particles based on the strength of the interaction between the particles and the lattice sites<sup>1</sup>. Ratchets<sup>2</sup> can also be used for the directed transport of distinct microscopic objects<sup>3</sup>. Simultaneous sorting of heterogeneous materials can be achieved with particles driven through periodically modulated energy landscapes<sup>4</sup>. In general, these mechanisms do not allow to precisely control the direction of the transported objects.

The simultaneous transport of colloidal assemblies that can be adapted to requirements such as the presence or absence of colloidal cargo would allow to switch between multiple tasks on lab-on-the-chip devices. To this end, depending on their intrinsic properties, colloidal assemblies need to respond differently to an externally given command. The analog in computer science is known as a polyglot, a program that can be simultaneously compiled and executed in different languages. Typically, the polyglot performs the same task in all valid languages. However, much more powerful polyglots can be coded to perform different and independent tasks for each language<sup>5</sup>. A current of electrons is the only computational element in computer science. The ability to execute commands in parallel gains relevance if several computational elements are used. For example, in biochemistry the nodes of a metabolic network trigger different reactions in parallel. Other areas that would benefit from using parallel commands include the parallel computing with entangled quantum states<sup>6–8</sup>, with DNA oligonucleotides<sup>9–14</sup>, and with soft matter devices<sup>15</sup> such as membranes<sup>16</sup>, reaction-diffusion computers<sup>17</sup>, microfluidic computers<sup>18,19</sup> and colloidal computers<sup>20,21</sup>.

Here we develop a parallel polydirectional command for the robust transport of colloidal rods above magnetic patterns. The parallel polydirectional command addresses simultaneously and independently the transport of rods of different lengths, and it is hence more efficient than multiplexing, which addresses one command at a time. We provide a fully explained parallel polydirectional command ultimately based on topological protection.

## Results

**Experimental setup.** Paramagnetic colloidal particles (diameter 2.8 μm) immersed in water are placed on top of a two-dimensional magnetic pattern. The pattern is a square lattice of alternating regions with positive and negative magnetization relative to the direction normal to the pattern, see Fig. 1a. A uniform time-dependent external field of constant magnitude is superimposed to the nonuniform time-independent magnetic field generated by the pattern. The external field induces strong dipolar interactions between the colloidal particles which respond by self-assembling into rods of 2–19 particles.

The orientation of the external field changes adiabatically along a closed loop (Fig. 1b). Despite the field returning to its initial direction, single colloidal particles can be topologically transported by one-unit cell after completion of one loop<sup>22,23</sup>. The transport occurs provided that the loop winds around specific orientations of the external field. In particular, around those orientations given by the unit vectors of the square magnetization pattern<sup>23</sup>. Colloidal rods formed by several particles can also be transported. The rod aligns with the external field since dipolar interactions are stronger than the buoyancy. Hence, if the external field is not parallel to the pattern, one end of the rod remains on the ground while the other one is lifted. As a result, the rods walk through the pattern, see Brownian dynamics

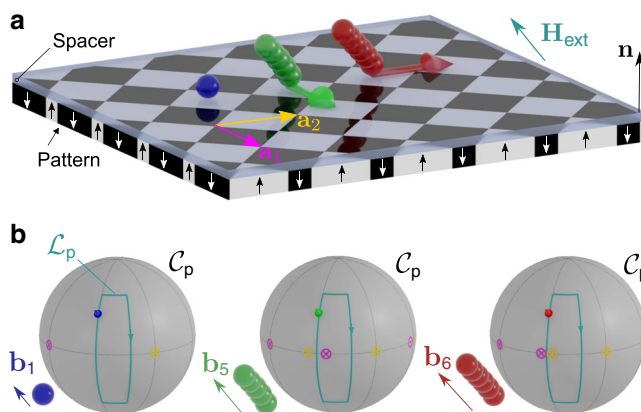


**Fig. 1 Schematic of the colloidal transport.** **a** A square magnetic pattern with lattice vectors  $\mathbf{a}_1$  and  $\mathbf{a}_2$  is magnetized with regions of positive (white) and negative (black) magnetization parallel to the vector normal to the pattern  $\mathbf{n}$ . Spherical colloidal particles (blue) are placed on top of the pattern immersed in water. Due to the presence of a strong homogeneous external field, some colloids self-assemble into rods of different length (green and red). **b** Our control space  $C_p$  is a sphere that represents all possible directions of the external field  $\mathbf{H}_{\text{ext}}$ . The direction of the external field varies in time performing a closed loop  $\mathcal{L}_p$ . The colored arrow tip on the loop corresponds to the orientation of the external field depicted in **a**. The orientation of the bipeds ( $\mathbf{b}_1$ ,  $\mathbf{b}_5$ , and  $\mathbf{b}_6$ ) is parallel to  $\mathbf{H}_{\text{ext}}$ . If the loop winds around special directions (yellow and pink equatorial circles), colloidal rods move as bipeds one-unit cell after completion of one loop (**a**). The topological properties of control space depend on the length of the rod, allowing the design of parallel polydirectional loops that move rods of different lengths simultaneously along different directions. Here, the loop transports  $b_5$ -bipeds with five colloidal particles by  $\Delta\mathbf{r}(\mathcal{L}_5) = \mathbf{a}_1$  (green arrow in **a**),  $b_6$ -bipeds with six colloidal particles by  $\Delta\mathbf{r}(\mathcal{L}_6) = \mathbf{a}_2$  (red arrow in **a**), and does not transport single colloids  $b_1$ .

simulations in Supplementary Movie 1. For this reason, we refer to the rods as bipeds<sup>24–28</sup>.

**Parallel polydirectional loops.** To transport the bipeds, the loop also needs to wind around special orientations of the external field. Surprisingly, these special orientations depend on the length of the bipeds, see Fig. 1b. Bipeds of different length fall into different topological classes such that their displacement upon completion of one parallel polydirectional loop can be different in both magnitude and direction. A sketch of the process is shown in Fig. 1. As it is the case for single colloids, the biped motion is topologically protected and hence robust against perturbations. As we show next, it is possible to design parallel polydirectional loops that simultaneously and independently transport bipeds of different lengths.

For example, parallel didirectional loops can be used to simultaneously transport bidisperse bipeds into two different directions. Fig. 2a shows the experimental trajectories of a set of bipeds of lengths  $b_5$  and  $b_6$ , with  $b_n = nD$  and  $D$  the diameter of the colloidal particles.

Parallel tridirectional loops can be used to initiate the polymerization addition reaction of two bipeds of different lengths by setting them on a collision course and letting the product of the polymerization be transported into a third direction. In Fig. 2b we show experimental trajectories of biped educts of lengths  $b_3$  and  $b_7$  polymerizing to a product biped of length  $b_{10}$ .

In Fig. 2c, bipeds of lengths  $b_3$ ,  $b_7$ ,  $b_2$ ,  $b_5$ , and  $b_{10}$  are driven by a complex parallel tetradirectional loop that simultaneously programs the bipeds to write the letters T, E, T, R, and A,

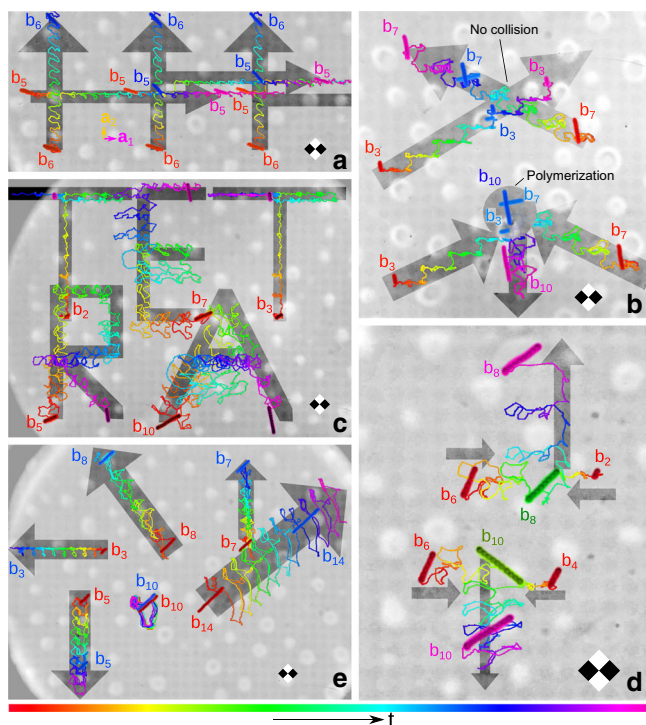


**Fig. 2 Experimental trajectories of bipeds driven by parallel polydirectional loops.** **a** parallel didirectional loop of robustness  $\rho = 0.16$  and compaction  $c = 1/2$  transporting several bipeds  $b_5$  into the  $\mathbf{a}_1$ -direction and bipeds  $b_6$  into the  $\mathbf{a}_2$ -direction. **b** parallel tridirectional loop of robustness  $\rho = 0.3$  and compaction  $c = 7/8$  setting two bipeds  $b_3$  and two bipeds  $b_7$  on a collision course. One pair of bipeds collides and polymerizes to a longer biped  $b_{10}$  that is then transported into a third direction. The non-colliding bipeds continue their motion. **c** Parallel tetradirectional loop of robustness  $\rho = 0.2$  and compaction  $c = 30/54$  commanding bipeds of five different lengths  $\{b_3, b_7, b_2, b_5, b_{10}\}$  to simultaneously write four different letters. The biped  $b_2$  is topologically equivalent to the biped  $b_3$  and hence writes the same letter (T). **d** Parallel pentadirectional loop of robustness  $\rho = 0.11$  and compaction  $c = 5/6$  commanding a biped  $b_2$  and a biped  $b_4$  to polymerize with two colliding bipeds  $b_6$  and then separate as they form a biped  $b_8$  and a biped  $b_{10}$ . **e** Parallel hexadirectional loop of robustness  $\rho = 0.06$  and compaction  $c = 4/8$  transporting six bipeds of different lengths into six different directions. The color of both bipeds and trajectories indicates the time progress of one control loop (see bottom colorbar). A square region of the pattern of diagonal  $2a \approx 22 \mu\text{m}$  is sketched in each panel to indicate the scale and the relative orientation.

respectively. Note that bipeds of lengths  $b_2$  and  $b_3$  perform the same trajectory (letter T). As we show below the reason is that  $b_2 < b_3 < a$  with  $a \approx 11 \mu\text{m}$  the lattice constant of the pattern. Both  $b_2$  and  $b_3$  bipeds respond in the same way to the parallel polydirectional loop despite being at different locations. The parallel polydirectional loop does not address the location of the bipeds but only their shape.

We use a parallel pentadirectional loop for the quality control of a competing polymerization addition reaction, Fig. 2d. The loop initiates the addition of a  $b_2$  and a  $b_6$  biped as well as the addition of a  $b_4$  and a  $b_6$  biped. Both, the  $b_2$  and the  $b_4$  bipeds are set on a topologically nonequivalent collision course with  $b_6$  bipeds. The products of the addition polymerization reactions are a  $b_8$  and a  $b_{10}$  biped that are topologically distinct and can be separated from each other as well as from the transport direction of the educts.

In Fig. 2e we plot the trajectories of six bipeds of different lengths after completion of several parallel hexadirectional loops

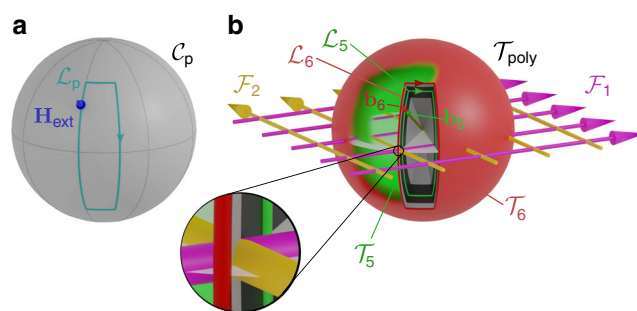


**Fig. 3 Control and transcription spaces.** **a** Polydirectional control space  $C_p$ . Each point on the sphere represents the orientation of the external field. Commands are given as closed loops  $\mathcal{L}_p$ . **b** Polydirectional transcription space  $\mathcal{T}_{poly}$  contains all unidirectional transcription spaces  $\mathcal{T}_n$  that are concentric spheres of radius  $b_n$ . Each point in  $\mathcal{T}_n$  represents the orientation of a biped of length  $b_n$ . One point in  $C_p$  is transcribed into a ray in  $\mathcal{T}_{poly}$ . The unidirectional loops  $\mathcal{L}_5$  (green) and  $\mathcal{L}_6$  (red) wind around different fence lines and they pass on different sides of the (pink)  $\mathcal{F}_1$ - and (yellow)  $\mathcal{F}_2$ -line as can be seen in the magnified inset.

that transport all six different bipeds consistently into six different directions.

Supplementary Movies 2–6 show walking bipeds with tracked experimental trajectories as well as the driving parallel polydirectional loops. The details of the parallel polydirectional loops are provided in Supplementary Note 1 and Supplementary Figs. 1–3. Supplementary Movie 7 shows the trajectories of the tetradirectional command, panel Fig. 2c, according to Brownian dynamics simulations. The agreement between simulations (Supplementary Movie 7) and experiment (Supplementary Movie 4) is excellent.

**Theory.** As we show next, the reason we can independently and simultaneously transport up to six different particles is topological protection. Let  $\mathbf{H}_{ext}(t)$  be the uniform time,  $t$ , dependent external field, and  $\mathbf{H}_p = \nabla\psi$  the spatially nonuniform and time-independent magnetic field generated by the pattern, with  $\psi(\mathbf{r})$  the magnetostatic potential of the pattern, and  $\mathbf{r} = (\mathbf{r}_A, z)$  the position vector with components  $\mathbf{r}_A$  in the plane parallel to the pattern and  $z$  normal to it.

**Control space.** The polydirectional control space  $C_p$  is the surface of a sphere, Fig. 3a, which represent all possible orientations of  $\mathbf{H}_{ext}$ . Parallel commands are given in the form of closed loops  $\mathcal{L}_p$  in  $C_p$ .

**Transcription space.** The orientation of the (dipolar) biped is locked to that of the external field with the northern foot being a magnetic north pole and the southern foot being a south pole. Let  $\mathbf{b}_n$  denote the vector from the northern foot to the southern foot of a biped of length  $b_n$ , Fig. 1a. The southern (northern) foot is on the ground if  $\mathbf{H}_{ext}$  points into the south (north) of  $C_p$ . When  $\mathbf{H}_{ext}$  crosses the equator of  $C_p$ , the biped is parallel to the pattern and the transfer between the feet occurs. Given the one-to-one correspondence between the biped orientation  $\mathbf{b}_n$  and that of the external field, we use  $\mathbf{b}_n$  to define unidirectional transcription spaces  $\mathcal{T}_n$  given by the surface of a sphere of radius  $b_n$ . Each point on  $\mathcal{T}_n$  corresponds to an orientation of a biped of length  $b_n$  and there exists a one-to-one mapping between  $C_p$  and  $\mathcal{T}_n$ . All unidirectional transcription spaces  $\mathcal{T}_n$  can be jointly represented in a polydirectional transcription space  $\mathcal{T}_{poly}$  as concentric spheres of radius  $b_n$ , Fig. 3b. One point in polydirectional control space  $C_p$  is simultaneously translated into a ray in polydirectional transcription space  $\mathcal{T}_{poly}$ . The intersection between the ray and each

unidirectional transcription space is a point that indicates the orientation of the rod. The entire modulation loop  $\mathcal{L}_p$  in  $\mathcal{C}_p$  is transcribed into a cone with arbitrary cross-section in  $\mathcal{T}_{\text{poly}}$ . The intersection between  $\mathcal{T}_n$  and the cone is  $\mathcal{L}_n$ , the modulation loop for bipeds of length  $b_n$ .

**Topological classes.** A biped is subject to a total potential dominated by  $-\mathbf{H}_{\text{ext}} \cdot \mathbf{H}_p$ , the coupling between the external and the pattern fields<sup>22,23</sup>. This coupling leads to an effective biped potential  $V_n$  proportional to the difference in magnetostatic potential at the two feet. That is,

$$V_n(\mathbf{r}, \mathbf{b}_n) \propto \psi(\mathbf{r} + \mathbf{b}_n/2) - \psi(\mathbf{r} - \mathbf{b}_n/2), \quad (1)$$

with the biped centered at  $\mathbf{r}$ . Note  $V_n$  depends explicitly on  $\mathbf{H}_{\text{ext}}$  via the one-to-one correspondence between  $\mathbf{b}_n$  and  $\mathbf{H}_{\text{ext}}$ . Transport of a biped  $b_n$  after completion of one modulation loop  $\mathcal{L}_n$  occurs provided that  $\mathcal{L}_n$  winds around fences, which are those orientations  $\mathbf{b}_n$  for which the potential is marginally stable<sup>23</sup>, i.e., the set of biped orientations for which  $\nabla V_n = 0$  and  $\det(\nabla \nabla V_n) = 0$ . For the present square pattern, both conditions are fulfilled along two perpendicular lines in  $\mathcal{T}_{\text{poly}}$  running through the origin ( $b_n = 0$ ) and parallel to the lattice vector directions. The biped potential is periodic and invariant under the simultaneous transformation  $\mathbf{b}_n \rightarrow \mathbf{b}_n + \mathbf{a}_i$  and  $\mathbf{r} \rightarrow \mathbf{r} + \mathbf{a}_i/2$  with  $\mathbf{a}_i$ ,  $i = \{1, 2\}$ , a lattice vector, cf. Eq. (1). The same periodicity in  $\mathcal{T}_{\text{poly}}$  applies therefore to the fences, which form a square grid of two mutually perpendicular sets of parallel lines separated by one lattice vector,  $\mathcal{F}_1$  and  $\mathcal{F}_2$ , see Fig. 3b. The fences lie in the equatorial plane of  $\mathcal{T}_{\text{poly}}$  (the plane of biped orientations parallel to the pattern). In each unidirectional transcription space  $\mathcal{T}_n$  the fences are points on the equator. Winding around a single fence line of  $\mathcal{F}_i$  transports the biped by one lattice vector  $\pm \mathbf{a}_i$ , depending on whether the loop winds in the same (+) or opposite (−) sense than the axial fence vector. Note that fence lines and lattice vectors are rotated by ninety degrees, cf. Figs. 1 and 2. After completion of a loop  $\mathcal{L}_n$ , a biped  $b_n$  is displaced by

$$\Delta \mathbf{r}(\mathcal{L}_n) = w_n^1(\mathcal{L}_n) \mathbf{a}_1 + w_n^2(\mathcal{L}_n) \mathbf{a}_2, \quad (2)$$

where  $\mathbf{w}_n = (w_n^1, w_n^2)$  is the set of winding numbers of  $\mathcal{L}_n$  around the fences  $\mathcal{F}_1$  and  $\mathcal{F}_2$ . Two bipeds  $b_n$  and  $b_m$  of lengths smaller than the lattice constant  $a$  fall in the same topological class since for both of them there exist only two fence lines. Hence, any parallel polydirectional loop  $\mathcal{L}_p$  in  $\mathcal{C}_p$  is transcribed into modulation loops  $\mathcal{L}_n$  and  $\mathcal{L}_m$  that have the same set of winding numbers, i.e.,  $\mathbf{w}_n = \mathbf{w}_m$ . However, two bipeds where at least one length is larger than the lattice constant, can be transported independently since it is always possible to find a parallel polydirectional loop in  $\mathcal{C}_p$  that is transcribed into two loops  $\mathcal{L}_n$  and  $\mathcal{L}_m$  with different winding numbers. That is, there exists a parallel polydirectional loop for which  $b_n$  and  $b_m$  fall into different topological classes. Examples of such loops are shown in Fig. 3.

**Polydirectional degree.** Theoretically and provided that no more than one biped is shorter than the lattice constant, it is always possible to find a parallel polydirectional loop  $\mathcal{L}_p$  that transports a collection of bipeds of different lengths independently. We call the number of simultaneously controlled lengths the degree of the parallel polydirectional loop. In Fig. 2 we have shown parallel polydirectional loops of degrees 2–6.

**Robustness.** The limitations in practice arise due to several factors such as the precision of the orientation of the field or deviations due to colloidal polydispersity. Let  $\Delta(\mathcal{L}_n)$  be the minimum Euclidian distance from the unidirectional loop  $\mathcal{L}_n$  and

all the fences in  $\mathcal{T}_{\text{poly}}$ . Then  $\Delta(\mathcal{L}_n)$  provides a direct measurement of the robustness of the transport of a biped  $b_n$ ; the larger value of  $\Delta$ , the more robust the transport is. We define the robustness of a parallel polydirectional loop of degree  $l$  transporting a set of bipeds of lengths  $\{b_{n_1}, \dots, b_{n_l}\}$  as the minimum value of all individual distances to the fences, i.e.,

$$\rho(\mathcal{L}_p) = \frac{2}{a} \min\{\Delta(\mathcal{L}_{b_{n_1}}), \dots, \Delta(\mathcal{L}_{b_{n_l}})\}, \quad (3)$$

where the prefactor  $2/a$  normalizes the robustness such that  $0 < \rho < 1$ . The robustness decreases with the polydirectional degree, see values in Fig. 2. Experimentally the transport with parallel hexadirectional loops  $\mathcal{L}_p$  of robustness as low as  $\rho = 0.06$  is still reliable.

**Compaction.** The parallel polydirectional loop is more efficient than multiplexing. That is, addressing sequentially each command, understood as the transport of one biped by one-unit vector. Using parallel polydirectional commands, a single command corresponds to a fundamental loop crossing the equator of  $\mathcal{C}_p$  twice. We define the compaction  $c$  of a target transport as the ratio of the number of parallel polydirectional commands required and the number of commands in multiplexing. We have implemented a program that optimizes the driving loop by reducing the number of commands, while fulfilling the desired robustness requirements for a given set of target bipeds and displacements. The more robustness we require the less compact the parallel polydirectional loop is. One needs to find a compromise between compaction and robustness. Both the compaction and the robustness are indicated in Fig. 2.

Even though we have not designed tasks that are prompted to be compacted, we achieve a compaction of up to 1/2 and much better values can be obtained for suitable tasks. An example with compaction  $c = 1/72$  and robustness  $\rho = 0.02$  is shown in Fig. 4 and Supplementary Movie 8, where thirteen bipeds of different lengths between  $b_2$  and  $b_{19}$  are transported into roughly the same direction but with different magnitudes of the total displacement, which are in all cases commensurate with the lattice constant  $a$ .

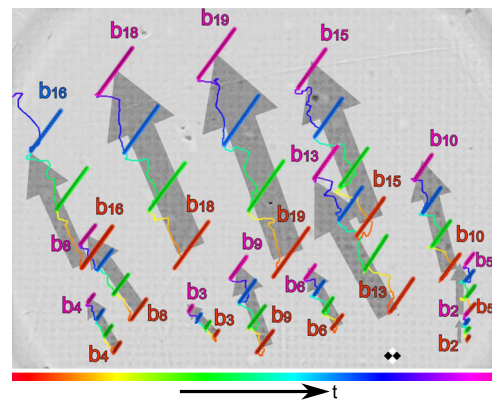


**Fig. 4 Experimental trajectories of bipeds with lengths between  $b_2$  and  $b_{19}$ .** The bipeds are driven by a fundamental loop on a pattern with lattice constant  $a \approx 7 \mu\text{m}$ . The color of each of the thirteen bipeds and their trajectories indicates the time progress of the repeating control loop (see colorbar). The biped  $b_4$  shares the same winding number with the biped  $b_6$ . The biped  $b_{16}$  shares the same winding number with the biped  $b_{18}$ . The low robustness,  $\rho = 0.02$ , causes discrepancies between the theoretically computed and the experimentally observed winding numbers for the bipeds  $b_{13}$  and  $b_{15}$ . The compaction of the loop is  $c = 1/72$ . A square region of the pattern of diagonal  $2a$  is sketched and to indicate the relative orientation.

The modulation loop is shown in Supplementary Fig. 4. Although the robustness is low, the experimental and theoretical winding numbers agree with each other. Only for  $b_{13}$  and  $b_{15}$  the experimental values slightly deviate from the expected winding numbers (error  $\Delta w = \pm 1$ ). Despite this deviation, the modulation can still be used to separate the bipeds but it can no longer be used to steer the bipeds independently into any direction since that requires an exact matching of experimental and theoretical winding numbers.

## Discussion

The complete and simultaneous control over a collection of different objects that we have shown here would be much more difficult to achieve using the ratchet effect. To highlight the differences, consider the transport of stochastic on-off ratchets<sup>2</sup>, in which a periodic biased potential consisting of two nonequivalent minima is repeatedly switched on and off. The potential nonergodically confines a particle to a local minimum during the on-phase. When the potential is switched off, the particles can freely diffuse. Effective ratchet-like transport occurs by adjusting the duration of the off-period, since the diffusive time to escape from each potential minimum depends on the escape direction. A ratchet always needs a finite characteristic frequency, determined by the intrinsic dynamics of the system. It is very difficult to adjust several frequencies for different species such that the ratchet effect can work simultaneously for particles of e.g., different shapes. In our approach, which is conceptually closer to a Thouless pump<sup>29</sup> than to the ratchet effect, we also have a potential that is biased by the external magnetic field. However, we avoid ratchet effects and we do not have an off-period. The bipeds always stay in their local minimum to which they are nonergodically confined. Transport occurs solely due to the parametric dependence of the potential on the external field and the enslaved biped direction. Particles follow adiabatically the local minimum at any time during the modulation. Hence, the transport is not the result of a smart choice of dynamic parameters but due to the complexity of the parametric dependence of the topology of the potential on the external field. The transport occurs in the adiabatic limit of vanishing driving frequency. Since the topology is robust, the transport is also robust and feasible in a finite range of frequencies.

Nevertheless, high modulation frequencies must be avoided due to a broadening of the fences. This broadening has almost no effect when manipulating one or two biped lengths, but it makes it very difficult to prescribe the motion of a collection of bipeds due to the occurrence of ratchets. These two-dimensional ratchets lead not only to flux reversal but also to a directional locking into new directions<sup>4</sup>. Another reason to avoid high modulation frequencies is the shape of the rods. The straight shape of the bipeds is due to the dipolar interactions, but the bipeds are quite flexible. High modulation frequencies alter the shape of the rods, changing therefore the topological properties of the transport. This limitation can be alleviated using rigid anisotropic colloidal particles instead of an assembly of colloidal beads.

We have restricted here to rod-like colloidal particles. Elongated enough particles will behave in a similar fashion independently of the precise shape. We expect particles with significant different shapes, e.g., L- or triangular-like colloidal particles, to have completely different topological properties such that it might be possible to control their transport independently.

In summary, using topological protection we have developed a colloidal parallel polydirectional command which delivers an unprecedented control over the simultaneous motion of a collection of colloidal particles. The parallel polydirectional command addresses individually but simultaneously the motion of up

to six colloidal bipeds of different lengths. Brownian diffusion does not play any role in our system since the external energy is very large compared to the thermal energy. Hence, it would be possible to construct a macroscopic analog of the system using e.g., an arrangement of NbB-magnets<sup>30</sup>. Downscaling the system from the meso- to the nanoscale is challenging since thermal fluctuations might play a role, broadening the fences and facilitating therefore ratchets.

The parallel polydirectional command paves the way to exciting new applications in colloidal science such as e.g., the automatic quality control of chemical reactions and the parallel computing with colloids. Using directional interparticle interactions, such as in the case of patchy colloids<sup>31</sup>, it might be possible to program the assembly of colloids into clusters of complex and predefined shapes that are then transported to the desired direction. Moreover, our methodology and ideas for the simultaneous control of objects that belong to different topological classes can be transferred to other systems for which topological protection is at work.

## Methods

**Pattern.** The pattern is a thin Co/Au layered system with perpendicular magnetic anisotropy lithographically patterned via ion bombardment<sup>32,33</sup>. The pattern consists of a square lattice of magnetized domains with a mesoscopic pattern lattice constant of either  $a = 11 \mu\text{m}$  or  $a = 7 \mu\text{m}$ , see a sketch in Fig. 1a. The magnetic pattern is spin coated with a  $1.6 \mu\text{m}$  polymer film that serves as a spacer.

**External field.** The uniform external magnetic field has a magnitude of  $H_{\text{ext}} = 4 \text{ kA m}^{-1}$  (smaller than the coercive field of the magnetic pattern) and it is generated by three computer-controlled coils arranged around the sample at  $90^\circ$ .

**Preparation of the initial states.** Paramagnetic colloids are dispersed in water and placed above the magnetic pattern. Without external field the colloids are dispersed mainly as single particles above the pattern. Application of the external field leads to the assembly of random length and random position rods above the pattern. A glass capillary with tip diameter of a few micron attached to a micro manipulator is used to change the length and position of the bipeds to the desired relative initial arrangement while the external field remains in the equatorial plane.

**Visualization.** The colloids and the pattern are visualized using reflection microscopy. The pattern is visible because the ion bombardment changes the reflectivity of illuminated regions as compared to that of the masked regions. A camera records video clips of the bipeds.

**Compacted parallel polydirectional loop.** To find the loop  $\mathcal{L}_p$  for given target displacements  $w_{n1}, \dots, w_{nl}$  for a set of target lengths  $b_{n1}, \dots, b_{nl}$  we start by calculating all fence points for each target length. Then, we transcribe the fence points back to control space  $C_p$  by rescaling. All fence points in  $C_p$  lie on the equator (see Fig. 1b yellow and pink circles) and hence they differ only by the azimuthal angle of the external field. For every neighboring fence azimuthal angles we choose one intermediate azimuthal angle between them. These intermediate points are then transcribed to each of the unidirectional transcription spaces of the target set of bipeds and we calculate their minimum distance  $\Delta$  to the fences. The intermediate points having transcriptions with  $\Delta$  smaller than a fixed threshold are discarded. Every pair formed by two of the non-discarded points defines a fundamental parallel polydirectional loop. Every fundamental parallel polydirectional loop causes a unidirectional displacement for every target length and hence can be represented as a displacement in a  $2l$ -dimensional vector space of the  $l$  target lengths. As the target displacements can be represented in this vector space, the parallel polydirectional loop  $\mathcal{L}_p$  can be found as an integer linear combination of fundamental parallel polydirectional loops, i.e., by solving the resulting system of linear equations. Note that only an integer number of every fundamental loop is valid as a solution since only integer winding numbers are possible. If the selected threshold for the robustness is too large, it may be impossible to find an integer solution, but there is always a solution if we sufficiently reduce the minimum robustness. There exist an infinite number of parallel polydirectional loops decoding the same displacements and the one found by solving the linear system of equations is just one of them, not necessarily the most compact. Therefore, we obtain a compaction of this parallel polydirectional loop by searching for pairs (and triplets) of fundamental loops in the parallel polydirectional loop that can be replaced by a single fundamental loop having the same net displacement. This is repeated in an iterative scheme until no further compaction of the loop is found. See Supplementary Movie 9 for a detailed visual explanation of the algorithm.

**Computer simulations.** All parallel polydirectional loops considered here have been also implemented in computer simulations and the colloidal transport matches that found experimentally. Compare, for example, the experimental and simulated trajectories shown in Supplementary Movies 4 and 7, respectively. We simulate the system using overdamped Brownian dynamics. The equation of motion is integrated in time using the standard Euler algorithm. Colloidal particles are modeled as point particles interacting via a Weeks–Chandler–Anderson and a dipolar interparticle potential. Each point particle is subject to the colloidal single particle potential proportional to  $-\mathbf{H}_{\text{ext}} \cdot \mathbf{H}_p(\mathbf{r})$ .

**Fences.** We express the magnetostatic potential as a Fourier series, see refs. 22,23. The Fourier modes decay exponentially such that at sufficiently high elevations only the first mode contributes (the spacer forces the colloids to be at high elevations). The fences are found by simultaneously solving the equations  $\nabla V_n = 0$  and  $\det(\nabla \nabla V_n) = 0$ , which for the case of a square pattern is straight forward. See the example for point particles ( $b_0$ ) in ref. 23.

### Data availability

All the data supporting the findings are available from the corresponding author upon reasonable request.

Received: 9 April 2020; Accepted: 25 August 2020;

Published online: 16 September 2020

### References

- McDonald, M. P., Spalding, G. C. & Dholakia, K. Microfluidic sorting in an optical lattice. *Nature* **426**, 421–424 (2003).
- Reimann, P. Brownian motors: noisy transport far from equilibrium. *Phys. Rep.* **361**, 57–265 (2002).
- Skaug, M. J., Schwemmer, C., Fringes, S., Rawlings, C. D. & Knoll, A. W. Nanofluidic rocking Brownian Mot. *Sci.* **359**, 1505–1508 (2018).
- Gopinathan, A. & Grier, D. G. Statistically locked-in transport through periodic potential landscapes. *Phys. Rev. Lett.* **92**, 130602 (2004).
- Add a language to a polyglot. user62131 et al. Posted Dec 6 '16 at 18:59 <https://codegolf.stackexchange.com/questions/102370/add-a-language-to-a-polyglot> (2017).
- DiVincenzo, D. P. Quantum computation. *Science* **270**, 255–261 (1995).
- Shor, P. W. Polynomial-time algorithms for prime factorization and discrete logarithms on a quantum computer. *SIAM J. Comput.* **26**, 1484–1509 (1997).
- Kitaev, A. Y. Fault-tolerant quantum computation by anyons. *Anna Phys.* **303**, 2–30 (2003).
- Adleman, L. Molecular computation of solutions to combinatorial problems. *Science* **266**, 1021–1024 (1994).
- Lipton, R. J. DNA solution of hard computational problems. *Science* **268**, 542–545 (1995).
- Qian, L. & Winfree, E. Scaling up digital circuit computation with DNA strand displacement cascades. *Science* **332**, 1196–1201 (2011).
- Amir, Y. et al. Universal computing by DNA origami robots in a living animal. *Nat. Nanotechnol.* **9**, 353–357 (2014).
- Church, G. M., Gao, Y. & Kosuri, S. Next-generation digital information storage in DNA. *Science* **337**, 1628 (2012).
- Rothemund, P. W. K. & Folding, D. N. A. to create nanoscale shapes and patterns. *Nature* **440**, 297–302 (2006).
- Ilievski, F., Mazzeo, A. D., Shepherd, R. F., Chen, X. & Whitesides, G. M. Soft robotics for chemists. *Angew. Chem. Int. Ed.* **50**, 1890–1895 (2011).
- Păun, G. Computing with membranes. *J. Comput. Syst. Sci.* **61**, 108–143 (2000).
- Adamatzky, A., Costello, B. D. L. & Asai, T. Reaction-diffusion computer. Elsevier (2005).
- Prakash, M. & Gershenfeld, N. Microfluidic bubble logic. *Science* **315**, 832–835 (2007).
- Kou, S. et al. Fluorescent molecular logic gates using microfluidic devices. *Angew. Chem. Int. Ed.* **47**, 872–876 (2008).
- Phillips, C. L. et al. Digital colloids: reconfigurable clusters as high information density elements. *Soft Matter* **10**, 7468–7479 (2014).
- Cui, J. et al. Nanomagnetic encoding of shape-morphing micromachines. *Nature* **575**, 164–168 (2019).
- Loehr, J. et al. Lattice symmetries and the topologically protected transport of colloidal particles. *Soft Matter* **13**, 5044–5075 (2017).
- de las Heras, D., Loehr, J., Lönne, M. & Fischer, T. M. Topologically protected colloidal transport above a square magnetic lattice. *N. J. Phys.* **18**, 105009 (2016).
- Asbury, C. L. Kinesin: world's tiniest biped. *Curr. Opin. Cell Biol.* **17**, 89–97 (2005).
- Shik, M. L. & Orlovsky, G. N. Neurophysiology of locomotor automatism. *Physiol. Rev.* **56**, 465–501 (1976).
- Hamacher, D., Herold, F., Wiegel, P., Hamacher, D. & Schega, L. Brain activity during walking: a systematic review. *Neurosci. Biobehav. Rev.* **57**, 310–327 (2015).
- Holmes, P., Full, R. J., Koditschek, D. & Guckenheimer, J. The dynamics of legged locomotion: models, analyses, and challenges. *SIAM Rev.* **48**, 207–304 (2006).
- Sherman, W. B. & Seeman, N. C. A precisely controlled DNA biped walking device. *Nano Lett.* **4**, 1203–1207 (2004).
- Thouless, D. J. Quantization of particle transport. *Phys. Rev. B* **27**, 6083–6087 (1983).
- Rossi, A. M. E. B. et al. Hard topological versus soft geometrical magnetic particle transport. *Soft Matter* **15**, 8543–8551 (2019).
- Wang, Y. et al. Colloids with valence and specific directional bonding. *Nature* **491**, 51–55 (2012).
- Chappert, C. et al. Planar patterned magnetic media obtained by ion irradiation. *Science* **280**, 1919–1922 (1998).
- Kuświk, P. et al. Colloidal domain lithography for regularly arranged artificial magnetic out-of-plane monodomains in Au/Co/Au layers. *Nanotechnology* **22**, 095302 (2011).

### Acknowledgements

This work is funded by the Deutsche Forschungsgemeinschaft (DFG, German Research Foundation) under project number 440764520.

### Author contributions

M.M.K., Ad.E., D.d.l.H., and T.M.F. designed and performed the experiment, and wrote the paper with input from all the other authors. M.U. and F.S. produced the magnetic film. J.G., Ar.E., and M.R. performed the fabrication of the micromagnetic domain patterns within the magnetic thin film.

### Funding

Open Access funding provided by Projekt DEAL.

### Competing Interests

The authors declare no competing interests.

### Additional information

Supplementary information is available for this paper at <https://doi.org/10.1038/s41467-020-18467-9>.

Correspondence and requests for materials should be addressed to T.M.F.

Peer review information *Nature Communications* thanks David Grier, Giovanni Volpe and the other, anonymous, reviewer(s) for their contribution to the peer review of this work. Peer reviewer reports are available.

Reprints and permission information is available at <http://www.nature.com/reprints>

Publisher's note Springer Nature remains neutral with regard to jurisdictional claims in published maps and institutional affiliations.



**Open Access** This article is licensed under a Creative Commons Attribution 4.0 International License, which permits use, sharing, adaptation, distribution and reproduction in any medium or format, as long as you give appropriate credit to the original author(s) and the source, provide a link to the Creative Commons license, and indicate if changes were made. The images or other third party material in this article are included in the article's Creative Commons license, unless indicated otherwise in a credit line to the material. If material is not included in the article's Creative Commons license and your intended use is not permitted by statutory regulation or exceeds the permitted use, you will need to obtain permission directly from the copyright holder. To view a copy of this license, visit <http://creativecommons.org/licenses/by/4.0/>.

© The Author(s) 2020

# Publication 3

---

## Supporting Information



### SUPPLEMENTARY NOTE 1

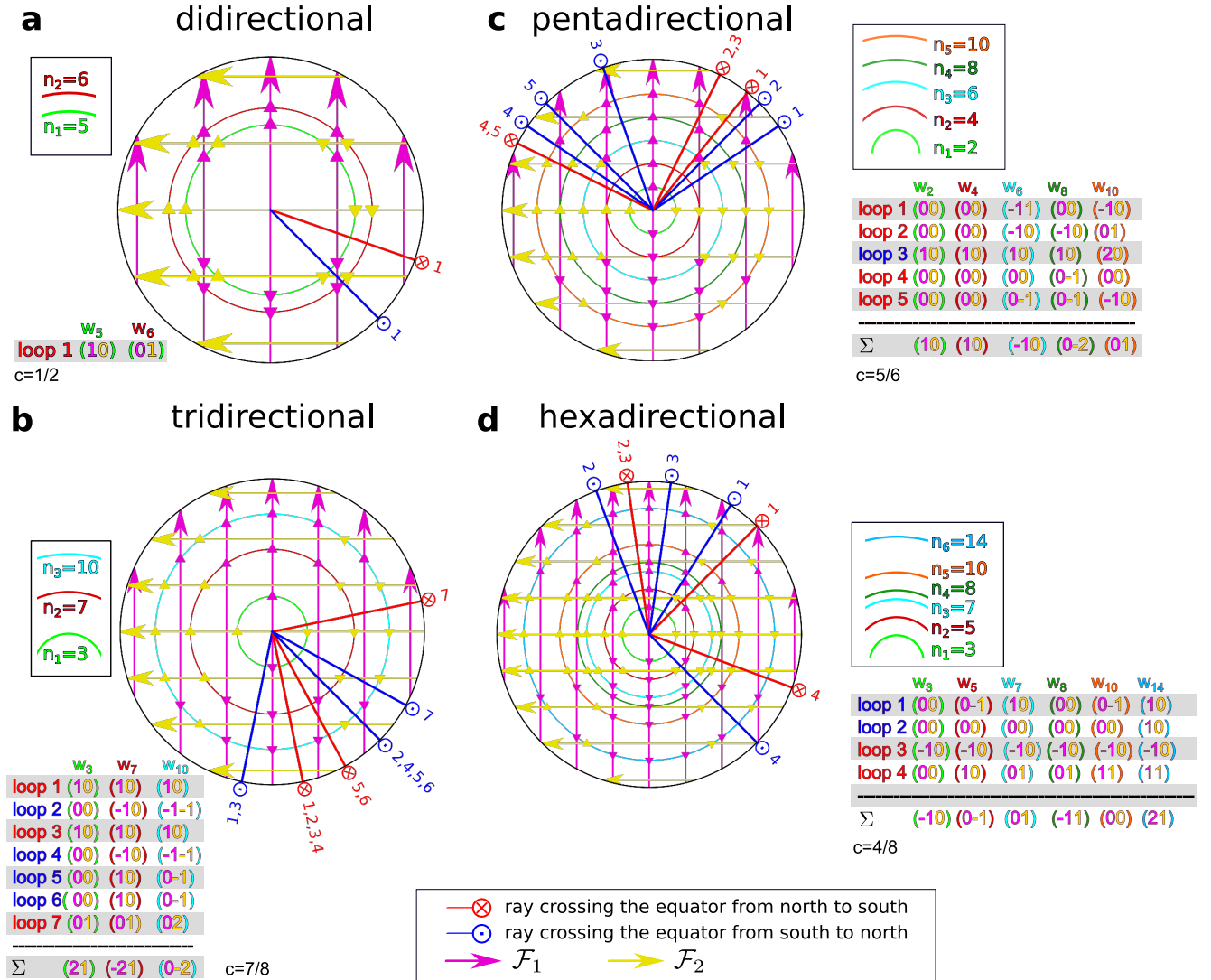
We describe here the parallel polydirectional loops used to control the simultaneous motion of bipeds shown in both Fig. 2 of the main text and the Supplementary Movies. In all cases, the loops are shown in polydirectional transcription space  $\mathcal{T}_{\text{poly}}$ . The loops transport a set of  $l$  bipeds of lengths  $b_{n1}, \dots, b_{nl}$ . Supplementary Fig. 1 shows the loops that control the motion of the parallel didirectional command  $l = 2$  (a), the parallel tridirectional command  $l = 3$  (b), the parallel pentadirectional command  $l = 5$  (c), and the parallel hexadirectional command  $l = 6$  (d). The parallel tetradirectional loop  $l = 4$  is depicted in Supplementary Fig. 2.

In both figures we plot a top view of the equatorial plane in  $\mathcal{T}_{\text{poly}}$ , the cuts of the target unidirectional spheres  $\mathcal{T}_{n1}, \dots, \mathcal{T}_{nl}$  with the equatorial plane (colored concentric circles), the fences  $\mathcal{F}_i$  with  $i = 1, 2$ , and the rays in  $\mathcal{T}_{\text{poly}}$  that are transcribed into  $\mathcal{T}_{\text{poly}}$  from the equatorial crossings of the parallel polydirectional loop  $\mathcal{L}_p$  in control space  $\mathcal{C}_p$ . A fundamental parallel polydirectional loop  $\mathcal{L}_p$  in  $\mathcal{C}_p$  can wind in the clockwise (-) or counterclockwise (+) direction around the fence points within the smaller enclosed area. In Supplementary Fig. 1 and Supplementary Fig. 2 we show tables next to each equatorial plane indicating whether the loop winds clockwise (red) or counterclockwise (blue).

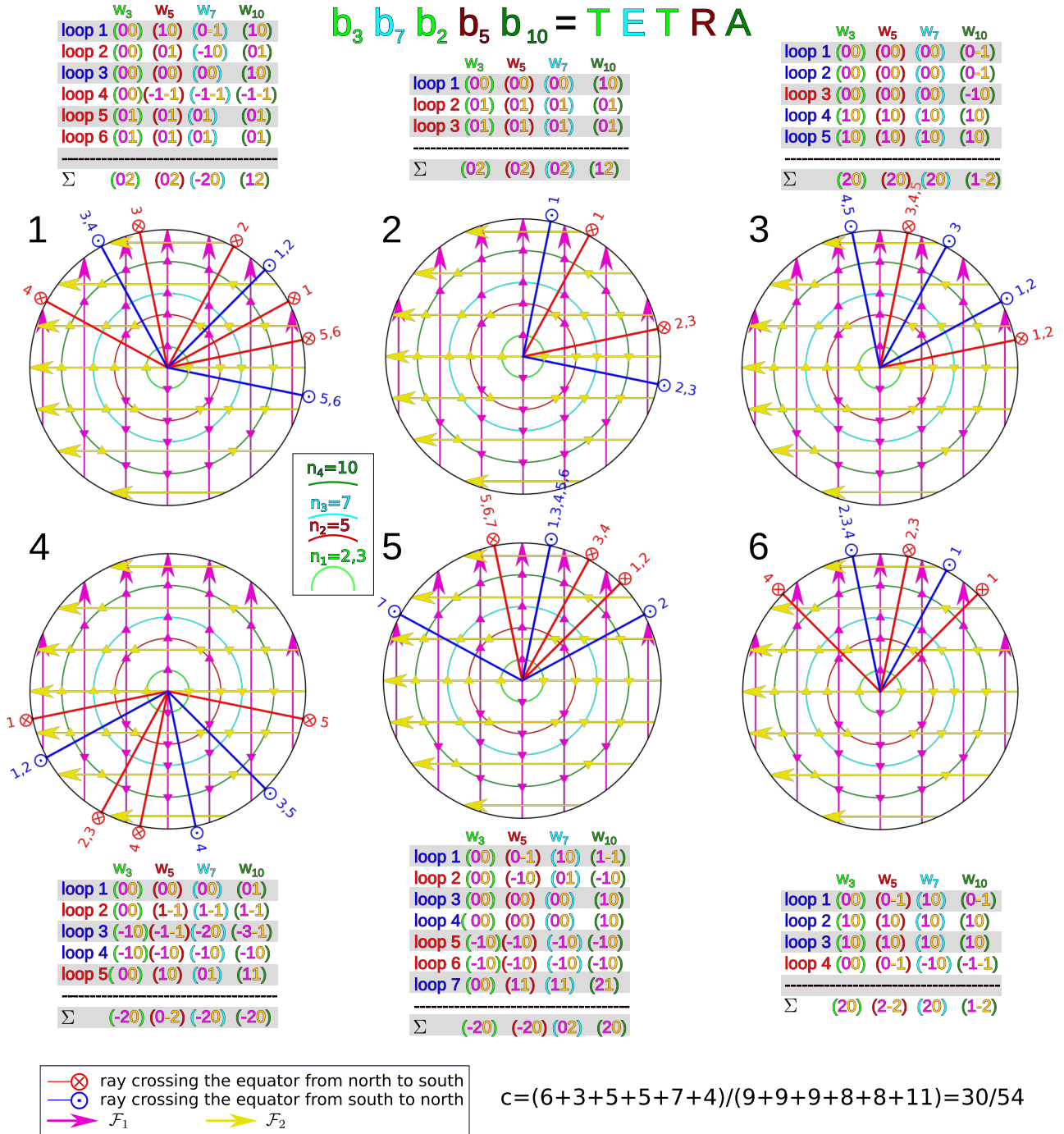
Up and down triangles are drawn at the intersections of the fences with the unidirectional transcription spheres. Triangles are up (down) if the scalar product of the tangent vector of the ray toward the triangle with the tangent vector of the fence is positive (negative). Taking the difference of up triangles and down triangles on a unidirectional arc inside a fundamental cone and multiplying with the winding sense of the fundamental loop gives the winding number of the particular unidirectional fundamental loop  $\mathcal{L}_{ni}$  for the chosen target length  $b_{ni}$ . Hence, the winding numbers can be read directly from the equatorial plots. In addition, all winding numbers are listed in the tables.

In Supplementary Fig. 3 we show a complex heptadirectional loop. We aim the reader to decipher the associated winding numbers and trajectories.

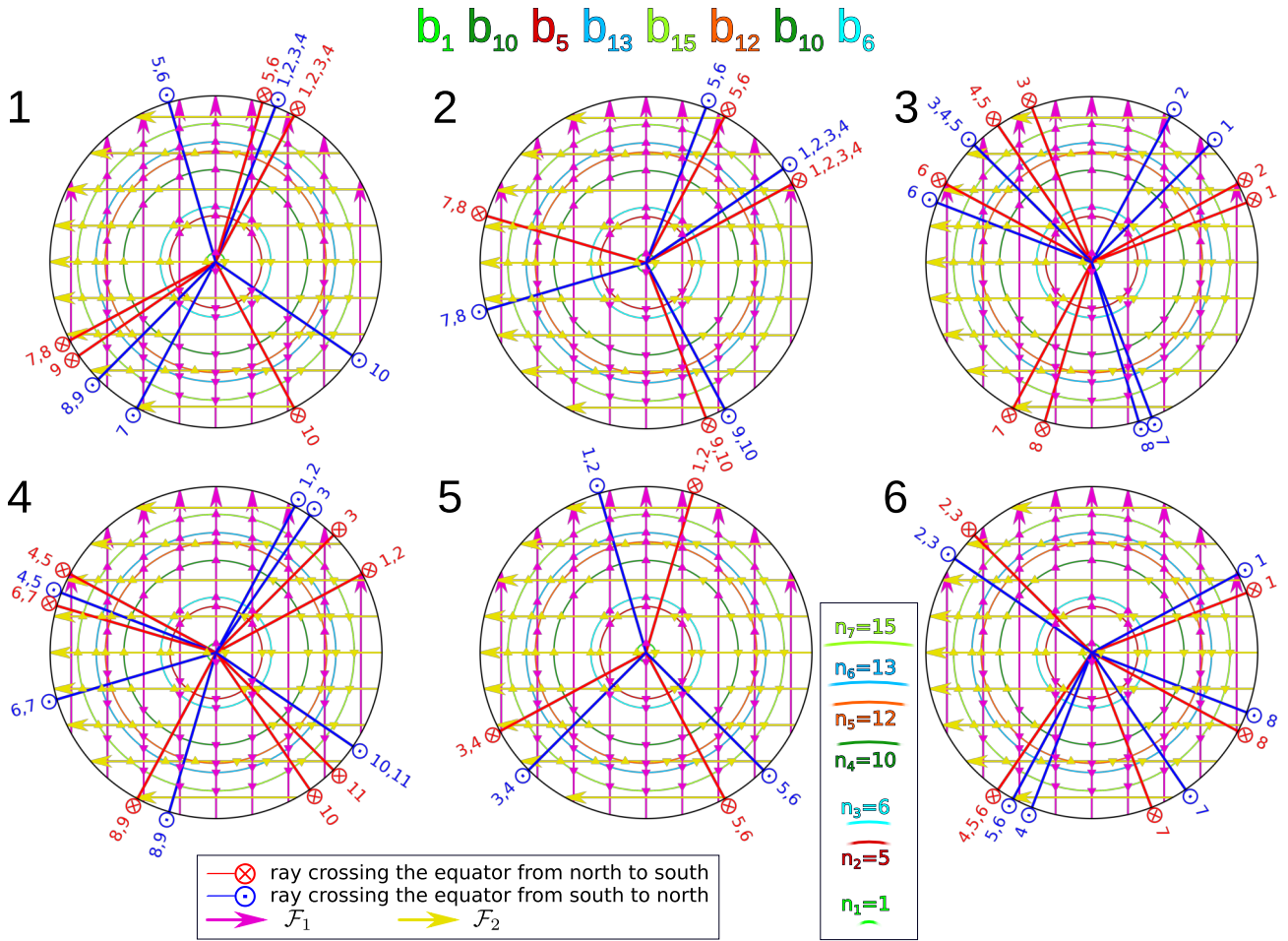
Finally, in Supplementary Fig. 4 we show a complex undecasorting loop with a table comparing the experimental and theoretical winding numbers.



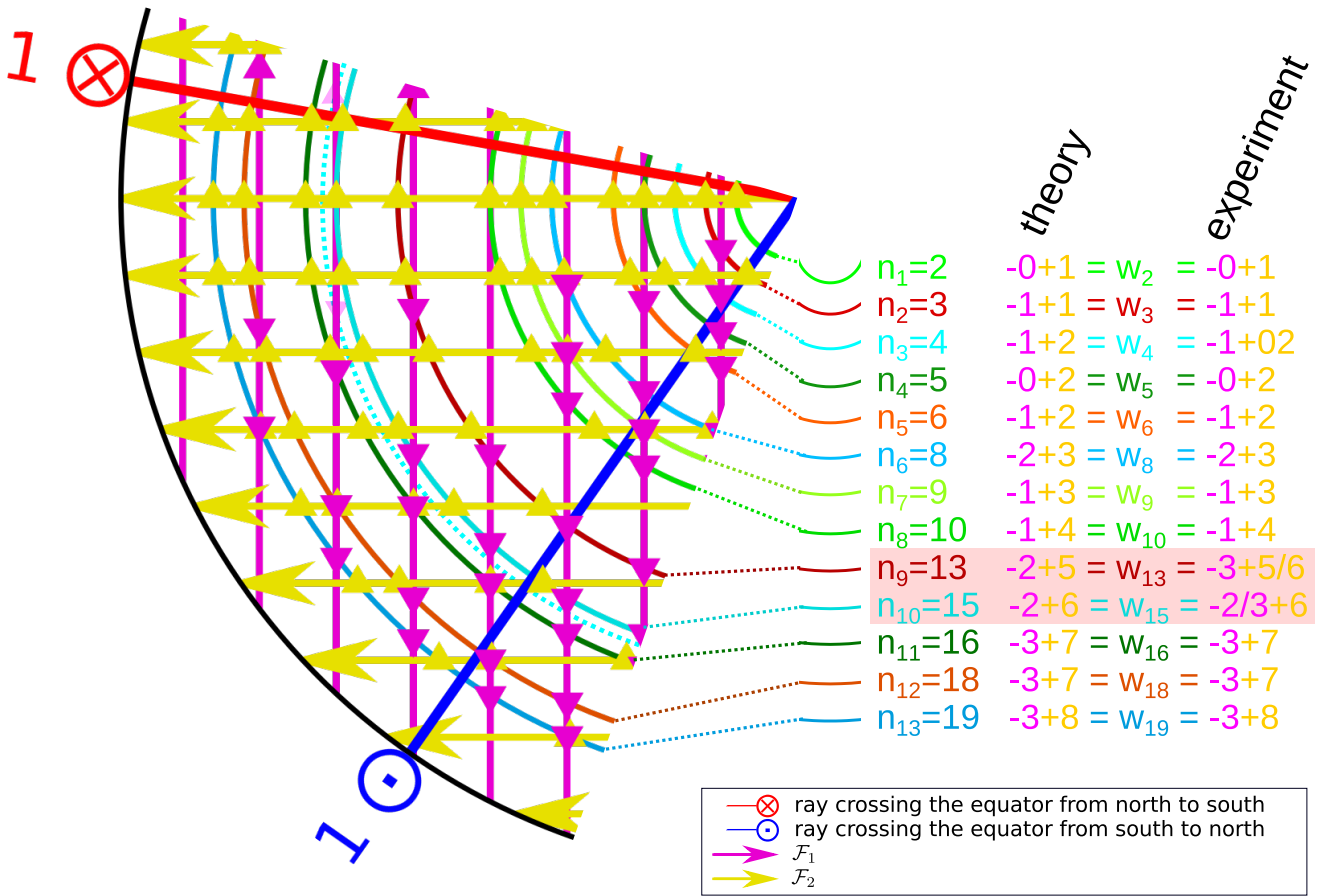
Supplementary Fig. 1. **Modulation loops in transcription space  $\mathcal{T}_{\text{poly}}$ .** Top view of the equatorial plane of  $\mathcal{T}_{\text{poly}}$  showing the fences  $\mathcal{F}_1$  and  $\mathcal{F}_2$ , the unidirectional transcription spaces (concentric circles)  $\mathcal{T}_{n_i}$  with  $i = 1, \dots, l$  and  $l$  the number of different bipeds transported by the loop, and the modulation loops of **a** the parallel didirectional command, **b** the parallel tridirectional command, **c** the parallel pentadirectional command and **d** the parallel hexadirectional command. A table indicating the winding numbers around each fence and the compaction of the loop are also depicted for each case. The procedure to read the loops is as follows. Pick the first fundamental loop 1 and determine its orientation ( $\pm 1$  for mathematical positive respectively negative sense). For example, loop 1 of the parallel didirectional command (parallel hexadirectional command) has negative (positive) orientation. Next, subtract the number of pink-down triangles from that of pink-up triangles on the  $b_{n_1}$  arcs of the fundamental loop 1 and multiply it with the orientation of the loop to obtain the  $\mathbf{a}_1$ -displacement of the  $n_1$ -biped during the loop 1. Repeat same procedure with the yellow triangles to obtain the  $\mathbf{a}_2$ -displacement. Repeat this for the other lengths  $b_{n_2} - b_{n_1}$  to obtain all unidirectional displacements. Count the total number of fundamental loops of the polydirectional command and compare it with the number of nearest neighbor displacements needed if multiplexing. To each polydirectional command we provide a table with the winding numbers of the fundamental loops as well as the sum of the concatenated complex polydirectional command for comparison. Fundamental loops with positive (negative) orientations are marked as blue (red) in the table.



Supplementary Fig. 2. **Modulation loop in transcription space  $\mathcal{T}_{\text{poly}}$  for the parallel tetradirectional command.** The loop induces a set of  $l = 5$  bipeds to write the word TETRA as shown in Fig. 2c of the main text and the Supplementary Videos. Each letter is written in six different steps. Each equatorial plane shown in the figure represents one of these steps, as indicated. See caption of Fig. 1 for a complete explanation on how to read the fundamental loops. The word TETRA appears when the bipeds are ordered as  $b_3, b_7, b_2, b_5, b_{10}$ .



Supplementary Fig. 3. **Parallel heptadirectional command.** The loop encrypts seven letters, each one with six steps. Each equatorial plane contains the fundamental loops of one step. All fundamental loops have positive orientation here. The procedure to read the loops is the same as that explained in the caption of Fig. 1. The encrypted word appears when the bipeds are ordered as  $b_1, b_{10}, b_5, b_{13}, b_{15}, b_{12}, b_{10}, b_6$ . The compaction of the loop is  $c = 30/54$  (see caption of Fig. 1 for an explanation on how to calculate the compaction). If you find a robust parallel heptadirectional command with less fundamental loops encoding the same word, please let us know!



Supplementary Fig. 4. **Modulation loops in transcription space  $\mathcal{T}_{\text{poly}}$ .** Top view of the equatorial plane of  $\mathcal{T}_{\text{poly}}$  showing the fences  $\mathcal{F}_1$  and  $\mathcal{F}_2$ , the unidirectional transcription spaces (concentric circles)  $\mathcal{T}_{ni}$  with  $i = 1, \dots, 13$  of the thirteen different bipeds transported by the loop, and the modulation loops of parallel undecasorting command. A table indicating the theoretical winding numbers around each fence and the experimentally observed winding numbers of the motion illustrated in Fig 4 of the main text are listed for a comparison. Discrepancies in winding numbers occur for the bipeds  $b_{13}$  and  $b_{15}$ , which are marked in red in the table. An incomplete locking between  $\mathbf{H}_{\text{ext}}$  and  $\mathbf{b}_{13}$  due to nonadiabatic effects could be the reason for observed differences for the  $b_{13}$ -biped, for which  $\mathcal{T}_{13}$ ,  $\mathcal{F}_2$  and  $\mathcal{L}_{13}$  almost fall on top of each other. The dotted transcription space is a transcription space for biped size  $b_{15.3} > b_{15}$ , that would contain an extra crossing of the fence  $\mathcal{F}_1$ , shown as transparent pink triangle demonstrating that a 2% increase in length of the biped could explain the discrepancies between experiment and theory for the  $b_{15}$ -biped.

## Description of Additional Supplementary Files

**Supplementary movie 1.mp4** Brownian dynamics simulation of a  $b_5$  biped subject to the loop presented in figure 1 and figure 3. The foot of the biped must slide into the position that commensurate with the lattice when the control loop of the external field passes close to a fence point.

**Supplementary movie 2.mp4** Reflection microscopy recording of the experiment of the didirectional command in figure 2a. To the right we show the motion of the external field in control space and the equatorial plane of the polydirectional transcription space.

**Supplementary movie 3.mp4** Reflection microscopy recording of the experiment of the tridirectional command in figure 2b. To the right we show the motion of the external field in control space and the equatorial plane of the polydirectional transcription space.

**Supplementary movie 4.mp4** Reflection microscopy recording of the experiment of the tetradirectional command in figure 2c. To the right we show the equatorial plane of the polydirectional transcription space. The tetradirectional command consists of six complex loops that are repeated three times and they have different rays in the equatorial planes.

**Supplementary movie 5.mp4** Reflection microscopy recording of the experiment of the pentadirectional command in figure 2d. To the right we show the equatorial plane of the polydirectional transcription space.

**Supplementary movie 6.mp4** Reflection microscopy recording of the experiment of the hexadirectional command in figure 2e. To the right we show the equatorial plane of the polydirectional transcription space.

**Supplementary movie 7.mp4** Brownian dynamics simulation of the tetradirectional command shown in figure 2c. Corresponding experiments are shown in Supplementary Movie 4.

**Supplementary movie 8.mp4** Reflection microscopy recording of the experiment of the undecasorting command in figure 4. To the right we show the equatorial plane of the polydirectional transcription space. At the end of the movie we show that the bipeds are indeed self assembled bipeds that depolymerize to monomers and dimers if we switch off the external field.

**Supplementary movie 9.mp4** Visual explanation of the algorithm to find a compacted loop with the desired transport directions.

# Publication 4

---

## Gauge invariant and gauge dependent aspects of topological walking colloidal bipeds

*Soft Matter* **17**, 1663-1674 (2021)

Mahla Mirzaee-Kakhki,<sup>a1</sup> **Adrian Ernst**,<sup>a1</sup>  
Daniel de las Heras,<sup>a2</sup> Maciej Urbaniak,<sup>b</sup>  
Feliks Stobiecki,<sup>b</sup> Andreea Tomita,<sup>c</sup> Rico Huhnstock,<sup>c</sup>  
Iris Koch,<sup>c</sup> Arno Ehresmann,<sup>c</sup> Dennis Holzinger,<sup>c</sup> &  
Thomas M. Fischer<sup>a1</sup>

<sup>a1</sup> Experimental Physics X and <sup>a2</sup> Theoretical Physics II, Department of Physics, University of Bayreuth, 95447 Bayreuth, Germany.

<sup>b</sup> Institute of Molecular Physics, Polish Academy of Sciences, 60-179 Poznań, Poland.

<sup>c</sup> Institute of Physics and Center for Interdisciplinary Nanostructure Science and Technology (CINSA-T), University of Kassel, 34132 Kassel, Germany.

---

### My Contribution

Mahla Mirzaee-Kakhki performed the experiments. I worked out the mathematical part, the computer control, and simulations of the experiments. Daniel de las Heras supervised the simulations and Thomas Fischer the experiments. The authors from Poznań grew the magnetic films and the authors from Kassel Helium bombarded them to create the magnetic patterns. The preparation and writing of the paper was done by all authors.





Cite this: *Soft Matter*, 2021,  
17, 1663

## Gauge invariant and gauge dependent aspects of topological walking colloidal bipeds†

Mahla Mirzaee-Kakhki,<sup>a</sup> Adrian Ernst,<sup>ib</sup><sup>a</sup> Daniel de las Heras,<sup>id</sup><sup>a</sup> Maciej Urbaniak,<sup>b</sup> Feliks Stobiecki,<sup>ib</sup><sup>b</sup> Andreea Tomita,<sup>c</sup> Rico Huhnstock,<sup>c</sup> Iris Koch,<sup>c</sup> Arno Ehresmann,<sup>ib</sup><sup>c</sup> Dennis Holzinger<sup>c</sup> and Thomas M. Fischer<sup>id</sup><sup>\*a</sup>

Paramagnetic colloidal spheres assemble to colloidal bipeds of various length in an external magnetic field. When the bipeds reside above a magnetic pattern and we modulate the direction of the external magnetic field, the rods perform topologically distinct classes of protected motion above the pattern. The topological protection allows each class to be robust against small continuous deformations of the driving loop of the external field. We observe motion of the rod from a passive central sliding and rolling motion for short bipeds toward a walking motion with both ends of the rod alternately touching down on the pattern for long bipeds. The change of character of the motion occurs in form of discrete topological transitions. The topological protection makes walking a form of motion robust against the breaking of the non symmorphic symmetry. In patterns with non symmorphic symmetry walking is reversible. In symmorphic patterns lacking a glide plane the walking can be irreversible or reversible involving or not involving ratchet jumps. Using different gauges allows us to unravel the active and passive aspects of the topological walks.

Received 16th September 2020,  
Accepted 10th December 2020

DOI: 10.1039/d0sm01670e

rsc.li/soft-matter-journal

### 1 Rolling, walking, and limping

Rolling is a process where a wheel winds around its axis and thereby translates on a support. If the propulsion distance of the wheel matches the wheel circumference the rolling is with a non-slip condition. Otherwise the rolling is with slip. Walking is generically a symmetric process differing from rolling. A walker progresses in steps by moving his feet and depending on the number of feet we call the walker a biped, triped, quadruped *etc.* A human is an example of a biped, where both feet of a walking person perform alternating steps. The spatial period of the walk of a biped is two steps, – not one step –, since the conformation of a person is restored after two steps and the conformation after an odd number of steps is related to the conformation after an even number of steps by a non-symmorphic group operation (a half period translation followed by a reflection known as a glide plane). The non-symmorphic symmetry can be broken in a trivial manner for example by

breaking one of our legs in which case we start limping and the broken leg functions differently than its non-broken mirror image partner.

We may view symmetric walking as a symmetry reduced form of rolling and limping as a symmetry reduced form of walking. For a rolling wheel all orientations of the wheel are of equivalent importance. A full rotation of the wheel passes through all equivalent orientations of the wheel in a continuous way. For a symmetric walker the symmetry of the motion is reduced to a two fold discrete symmetry as compared to the continuous symmetry of the wheel. The symmetry is further reduced when the walker limps.

A subtle, albeit psychologically undesirable<sup>1</sup> way of breaking the non-symmorphic symmetry of a symmetric walker is by letting him walk on a periodic structure with a period of the pattern commensurable with his step width. If the pattern has the period of one step but lacks the mirror symmetry of the non-symmorphic group operation of our two-step-periodic walker, we expect one foot to perform in a symmetry broken way compared to the other foot. One example of such walking is the motor protein Kinesin. It accomplishes transport by walking with its two heads (not its two feet) along a microtubule. The microtubule is a chiral periodic structure that lacks mirror symmetries such that we expect differences between the two heads even when the two heads walk in a “hand-over-hand” mechanism, where the kinesin heads step past one another, alternating the lead position.<sup>2,3</sup>

<sup>a</sup> University of Bayreuth, Physics, Universitätsstr. 30, 95447 Bayreuth, Germany.

E-mail: Thomas.Fischer@uni-bayreuth.de

<sup>b</sup> Institute of Molecular Physics, Polish Academy of Sciences,

ul. M. Smoluchowskiego 17, 60-179 Poznań, Poland

<sup>c</sup> Institute of Physics and Center for Interdisciplinary Nanostructure Science and Technology (CINSaT), University of Kassel, Heinrich-Plett-Strasse 40, D-34132 Kassel, Germany

† Electronic supplementary information (ESI) available. See DOI: 10.1039/d0sm01670e

A subtle way to allow for symmetric walking on a periodic pattern is to use a pattern with primitive unit vectors of two steps. If the space group of the pattern is non-symmorphic, containing the non-symmorphic group operation of our walker, the walker can still walk in a symmetric way.

If instead we use a symmorphic pattern containing only symmorphic group elements the walker is expected to walk in a symmetry-broken way. Its left foot has to step onto a position that is not related by a symmetry operation to the position the right foot steps upon.

A further way of breaking the symmetry of a walker exists for driven systems, where the walker responds to external commands. If those commands lack a non-symmorphic symmetry in time our walker will perform a walk lacking the non-symmorphic glide symmetry.

## 2 Robust walking

Rolling and walking are both usually generated by a cyclic change of certain parameters that control and drive the motion. These parameters can be as diverse as certain signals of the spinal chord for walking humans<sup>4,5</sup> or walking animals,<sup>6</sup> the concentration of complementary DNA-strands as well as temperature in DNA-bipeds,<sup>7</sup> or the geometric shape for geometric swimmers at low Reynolds numbers.<sup>8,9</sup> We can thus define a control space  $\mathcal{C}$  that is the space of possible parameters that might occur while we drive the motion. For robust walking the result of a slightly perturbed loop in control space  $\mathcal{C}$  must result in a successful sequence of walking steps albeit the disturbance of the loop. For robotic walkers mathematical algorithms such as Lyapunov function based control algorithms or control barrier functions are employed to guarantee safe walking.<sup>10</sup> Another powerful way of ensuring such robust behavior is the use of topological invariants.<sup>11–23</sup> If the control space  $\mathcal{C}$  is a not simply connected space the winding number  $w(\mathcal{L}_C)$  of a loop  $\mathcal{L}_C$  around the holes in control space constitutes a topological invariant. A walk on a pattern is a topological walk if the number of steps  $n_{\text{step}} = mw(\mathcal{L}_C)$  on the pattern is a non zero but low integer multiple ( $m = \pm 1, \pm 2, \dots$ ) of the winding number irrespective of the details of how precisely and with which speed the loop in control space winds around a hole.

This robustness includes perturbations that break the non-symmorphic symmetry. When the walking is topologically robust, then the stronger foot of the walker must consistently make up for its weaker partner in order to secure the commensurability with the period of the pattern. The robustness, however, also holds when we extend the two fold symmetry of a walker to the continuous symmetry of a rolling wheel. The space of orientations of a wheel is a not simply connected space and thus topological invariants can be used to control their motion on a pattern. In this work we morph the topological sliding rolling of a colloidal wheel into the topological equivalent motion of self assembled colloidal rods that either slide and roll or walk on symmorphic and non-symmorphic magnetic lattices. We show the topological robustness of the

transport by successively deforming the wheel into a biped and by continuously changing the character of the motion from rolling toward walking. Topological transitions toward larger bipeds with discretely increasing step widths occur as the self assembled biped grows longer.

## 3 Experimental setup

We illustrate the richness of biped motion using a square magnetic lattice (Fig. 1a)<sup>24,25</sup> with a glide plane and a magnetic hexagonal lattice (Fig. 1c) containing no glide plane. We study experimentally and with computer simulations the character of the biped motion. In the experiments, paramagnetic colloidal particles (negatively charged COOH-functionalized paramagnetic Dynabeads M-270 of radius  $R = 1.4 \mu\text{m}$  and effective magnetic susceptibility  $\chi_{\text{eff}} = 0.6$ ) assembled to a rod of  $n = 2–11$  particles move above a thin Co/Au layered system with perpendicular magnetic anisotropy lithographically patterned *via* ion bombardment.<sup>25–27</sup> The pattern consists of a square (hexagonal) lattice of magnetized domains with a mesoscopic pattern lattice constant  $a \approx 7 \mu\text{m}$ , see a sketch in Fig. 1a and c. The whole pattern is magnetized in the  $\pm z$ -direction normal to the film. The magnetic pattern is spin coated with a  $1.6 \mu\text{m}$  polymer film that serves as a spacer. The paramagnetic colloidal particles are immersed in water. A uniform time-dependent external magnetic field  $\mathbf{H}_{\text{ext}}(t)$  of constant magnitude ( $H_{\text{ext}} = 4 \text{ kA m}^{-1}$ ) is superimposed to the non-uniform and time-independent magnetic field generated by the pattern  $\mathbf{H}_p$ . The external field  $\mathbf{H}_{\text{ext}}(t)$  is varied on the surface of a sphere and hence the topology of our control space  $\mathcal{C}$  is that of a punctured sphere (certain bifurcation or fence points are removed from the sphere which renders the sphere not simply connected, see Fig. 1b and d). We perform periodic modulation loops  $\mathcal{L}_C$  of the external field in control space  $\mathcal{C}$  to drive the system. The external field is strong enough to cause the paramagnetic particles to assemble into a rod because of induced dipolar interactions between them. The two ends of the rod are the two feet of our self assembled biped. The dipolar interactions are stronger than the buoyancy of the biped causing the biped to align with the external field, which generically lifts one foot of the biped from the ground while the other foot remains on the ground. Note that the locking of the orientation of the biped to the external field with the continuous variation of the external field causes each foot to always keep its magnetic character, *i.e.* the northern foot located at  $\mathbf{r}_N$  being a magnetic north pole and the southern foot at  $\mathbf{r}_S$  being a south pole. The vector  $\mathbf{b} = \mathbf{r}_S - \mathbf{r}_N$  denotes the northern foot to southern foot vector of the biped. The locking of the biped orientation  $\mathbf{b}$  to the external field  $\mathbf{H}_{\text{ext}}$  allows to interchangeably use the sphere of biped orientations or the sphere of external field orientations as the control space. The southern foot will be on the ground when the external field points into the south of  $\mathcal{C}$ . The northern foot will be on the ground when the external field points into the north of  $\mathcal{C}$ . The transfer of support between the two feet occurs when the external field is within the tropics of  $\mathcal{C}$ .

The external magnetic field has negligible lateral gradients and the position of the biped is governed by the field gradients

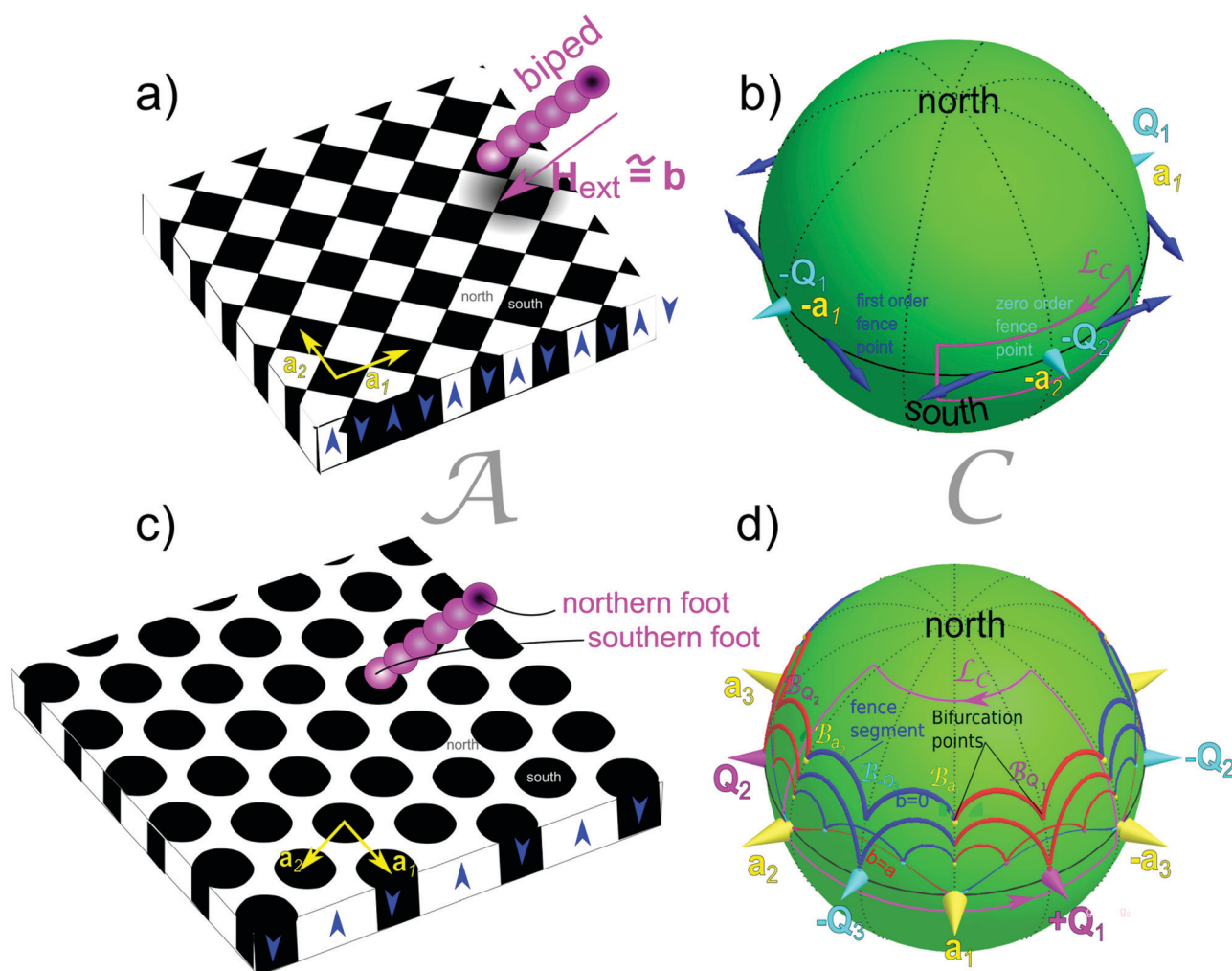


**Fig. 1** (a) Square ((c) hexagonal) magnetic pattern with up (white) and down (black) magnetized regions, characterized by the primitive unit vectors  $\mathbf{a}_i$  (yellow) and primitive reciprocal unit vectors  $\mathbf{Q}_i$  (magenta). Colloids (magenta) assemble into a rod that functions as a biped with feet at both ends. The biped walks across the pattern as we apply modulation loops of the external magnetic field. The external field and thus the orientation  $\mathbf{b}$  varies on the surface of a sphere (b and d). The walk depends on how the modulation loops in control space wind around the fence points (segments) in control space (b and d) that in general vary with the length  $b$  of the biped. We show a typical fundamental loop  $\mathcal{L}_C$  (purple) that causes different topologically protected transport for small and larger bipeds. Fence points for the square lattice in (b) are the points pierced by the cyan and blue arrows. For the hexagonal lattice in (d) segments of fence lines are depicted in red and blue and they meet in bifurcation points where the curvature of the fence diverges.

of the magnetic pattern. These gradients decay exponentially with the distance from the pattern. Therefore, the location of the walker is with the grounded foot sitting within a local minimum of the colloidal potential (a foothold). The transfer of support is accompanied by a release of the lifting foot from the minimum of the colloidal potential and a sliding of the touching down foot into a new minimum (foothold). Generically, the transfer of support will be associated with frustration as the length  $b = 2(n - 1)R$  of the biped will not match with the distance between consecutive minima.

## 4 Topological rolling transport of single spheres

Let us refer to the two-dimensional space the walker steps upon as action space  $\mathcal{A}$ . Special closed modulation loops in control

space  $\mathcal{C}$  induce open walks in action space  $\mathcal{A}$ . In ref. 24, 25 and 28 we demonstrated how the bulk rolling of single colloidal spheres (point particles) above magnetic lattices with different symmetries is topologically protected. We summarize here the main aspects of the sphere transport and refer the reader to ref. 24, 25 and 28 for a complete description. For each lattice symmetry there exist special fundamental modulation loops of  $\mathbf{H}_{\text{ext}}$  in  $\mathcal{C}$  that induce transport of colloids in  $\mathcal{A}$  by a primitive lattice vector  $\mathbf{a}_i$ . These fundamental loops share a common feature, they wind around special objects that lie in  $\mathcal{C}^{24,25,28}$  roughly in the direction of a primitive reciprocal unit vector perpendicular to the primitive lattice vector  $\mathbf{a}_i$  of the transport. A sphere does not walk because it is isotropic and has no foot. It adiabatically slides or rolls<sup>29</sup> on an externally controlled time scale and for very particular non trivial loops on a square lattice and in half of the non trivial loops on hexagonal lattice it irreversibly slides on a faster intrinsic time scale. The character

of the transport thus is that of a wheel rolling with slip between the wheel and the ground.

In the simplest case, a square lattice, the control space is characterized by just four zero order “fence” points on the equator lying along the directions of the primitive reciprocal lattice vectors,<sup>24</sup> see Fig. 1b. For a hexagonal lattice the objects are fence segments connecting bifurcation points in  $\mathcal{C}$ , see Fig. 1d. We call a modulation loop encircling one of these objects a fundamental loop  $\mathcal{L}_{Q_i}$ . Each of these fundamental loops induces adiabatic transport in the sense that a single colloidal particle follows a minimum of the colloidal potential at any time. Hence, the position of the particle in  $\mathcal{A}$  parametrically depends on the position of the external magnetic field in  $\mathcal{C}$ . All modulation loops discussed in what follows can be viewed as concatenations of fundamental loops. The motion of a sphere is an adiabatic motion if the loop is encircling the object without cutting through it.

## 5 Theory of adiabatic topological walks

Because the transport of a colloidal sphere is topological it is robust to perturbations. Mathematically the surface of a colloidal sphere is a manifold of genus  $g = 0$  and it is topologically equivalent to a biped. In theory we may continuously distort the shape of a sphere into that of a biped. In experiments this distortion is achieved by an assembly of a discrete number of spheres into a biped rod rather than by continuously distorting a colloidal particle. If the perturbation introduced by this change of shape is not too strong the result of a control loop must be the same no matter whether the object is a sphere or a biped. Longer bipeds fall into topological equivalence classes that are different from that of a point particle.

We may write the pattern magnetic field as<sup>24</sup>

$$\mathbf{H}_p = \nabla\psi \quad (1)$$

where

$$\psi(\mathbf{r}) \propto e^{-Qz} \sum_{n=1}^N \exp(i\mathbf{r}_A \cdot \mathbf{R}_N^n \cdot \mathbf{Q}_1) \quad (2)$$

is the magnetic potential and depends on the position  $\mathbf{r} = (\mathbf{r}_A, z)$  that we have split into a lateral vector  $\mathbf{r}_A$  in action space  $\mathcal{A}$  and the normal component  $z$ . Making use of the periodicity of the pattern, topologically action space is equivalent to a torus. A path leading from one unit cell to a neighboring unit cell becomes a path that winds around the torus once. The vector  $\mathbf{Q}_1$  denotes one of the  $N$  lowest non vanishing reciprocal lattice vectors of the 2D-lattice and  $Q = 2\pi/a$  its modulus. The lattice is invariant under a 2D rotation  $\mathbf{R}_N$  by the angle  $2\pi/N$  and the other  $N - 1$  equivalent reciprocal lattice vectors are obtained by successive rotations  $\mathbf{Q}_{n+1} = \mathbf{R}_N \cdot \mathbf{Q}_n$ . The projection of the pattern magnetic field onto the external field and averaged over the biped is the biped potential

$$V_{\text{biped}} \propto \psi(\mathbf{r}_S) - \psi(\mathbf{r}_N) \quad (3)$$

where  $\mathbf{r}_S$  and  $\mathbf{r}_N$  are the positions of the southern and the northern foot of the biped. The vector  $\mathbf{b} = \mathbf{r}_S - \mathbf{r}_N$  denotes the northern foot to southern foot vector of the biped. When the external magnetic field is strong compared to the pattern field the orientation  $\mathbf{b}$  is locked to the direction of the external field  $\mathbf{b} \parallel \mathbf{H}_{\text{ext}}$ . We may thus choose the vector space of  $\mathbf{b}$  as control space. In the limit  $b \ll a$  the biped potential reduces to a point particle potential

$$V_{\text{point}} \propto \mathbf{b} \cdot \mathbf{H}_p \propto \mathbf{H}_{\text{ext}} \cdot \mathbf{H}_p \quad (4)$$

### 5.1 Gauges

We have discussed the topological properties of  $V_{\text{point}}$  in ref. 24, 25 and 28.

We would like to write the position of both feet as a sum of an absolute position and a conformational position

$$\mathbf{r}_{S/N} = \mathbf{r}_{\text{abs}} + \mathbf{r}_{\text{con},S/N} \quad (5)$$

such that the conformation position after the period  $T$  of a closed fundamental control loop  $\mathcal{L}_C$  is restored

$$\mathbf{r}_{\text{conf},S/N}(T) = \mathbf{r}_{\text{con},S/N}(0) \quad (6)$$

and the translation  $\Delta\mathbf{r}_{\text{abs}} = \mathbf{a}_i$  by lattice vector over a period is blamed onto the absolute position  $\mathbf{r}_{\text{abs}}$ . The decomposition eqn (5) carries a gauge freedom. We will make use of two choices of gauge. The center gauge simply chooses the absolute position to be the center of the biped  $\mathbf{r} = \mathbf{r}_{\text{abs}} = (\mathbf{r}_S + \mathbf{r}_N)/2$  and the conformational coordinates as  $\mathbf{r}_{\text{con},S/N} = \pm\mathbf{b}/2$ . This choice of gauge is useful since it splits the position into a vector  $\mathbf{r} = (\mathbf{r}_A, z)$  in action space and a vector  $\mathbf{b}$  in control space. An alternative choice of the absolute position is the instantaneous center of rotation:

$$\mathbf{r}_{\text{Abs}} = \mathbf{r}_{\text{ICR}} \quad (7)$$

such that

$$d\mathbf{r}_{\text{ICR}} = d\mathbf{b} \cdot \nabla_{\mathbf{b}} \mathbf{r}_{\text{ICR}} = \mathbf{0} \quad (8)$$

exactly if

$$d\mathbf{b} \cdot \nabla_{\mathbf{b}} |\mathbf{r}_{\text{ICR}} - \mathbf{r}_S| = d\mathbf{b} \cdot \nabla_{\mathbf{b}} |\mathbf{r}_{\text{ICR}} - \mathbf{r}_N| = 0 \quad (9)$$

We call this gauge the walker gauge because eqn (9) will hold whenever the biped foot remains within a non moving foothold such that either  $\mathbf{r}_{\text{ICR}} = \mathbf{r}_S$  or  $\mathbf{r}_{\text{ICR}} = \mathbf{r}_N$ . Eqn (8) and (9) state that the edge  $\mathbf{r}_{\text{ICR}}$  of the triangle defined by  $\mathbf{r}_S$ ,  $\mathbf{r}_N$  and  $\mathbf{r}_{\text{ICR}}$  can only translate if the triangle changes its shape. In particular, the walker does not translate when one foot is grounded. The only translational motion of an ideal walker  $d\mathbf{r}_{\text{ICR,ideal}} = \mathbf{b}_{\text{transfer}} \delta(t - t_{\text{transfer}}) dt$  occurs when the instantaneous center of rotation longitudinally moves from one foot to the other by the momentary vector  $\mathbf{b}_{\text{transfer}}$  during the transfer of support. The walker gauge shows how essential is the lift of one foot from the non moving foothold and the grounding of the next foot for effective walking. The center of an ideal walker in contrast moves on a circle around the grounded foot while one of the feet is grounded. It does not move when the grounding is transferred between the feet. The motion of the biped center and the instantaneous center of

rotation for a general ideal or non ideal walker are quite different. Nevertheless, the motion of both points over a period is the same and thus gauge independent because of eqn (6). We decompose the motion of the instantaneous center of rotation into a longitudinal and transversal component.

We anticipate the longitudinal component of the motion as the autonomous walking component of the motion. The transversal component arises if a foothold is moving. This motion is a passive transport of the walker with the foothold. The walker gauge is useful to decompose the motion into walking and passive advection. Note, however, that the decomposition into walking and advection in contrast to the full motion is gauge dependent.

## 6 Adiabatic walks on square patterns

### 6.1 Walkers gauge

In Fig. 2a we show the driving loop  $\mathcal{L}_{-Q_2}^{-1}(\Delta\phi)$  in the control space  $\mathcal{C}$  of a square pattern. The loop clockwise circulates the

fence point of  $-Q_2$  direction with an azimuthal width of  $\Delta\phi$ . In Fig. 2b we plot simulated trajectories on square patterns of the southern (blue) and northern (red) foot together with the instantaneous center of rotation  $r_{ICR}$  that we color in green when the motion is longitudinal (along  $\mathbf{b}$ ), orange when it is transversal, and white when it is a mixture of longitudinal and transversal motion. Two trajectories are shown. One for a small biped of length  $b = 0.6a$  and one of a large biped of length  $b = 2.8a$ . The long biped longitudinally autonomously walks, while the smaller biped also shows some passive mixed sliding of the foothold (white part of the instantaneous center of rotation trajectory).

In Fig. 2c we plot experimental trajectories of the southern (blue) and the northern (red) foot of various bipeds assembled from colloidal spheres of radius  $R = 2.8 \mu\text{m}$  on a square pattern of lattice constant  $a = 7 \mu\text{m}$ . We also plot the trajectory instantaneous center of rotation (green). All bipeds are subject to the loop  $\mathcal{L}_{-Q_2}^{-1}(\Delta\phi)$  of width  $\Delta\phi = 65^\circ$ . A video clip of bipeds

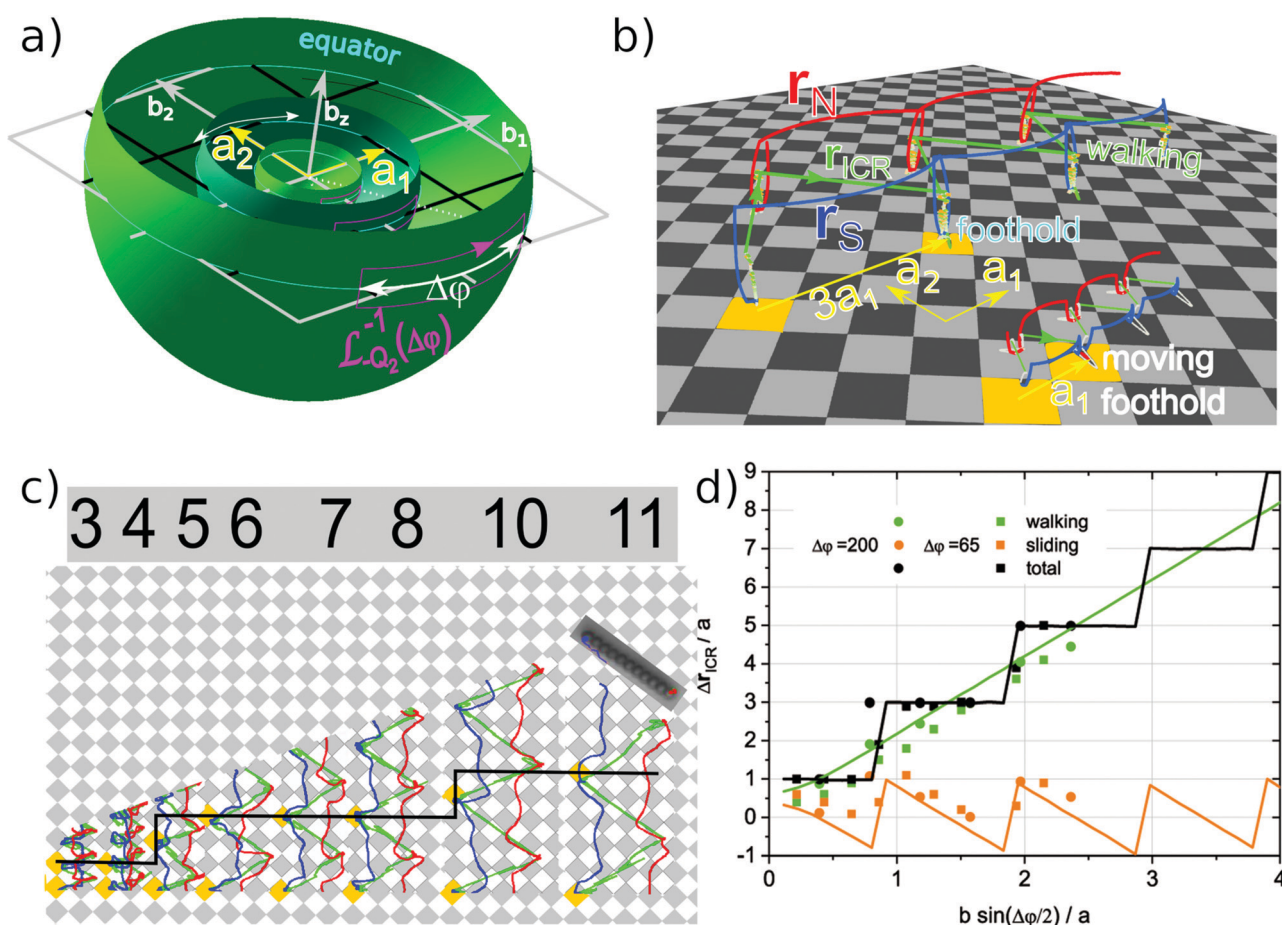


**Fig. 2** (a) Control spaces of bipeds of lengths  $b = 0.5a, 1.05a, 2.1a$  with a fundamental loop  $\mathcal{L}_{-Q_2}^{-1}(\Delta\phi)$  of width  $\Delta\phi = 70^\circ$ . Fence lines are drawn in gray and black. (b) Simulated trajectories of both feet (blue and red) and the instantaneous center of rotation  $r_{ICR}$  for a biped of length  $b = 0.6a$  and  $b = 2.8a$ . Longitudinal moves of the instantaneous center of rotation are shown in green, transversal moves in orange and mixed moves in white. (c) Experimental trajectories of the feet (blue and red) of bipeds assembled from 3–11 colloidal spheres of radius  $R = 2.8 \mu\text{m}$  on a square pattern of lattice constant  $a = 7 \mu\text{m}$  are shown together with the path of the instantaneous center of rotation (green). We also overlay a microscope images of the final biped position of the 11-particle biped. Two consecutive footholds of the southern foot for each walker are marked in orange. (d) Plot of the simulated and experimentally determined total, longitudinal and transversal displacement of the instantaneous center of rotation subject to the loop of width  $\Delta\phi = 70^\circ$  for the simulations and  $\Delta\phi = 65^\circ$  and  $\Delta\phi = 200^\circ$  for the experiments. Videoclips of bipeds subject to the same loop are shown in the Supplementary movie [adfigure2.mp4](#).

of different lengths subject to this loop are shown in the video clip [adfigure2.mp4](#). In Fig. 2c bipeds consisting of 3–11 colloidal particles are shown. Two consecutive footholds the southern foot steps upon are marked in orange to emphasize the step width of our walkers. We also overlay a microscope image of the final biped position for the 11-particle biped. The instantaneous center of rotation alternates between the southern and the northern foot. In Fig. 2d we plot the simulated and experimentally determined total, longitudinal and transversal displacement of the instantaneous center of rotation as a function of the length  $b$  of the biped. The displacement is shown for a loop of width  $\Delta\phi = 70^\circ$  for the simulations and  $\Delta\phi = 65^\circ$  and  $\Delta\phi = 200^\circ$  for the experiments. The total simulated displacement induced by the control loop is a primitive unit vector for small bipeds and increases by two lattice constants when the biped length times the sine of half the azimuthal loop width  $b_t \sin(\Delta\phi/2) = na$  is an integer multiple of the length of the unit vector. The experimental displacement shows similar behavior, however also even displacements are observed when  $b_t \sin(\Delta\phi/2)/a$  is close to an integer. Presumably this occurs because the control loop is not entirely symmetric around  $\mathbf{Q}_2$  such that the two higher order fences pass through the loop at slightly different biped sizes. Comparing the simulated and experimental total displacement we find excellent agreement.

We also depict the longitudinal and transversal displacement of the instantaneous center of rotation. The longitudinal displacement  $\Delta\mathbf{r}_l = \mathbf{a}_1 2b \sin(\Delta\phi/2)/a$  is proportional to the biped length  $b$  and increases continuously with the length of the biped. The transversal displacement does not exceed the length of a primitive unit vector  $\Delta\mathbf{r}_t = 2\mathbf{a}_1(b \sin(\Delta\phi/2)/a - \text{round}[b \sin(\Delta\phi/2)/a])$ . If we decompose the experimental displacement into longitudinal and transversal displacement we find the experimental longitudinal component to be systematically lower than the longitudinal component of the simulations. The experimental transversal component shows some trend to follow the discontinuous behavior of the transversal simulated component. We believe this relatively poor agreement to arise from the fact that in contrast to the total displacement the individual displacements are not topologically protected, but are susceptible to weak perturbations such as imperfections of the lithographic pattern, misalignments between the control loop and the pattern, and the deviation of the colloidal biped from an idealized paramagnetic line.

## 6.2 Center gauge

For a better understanding of the topology of the motion the center gauge is more useful and the potential in this gauge reads (see eqn (3)):

$$V_{\text{biped}} \propto (\psi(\mathbf{r} + \mathbf{b}/2)) - (\psi(\mathbf{r} - \mathbf{b}/2)) \quad (10)$$

with the biped centered at the position  $\mathbf{r}$ . The biped potential is periodic and invariant under the simultaneous transformation  $\mathbf{b} \rightarrow \mathbf{b} + \mathbf{a}$  and  $\mathbf{r} \rightarrow \mathbf{r} + \mathbf{a}/2$  where  $\mathbf{a}$  is a primitive lattice vector. The biped potential reverses sign  $V_{\text{biped}} \rightarrow -V_{\text{biped}}$  when one reverses the biped vector  $\mathbf{b} \rightarrow -\mathbf{b}$ . The fence is the set

$\mathcal{F} = \{(\mathbf{r}_A, \mathbf{b}) | \nabla_A V_{\text{biped}} = 0 \text{ and } \det(\nabla_A \nabla_A V_{\text{biped}} = 0)\}$ . Its projection into  $\mathcal{C}$  is the set  $\mathcal{F}_C = \{\mathbf{b} | (\mathbf{r}_A, \mathbf{b}) \in \mathcal{F} \text{ for some } \mathbf{r}_A\}$ .

In Fig. 2a we construct the projection of the fence onto the spherical control space of a biped of finite length  $b$  on a square pattern from that of a colloidal sphere (a point particle see ref. 24). For convenience we show the control space of a biped of length  $b$  as a sphere of radius  $b$ . Pieces of three such spheres are shown in Fig. 2a. As for point particles zero order fences lie along the  $b_1$  and  $b_2$  coordinates. Because the biped potential is periodic in  $\mathbf{b}$  with period  $\mathbf{a}$  these zero order fences repeat as higher order fences every lattice vector (gray and black lines in Fig. 2a). The minima near the black fences are displaced from the minima near the gray fences by half the lattice vector. For small bipeds  $b < a$  the control space is topologically equivalent to that of a point particle. Larger biped control spaces are cut also by higher order fences displaced from the origin and are therefore topologically different from small biped control spaces with more fence points on the equator. Each winding of a control loop around one of the fences adiabatically propels the biped by a unit vector perpendicular to the fence. The fundamental loop  $\mathcal{L}_{-\mathbf{Q}_2}^{-1}(\Delta\phi)$  in Fig. 2a winds clockwise around the central fence along the  $-b_2$  axes for all biped sizes but also around the black displaced fences parallel to the  $b_2$ -axes for the  $b = 2.1a$  bipeds. The  $b = 2.1a$  bipeds therefore are propelled three times as fast as the small bipeds. Much alike human beings bipeds with longer legs move faster than smaller bipeds. The increase in speed however happens in discrete steps as the speed is topologically enforced to be a multiple of a lattice vector per cycle.

The walker gauge may shed some light on what part of the motion is true walking and what part is sliding. In contrast to the gauge independent description in terms of winding numbers the decomposition into active and passive motion relies on a gauge and does not survive a gauge transformation.

## 7 Selective combinations of fundamental loops

The control space of the square lattice in Fig. 2a contains fence points at the positions

$$\phi_{\mathcal{F},n,m} = \arcsin \frac{na}{b} + m\frac{\pi}{2} \quad (11)$$

with  $m = 0, 1, 2, 3, \dots$  and  $n$  an integer. For bipeds larger than the lattice constant ( $b > a$ ) fundamental loops around these new  $n \neq 0$  fence points will not transport small bipeds, but only bipeds of the proper length. Moreover, the azimuthal position for the higher order fences depend on the biped length ( $\frac{d\phi_{\mathcal{F}}}{db} \neq 0$ ), allowing to adiabatically transport larger bipeds that fall into the appropriate length range. In Fig. 3a, we show the complex loops in control space that transport small bipeds into the  $-x$ -direction and bipeds consisting of four colloids of biped length  $b = (4 - 1)2R$  into the  $+x$ -direction. In Fig. 3b the four colloids are transported in the  $+y$ -direction perpendicular

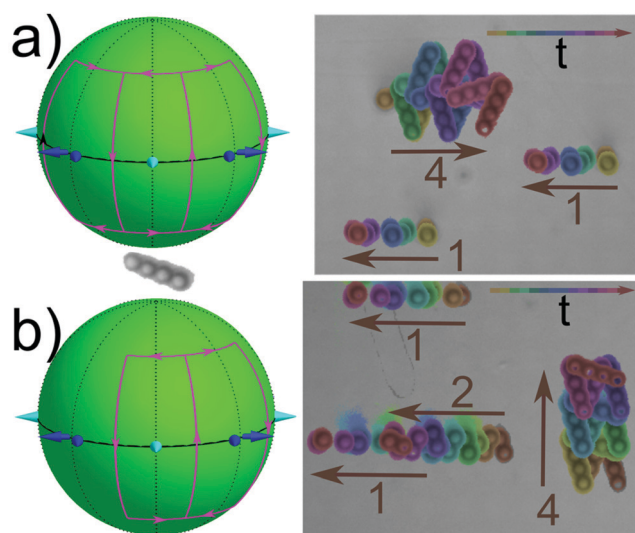


**Fig. 3** (a) Control space for a biped consisting of four colloids ( $b = (4 - 12R)$ ) together with a loop encircling the zero order  $y$ -fence in the positive and the 1st order  $x$ - and  $y$ -fences in the negative sense. Bipeds consisting of four colloids are transported in the  $+x$ -direction while single colloidal particles are transported in the  $-x$ -direction. We show an overlay of microscope images of the same bipeds at different times with the different times color coded from yellow toward red. (b) The same control space as in (A) subject to a loop encircling the zero order  $y$ -fence in the positive and the 1st order  $x$ - and  $y$ -fence in the negative sense. Bipeds consisting of four colloids are transported in the  $+y$ -direction while single colloidal particles and doublets are transported in the  $-x$ -direction. An overlay of microscope images of various bipeds is provided using the same color coding as in (A). Videoclips showing the complementary motion of different bipeds subject to the complex loops in this figure are shown in the Supplementary movie [adfigure3.mp4](#).

to the single colloid transport direction. A video clip showing the complementary motion of different bipeds subject to these complex loops are shown in the Supplementary movie [adfigure3.mp4](#). The longer the biped the more fence points exist in control space and the more directions of motion can be invoked by the proper combination of fundamental loops. A protocol how to exploit the fence pattern in a systematic way can be found in ref. 30.

## 8 Topological effects of hydrodynamic friction

The topological protection of the walker is based on the fact that the grounded foot of the walker remains within its local foothold as long as we do not approach the equator of control space where the transition of the foothold of the left toward the right foot occurs. For this the instantaneous center of rotation must remain with the grounded foot.

In a low Reynolds number fluid hydrodynamic friction opposes the rotation of a biped with the external field. The hydrodynamic friction of a rotating stick is minimal when the instantaneous center of rotation is centered in the biped rather than in one of its feet. Increasing the speed of the control loop

therefore causes competition for the instantaneous center of rotation between the biped center and the biped feet.

When the hydrodynamic forces exceed the pattern forces, which happens especially when the biped foot to foot vector endpoint is close to one of the fences, one may lose an integer number of steps per loop. The Mason number  $\mathcal{M} = \eta 2\pi f / \mu_0 \chi_{\text{eff}} \mathbf{H}_{\text{ext}} \mathbf{H}_p$  (with  $\eta$  the shear viscosity of the fluid and  $\chi_{\text{eff}}$  the effective magnetic susceptibility of a colloidal particle) is a dimensionless measure of the driving frequency  $f = T^{-1}$  of a loop. In Fig. 4a, we plot Brownian simulation data of the number of steps of a biped *versus* its effective length  $b \sin(\Delta\phi/2)/a$  and *versus* the dimensionless frequency  $\mathcal{M}(b/a)^{3/2}$ . The topological protection of an integer number of steps of the biped also holds when the driving is not adiabatic. However, the faster the driving the lower the number of biped steps per loop.

The experimental data in Fig. 4b shows odd and even steps and roughly follows the simulations. The lack of detailed

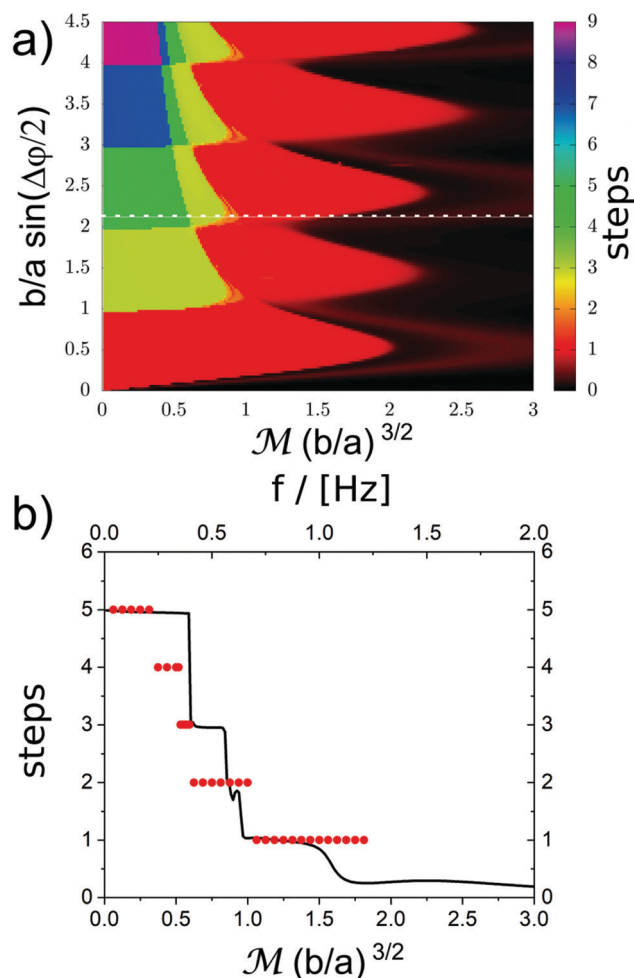


**Fig. 4** (a) Brownian dynamics simulations of the displacement of the biped as a function of the Mason number and the effective length of the biped. (b) The experimental data of a biped of length  $b/a \sin \Delta\phi/2 \approx 2.1$  *versus* the frequency of the driving (red circles) and the simulated data for the same effective length *versus* Mason number.

agreement may be easily understood as we have neglected the presence of the solid support as well as hydrodynamic interactions between the colloidal beads in the simulations. However, the topological locking to integer steps seems to be a robust feature of the dynamics also at higher frequencies.

## 9 Symmorphic hexagonal pattern

### 9.1 Control space

In Fig. 5a we plot the fence (red and blue) in the Wigner Seitz cell (cyan) of a hexagonal lattice as a function of  $\mathbf{b}$ . In theory we could in principle also change the length of the biped such that our control space is augmented by one dimension. In the experiments the biped length will be fixed and the control space is the cut of a sphere of radius  $b$  with this augmented control space. In Fig. 5a fence areas are bordered by bifurcation lines (yellow, magenta, and cyan) with the bifurcation lines meeting in topological transition points that are located in the center and at the corners of the Wigner Seitz cell. A cut of the periodically continued fence with a sphere of radius  $b$  constitutes the control space  $\mathcal{C}$  of a biped of fixed length  $b$ . In Fig. 5b we show the normalized spherical control spaces for ( $b = 0.33a, b_t = a/\sqrt{3}, 0.7a$ ) and  $b_t = a$ . If the fence segments of two bipeds can be continuously deformed into each other without changing the number of bifurcation points the bipeds exhibit equivalent transport behavior. The behavior of the bipeds changes at the topological transition lengths  $b_t = a\sqrt{(n^2 + nm + m^2)}/3$ , where  $n$  and  $m$  are integers.

If we project the bifurcation lines of Fig. 5a to the plane  $b_z = 0$  we obtain the projected fence lines in Fig. 5c. The yellow line segments between the topological transition points are along the lattice vectors and the magenta (cyan) segments are parallel to the positive (negative) reciprocal lattice vectors when folded into the Wigner Seitz cell. The cyan segments are anti parallel to the positive reciprocal lattice vectors. The circle of biped length  $b$  cuts through

these segments and the number  $N_a$  ( $N_Q$ ) of yellow (magenta or cyan) segments cut exactly once are the number of bifurcation points of type  $\mathcal{B}_a$  and  $\mathcal{B}_Q$  in the northern fence in Fig. 5b.

### 9.2 Stationary manifold

For a fixed length of the biped the stationary manifold  $\mathcal{M} = \{(\mathbf{r}_A, \mathbf{b}) | \nabla_{\mathcal{A}} V_{\text{biped}} = 0\} \subset \mathcal{C} \otimes \mathcal{A}$  can be shown to be a manifold of genus  $g = N_a + N_Q - 5$  that is cut into three pieces  $\mathcal{M}_+$  and  $\mathcal{M}_-$  of genus  $g_+ = g_- = (N_a - 2)/2$  and,  $\mathcal{M}_0$  of genus  $g_0 = N_Q - 3$ , where the stationary points are maxima, minima, respectively saddle points of the biped potential. The holes in  $\mathcal{C} \otimes \mathcal{A}$  and in  $\mathcal{M}$  are inherited from the holes of  $\mathcal{A}$  (a torus). A loop  $\mathcal{L}_{\mathcal{C}} \subset \mathcal{C}$  in control space has several preimage loops  $\mathcal{L}_{\mathcal{M}_i} \subset \mathcal{M}$ , ( $i = 1, 2, \dots, m$ ), ( $m = 4, 5$ , or  $6$ ) on  $\mathcal{M}$ . If one of these loops entirely lies in  $\mathcal{M}_-$  and winds around holes in  $\mathcal{M}_-$  the loop will be projected into action space as a minimum loop  $\mathcal{L}_{\mathcal{A}} \subset \mathcal{A}$  that winds around the torus and therefore adiabatically transports the biped. Fundamental loops in control space that enter and exit the region north of the fence *via* fence segments of the same color (red or blue) cause adiabatic transport. A preimage loop that winds around holes of  $\mathcal{M}_-$  but crosses over to  $\mathcal{M}_0$  also transports but in form of a ratchet. Fundamental loops in control space that enter and exit the region north of the fence *via* fence segments of different color cause ratchet transport. At fixed biped length  $b$  one form of adiabatic transport changes to another form of adiabatic transport only *via* an intervening ratchet. The adiabatic speed of a longer biped can be higher once we insert more bifurcation points of type  $\mathcal{B}_a$  into a fence in control space and this happens the first time for  $b > a$  beyond the lowest fence in Fig. 5b and c.

### 9.3 Response to loops in action space

The hexagonal pattern lacks a glide plane and the fence is no longer located at the equator but in the northern hemisphere, and the number of minima of the potential per unit cell of the

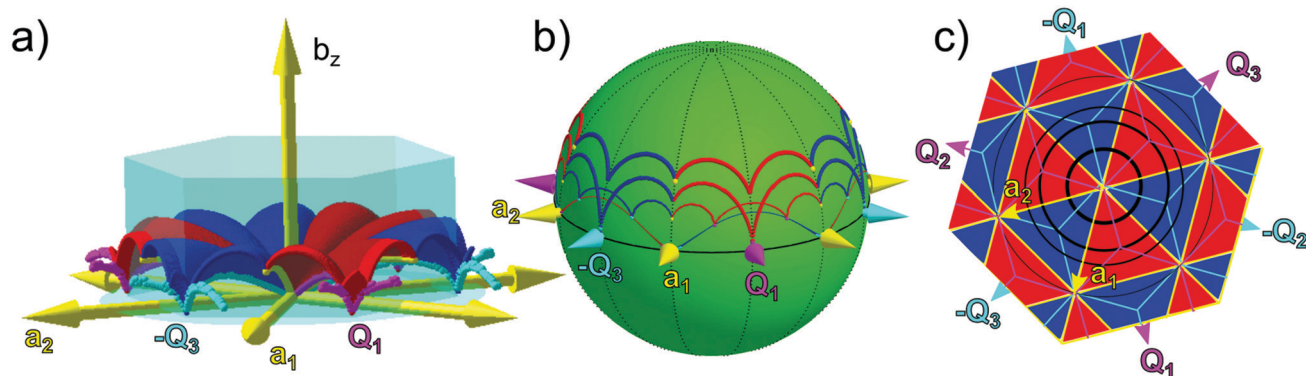


Fig. 5 (a) Fences (red and blue) within the Wigner Seitz cell (cyan) of a hexagonal lattice with unit vectors  $\mathbf{a}_1$  and  $\mathbf{a}_2$ . Bifurcation lines (yellow, cyan and magenta) are lines where the curvature of the fences diverges. The bifurcation lines meet at topological transition points located in the center and at the corners of the Wigner Seitz cell. (b) Fence segments and bifurcation points on the control space  $\mathcal{C}$  of the external field obtained from figure (a) by cutting the fence with a sphere of radius  $b = 0.33a$  (upper fence),  $b_t = a/\sqrt{3}$ ,  $b = 0.7a$ , and  $b_t = a$  (thinnest fence) and projecting it to a unit sphere. Topologically nontrivial loops must wind around one of the bifurcation points of the biped. There are modulation loops that circle around a bifurcation point of a biped of one but not the other length. (c) Projection of the bifurcation lines of figure (a) in an extended zone scheme onto the plane  $b_z = 0$  together with cuts (black) of the spheres from (b) with this plane. Topological transitions in the biped behavior occur when ever the radius moves across one of the topological transition points.

lattice differs depending on whether the external field is north or south of the fence. For this reason, even if we apply a loop that extends as much to the north as to the south of control space, the motion of the biped is a limping motion. We see this in Fig. 6 by the instantaneous center of rotation (green) meeting the southern (blue) foot within a southern foothold (bubble) and the northern (red) foot within one of the two (white) interstitials between three bubbles. When the motion is adiabatic the northern foothold can hold the northern foot at its location while we exit the region of control space north of the fence. In contrast, for a ratchet the northern foot of the biped prior to crossing the fence is in a vanishing foothold and therefore irreversibly jumps to the remaining foothold in the other interstitial when we exit the northern region. Simultaneously the southern foot jumps above the southern foothold (bubble). During the jump the orientation of the biped is fixed and therefore the instantaneous center of rotation moves away from the northern foothold far above the magnetic pattern before it returns to the northern foot after the jump. The northern foot stays with the remaining northern foothold only for the short period of the loop from the fence to the equator. The southern foot touches down to the southern foothold when we cross the equator, and the adiabatic propulsion caused by the northern segment of the loop in control space is booked in the walker gauge by a transfer of the instantaneous center of rotation from the northern to the southern foot. In Fig. 6a we show the control space of a biped of length  $b = 1.4a$  with 36 red and blue fence segments north of the equator. A symmetric loop around  $-Q_3$  enters and exits the north of control

space *via* a red fence segment and thus causes an adiabatic walk simulated with Brownian dynamics to the right of Fig. 6b. A different asymmetric loop in Fig. 6a enters the north of  $C$  *via* a blue segment and exits *via* the same red fence segment as the symmetric loop. Upon entry the northern foot resides in a foothold that vanishes upon exit through the red fence and therefore jumps to the remaining foothold, *i.e.* the remaining foothold in which the southern foot of the adiabatic loop had stayed in through the entire northern part of the adiabatic loop. The net motion is  $-2a_3$  for the symmetric loop and  $-a_2 - a_3$  for the asymmetric loop.

In Fig. 6c we show the experimental trajectories of two bipeds of length  $b = 1.2a$  subject to an asymmetric and a symmetric loop, the first performing a ratchet motion, the second an adiabatic motion. Ratchet jumps are visible as a motion of higher speed, with both feet making parallel displacements such that the relative orientation of the feet remain the same. Note that the adiabatic trajectories are mirror symmetric such that it is not possible to tell the direction of the motion from the trajectories. The ratchet trajectories in contrast are chiral and the direction of the motion can be told from this chirality. The direction is with the southern foot jumping into the bubble not out of the bubble. Similarly, the direction can be inferred from the northern foot jumping from the foothold that is the center of curvature of the arc segment of the southern foot toward the foothold that is not a center of curvature of an arc segment of the southern foot. In the video clip `adfigure6.mp4` the motion of the two experimental bipeds can be followed in full detail. The computation of the

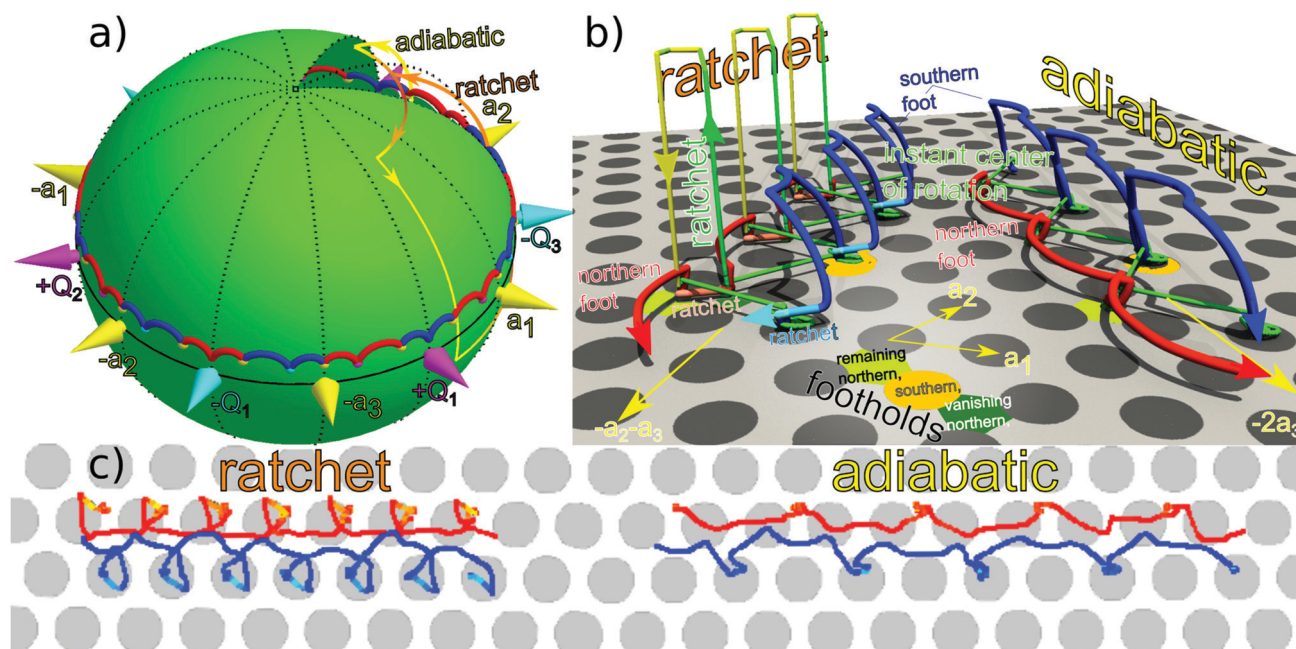


Fig. 6 (a) Control space and fence of a biped of length  $b = 1.4a$  with an asymmetric control loop causing a ratchet and a symmetric control loop causing adiabatic transport. (b) Simulated trajectories of the northern and southern foot and the instantaneous center of rotation of the same biped for the asymmetric and for the symmetric loop. In the ratchet trajectories brighter colors of the trajectories label the regions of higher speed when the ratchet jumps occur. (c) Experimentally measured ratchet and adiabatic trajectories of the feet of the bipeds of lengths  $b = 1.2a$  and  $b = 1.2a$  respectively. The trajectories are colored with brighter colors where the velocity is higher. Videoclips of the two experimental bipeds are shown in the Supplementary movie `adfigure6.mp4`.

instantaneous center of rotation from the motion of the two feet is rather sensitive to noise in the measurements and led to results dominated by the noise for these experiments. We do not show the instantaneous centers of rotation of the two experiments for this reason.

## 10 Discussion

The bipeds studied in this work are rigid bipeds having no joints. For these bipeds it is straight forward to compute the winding numbers of the driving loops in control space. Some of the objects one winds around are fixed and do not move with the size of the biped. Higher order objects arising from the periodicity of the problem as a function of the biped vector  $\mathbf{b}$  move in control space as the length of the biped grows. Part of the motion is therefore topologically protected independently of the size, others only beyond a certain size and only if one adapts the modulation loop to the increasing size.

Robotic bipeds have joints and other internal degrees of freedom of the conformation of a biped. Which of our findings of this work remain true when dealing with colloidal bipeds that have joints? The answer of course is that everything remains topologically protected if the conformation of a biped with joints does not deviate too strong from that of a rigid rod. In Fig. 7 and in the Supplementary movie [adfigure7.mp4](#) we show the motion of a colloidal biped on a square lattice that is deformed by viscous and magnetic stress<sup>31</sup> by a loop enclosing the vicinity of the equator. The shape of the biped at large Mason number alternates between an S-shaped conformation (stage 6 in Fig. 7) and its chiral mirror image (stage 4 in Fig. 7).

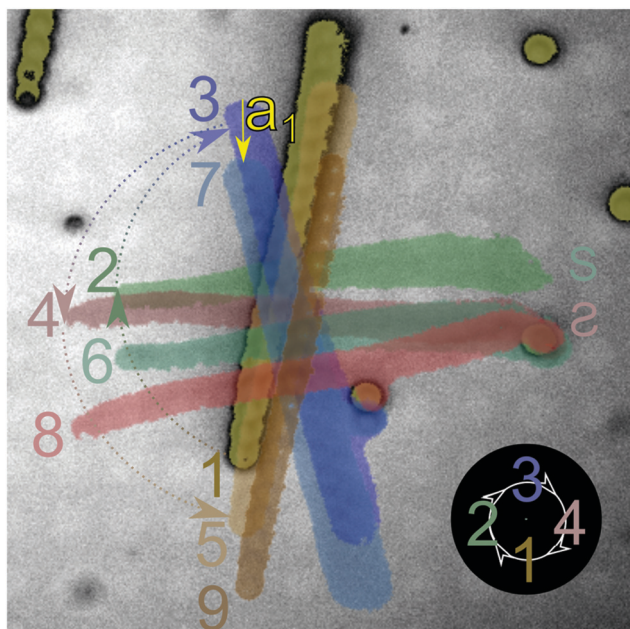


Fig. 7 Overlay of nine microscope images of a shape changing flexible colloidal rod at different times of the driving loop. The shape changing rod performs a topologically protected non-adiabatic walk on the pattern. A videoclip of the biped is shown in the Supplementary movie [adfigure7.mp4](#).

The same biped returns to a straight rod shape as the external field direction moves along the longitudinal sections of the loop. The non-adiabatic walking motion of these bipeds remains locked to a unit vector of the lattice, which proves that also flexible bipeds are topologically protected.

Once the flexibility of a biped becomes substantial we expect them to morph into magnetic filaments the propulsion of which has been studied in great detail.<sup>32–38</sup> The propulsion of magnetic filaments and bipeds are similar as they both are examples of geometric motion, *i.e.* a motion, where the global displacement only depends on the conformational path of the filaments or bipeds and not on the speed with which the conformational path is taken. Apart from these similarities the process of motion of filaments starkly differs from the motion of bipeds. For a filament to swim one must attach it to a larger particle that breaks the mirror symmetry between the two ends. A mirror symmetric filament would not be able to swim in a bulk low-Reynolds number liquid. Our bipeds are mirror symmetric and they can only walk by interacting with the magnetic pattern to which they intermittently bind but then detach. In the case of filaments the propulsion is a geometric propulsion which is not topological. If one perturbs the driving magnetic field the motion of the filament deviates from the original path, while in our topological system a small perturbation of the driving magnetic field perturbs the path of the motion but not the total displacement after completion of the closed but perturbed modulation loop.

It is not important whether the particles are paramagnetic or ferromagnetic since only the direction of the external magnetic field not its magnitude enters into the topology of the biped potential. We have not tried ferromagnetic colloids, but we anticipate them to behave in the same way, if we could keep them in a biped-shape and prevent the formation of closed rings.

A decrease of the scale will render thermal fluctuations more important and will broaden the bifurcation points into local regions that must be avoided in control space for the transport to remain robust. The robust biped motion control might be relevant for lab-on-the-chip applications.

## 11 Conclusions

The adiabatic walking step width of self assembled paramagnetic colloidal rods on a periodic magnetic lattice is topologically locked to be commensurate with the magnetic lattice. For this reason driving loops can be classified by winding numbers around fences (bifurcation points with fence segments) in control space. The walking is robust against a variety of static, adiabatic, and dynamic perturbations of the system. While the description of the absolute motion of the biped is gauge invariant, the decomposition into an active and a passive motion is gauge dependent.

## Author contributions

MMK, AdE, DdlH, & TMF designed and performed the experiment, and wrote the manuscript with input from all the other

authors. MU & FS produced the magnetic film. AT, RH, IK, ArE & DH performed the fabrication of the micromagnetic domain patterns within the magnetic thin film.

## Conflicts of interest

There are no conflicts to declare.

## Appendix

We use Brownian dynamics to simulate the motion of the bipeds on top of the magnetic pattern. Each biped consists of  $N$  particles where each particle sees the magnetic potential

$$V(\mathbf{x}_A, \mathbf{H}_{\text{ext}}(t), z) \propto -\mathbf{H}_{\text{ext}}(t) \cdot \mathbf{H}_p(\mathbf{x}_A) e^{-(z-z_0)\frac{2\pi}{a}}, \quad (12)$$

where  $\mathbf{H}_{\text{ext}}(t)$  is the external field at time  $t$ ,  $\mathbf{H}_p(\mathbf{x}_A)$  is the magnetic field created by the pattern at a fixed height  $z_0$  above the pattern at the position of the particle position  $\mathbf{x}_A$  in action space  $\mathcal{A}$  and  $z$  is the distance of the particle from the pattern. The equation of motion is then given by

$$\zeta \dot{\mathbf{x}}_A(t) = -\nabla_{\mathcal{A}} V(\mathbf{x}_A, \mathbf{H}_{\text{ext}}(t), z) + \eta(t), \quad (13)$$

where  $\zeta$  is the friction coefficient and  $\eta$  is a Gaussian random force with a variance given by the fluctuation–dissipation theorem. We use a constant value of  $\zeta$  which neglects all hydrodynamic interactions between the particles. The equation is then integrated in time  $t$  with a standard Euler algorithm. To restore the rigid shape of the biped and the enslavement of the orientation  $\mathbf{b}$  to the external magnetic field  $\mathbf{H}_{\text{ext}}(t)$ , after every simulation step the center  $\mathbf{x}_c$  of the biped is determined by the mean position of all particles

$$\mathbf{x}_c(t) = \frac{1}{N} \sum_{i=1}^N \mathbf{x}_i(t) \quad (14)$$

and its direction  $\mathbf{b}$  by the direction of the external field  $\mathbf{H}_{\text{ext}}$ . The new position for every particle is calculated as

$$\mathbf{x}_i(t) = \mathbf{x}_c(t) + (2i - (N + 1)) \frac{R}{\mathbf{H}_{\text{ext}}} \cdot \mathbf{H}_{\text{ext}}(t), \quad (15)$$

$$i = 1, \dots, N.$$

The particles are then shifted the same amount along an axis perpendicular to the pattern such that the lowest particle has the distance  $z_0$  from the pattern. We use a time step  $dt$  in the range from  $\frac{T}{dt} \approx 2 \times 10^4$  to  $2 \times 10^5$ , where the period  $T$  is proportional to the arc length  $S$  of the modulation loop in control space  $\mathcal{C}$ .

## Acknowledgements

This work is funded by the Deutsche Forschungsgemeinschaft (DFG, German Research Foundation) under project number 440764520. M. U. and F. S. acknowledge support from the Polish National Agency for Academic Exchange under grant number PPN/BDE/2019/1/00014/U/00001.

## References

- 1 D. Jongenee, R. Withagen, R. Withagen and F. T. J. M. Zaal, Do children create standardized playgrounds? A study on the gap-crossing affordances of jumping stones, *J. Environ. Psychol.*, 2016, **44**, 45–52.
- 2 A. Yildiz, M. Tomishige, R. D. Vale and P. R. Selvin, Kinesin walks hand-over-hand, *Science*, 2004, **303**, 676–678.
- 3 C. L. Asbury, Kinesin: world's tiniest biped, *Curr. Opin. Cell Biol.*, 2005, **17**, 89–97.
- 4 M. L. Shik and G. N. Orlovsky, Neurophysiology of locomotor automatism, *Physiol. Rev.*, 1976, **56**, 465–501.
- 5 D. Hamacher, F. Herold, P. Wiegel, D. Hamacher and L. Schega, Brain activity during walking: A systematic review, *Neurosci. Biobehav. Rev.*, 2015, **57**, 310–327.
- 6 P. Holmes, R. J. Full, D. Koditschek and J. Guckenheimer, The Dynamics of Legged Locomotion: Models, Analyses, and Challenges, *SIAM Rev.*, 2006, **48**, 207–304.
- 7 W. B. Sherman and N. C. Seeman, A Precisely Controlled DNA Bipod Walking Device, *Nano Lett.*, 2004, **4**, 1203–1207.
- 8 A. Shapere and F. Wilczek, Geometry of self-propulsion at low Reynolds number, *J. Fluid Mech.*, 1989, **198**, 557–585.
- 9 A. Shapere and F. Wilczek, Efficiency of self-propulsion at low Reynolds number, *J. Fluid Mech.*, 1989, **198**, 587–599.
- 10 Q. Nguyen, H. Ayonga, G. W. Jessy, A. D. Aaron and S. Koushil, 3D Dynamic Walking on Stepping Stones with Control Barrier Functions 2016 IEEE 55TH CONFERENCE ON DECISION AND CONTROL (CDC), IEEE Conference on Decision and Control, 2016, pp. 827–834.
- 11 M. Z. Hasan and C. L. Kane, Colloquium: Topological insulators, *Rev. Mod. Phys.*, 2010, **82**, 3045–3067.
- 12 S.-Q. Shen, *Topological insulators: Dirac equation in condensed matters*, Springer Science, and Business Media, 2013.
- 13 M. C. Rechtsman, J. M. Zeuner, Y. Plotnik, Y. Lumer, D. Podolsky, F. Dreisow, S. Nolte, M. Segev and A. Szameit, Photonic Floquet topological insulators, *Nature*, 2013, **496**, 196–200.
- 14 M. Xiao, G. Ma, Z. Yang, P. Sheng, Z. Q. Zhang and C. T. Chan, Geometric phase and band inversion in periodic acoustic systems, *Nat. Phys.*, 2015, **11**, 240–244.
- 15 A. Murugan and S. Vaikuntanathan, Topologically protected modes in non-equilibrium stochastic systems, *Nat. Commun.*, 2017, **8**, 13881.
- 16 A. M. E. B. Rossi, J. Bugase and Th. M. Fischer, Macroscopic Floquet topological crystalline steel and superconductor pump, *Europhys. Lett.*, 2017, **119**, 40001.
- 17 C. L. Kane and T. C. Lubensky, Topological boundary modes in isostatic lattices, *Nat. Phys.*, 2014, **10**, 39–45.
- 18 J. Paulose, B. G. Chen and V. Vitelli, Topological modes bound to dislocations in mechanical metamaterials, *Nat. Phys.*, 2015, **11**, 153–156.
- 19 L. M. Nash, D. Kleckner, A. Read, V. Vitelli, A. M. Turner and W. T. M. Irvine, Topological mechanics of gyroscopic metamaterials, *Proc. Natl. Acad. Sci. U. S. A.*, 2015, **112**, 14495–14500.
- 20 S. D. Huber, Topological mechanics, *Nat. Phys.*, 2016, **12**, 621–623.

- 21 M. J. Rice and E. J. Mele, Elementary Excitations of a Linearly Conjugated Diatomic Polymer, *Phys. Rev. Lett.*, 1982, **49**, 1455–1459.
- 22 B. I. Halperin, Quantized Hall conductance, current-carrying edge states, and the existence of extended states in a two-dimensional disordered potential, *Phys. Rev. B: Condens. Matter Mater. Phys.*, 1982, **25**, 2185–2190.
- 23 M. S. Rudner, N. H. Lindner, E. Berg and M. Levin, Anomalous Edge States and the Bulk-Edge Correspondence for Periodically Driven Two-Dimensional Systems, *Phys. Rev. X*, 2013, **3**, 031005.
- 24 D. de las Heras, J. Loehr, M. Lönne and Th. M. Fischer, Topologically protected colloidal transport above a square magnetic lattice, *New J. Phys.*, 2016, **18**, 105009.
- 25 J. Loehr, D. de las Heras, M. Lönne, J. Bugase, A. Jarosz, M. Urbaniak, F. Stobiecki, A. Tomita, R. Huhnstock, I. Koch, A. Ehresmann, D. Holzinger and Th. M. Fischer, Lattice symmetries and the topologically protected transport of colloidal particles, *Soft Matter*, 2017, **13**, 5044–5075.
- 26 C. Chappert, H. Bernas, J. Ferré, V. Kottler, J.-P. Jamet, Y. Chen, E. Cambril, T. De-Volder, F. Rousseaux, V. Mathet and H. Launois, Planar patterned magnetic media obtained by ion irradiation, *Science*, 1998, **280**, 1919–1922.
- 27 P. Kuświk, A. Ehresmann, M. Tekielak, B. Szymański, I. Sveklo, P. Mazalski, D. Engel, J. Kisielewski, D. Lengemann, M. Urbaniak, C. Schmidt, A. Maziewski and F. Stobiecki, Colloidal domain lithography for regularly arranged artificial magnetic out-of-plane monodomains in Au/Co/Au layers, *Nanotechnology*, 2011, **22**, 095302.
- 28 J. Loehr, M. Lönne, A. Ernst, D. de las Heras and Th. M. Fischer, Topological protection of multiparticle dissipative transport, *Nat. Commun.*, 2016, **7**, 11745.
- 29 D. Harland and N. S. Manton, Rolling Skyrmions and the nuclear spin-orbit force, *Nucl. Phys. B*, 2018, **935**, 210–241.
- 30 M. Mirzaee-Kakhki, A. Ernst, D. de las Heras, M. Urbaniak, F. Stobiecki, J. Gördes, M. Reginka, A. Ehresmann and Th. M. Fischer, Simultaneous polydirectional transport of colloidal bipeds, *Nat. Commun.*, 2020, **11**, 4670.
- 31 S. Melle and J. E. Martin, Chain model of a magnetorheological suspension in a rotating field, *J. Chem. Phys.*, 2003, **118**, 9875–9881.
- 32 C. Goubault, P. Jop, M. Fermigier, J. Baudry, E. Bertrand and J. Bibette, Flexible Magnetic Filaments as Micromechanical Sensors, *Phys. Rev. Lett.*, 2003, **91**, 260802.
- 33 R. Dreyfus, J. Baudry, M. L. Roper, M. Fermigier, H. A. Stone and J. Bibette, Microscopic artificial swimmers, *Nature*, 2005, **437**, 862–865.
- 34 M. Roper, R. Dreyfus, J. Baudry, M. Fermigier, J. Bibette and H. A. Stone, On the dynamics of magnetically driven elastic filaments, *J. Fluid Mech.*, 2006, **554**, 167–190.
- 35 K. Ērglis, R. Livanovičs and A. Cēbers, Three dimensional dynamics of ferromagnetic swimmer, *J. Magn. Magn. Mater.*, 2011, **323**, 1278–1282.
- 36 A. Cēbers and K. Ērglis, Flexible Magnetic Filaments and their Application, *Adv. Funct. Mater.*, 2016, **26**, 3783–3795.
- 37 J. Wei, F. Song and J. Dobnikar, Assembly of Superparamagnetic Filaments in External Field, *Langmuir*, 2016, **32**, 9321–9328.
- 38 A. Zaben, G. Kitenbergs and A. Cēbers, 3D motion of flexible ferromagnetic filaments under a rotating magnetic field, *Soft Matter*, 2020, **16**, 4477–4483.

# Publication 5

---

## Colloidal trains

*Soft Matter* **16**, 1594-1598 (2020)

Mahla Mirzaee-Kakhki,<sup>a1</sup> **Adrian Ernst**,<sup>a1</sup>  
Daniel de las Heras,<sup>a2</sup> Maciej Urbaniak,<sup>b</sup>  
Feliks Stobiecki,<sup>b</sup> Andreea Tomita,<sup>c</sup> Rico Huhnstock,<sup>c</sup>  
Iris Koch,<sup>c</sup> Jendrik Gördes,<sup>c</sup> Arno Ehresmann,<sup>c</sup>  
Dennis Holzinger,<sup>c</sup> Meike Reginka,<sup>c</sup> &  
Thomas M. Fischer<sup>a1</sup>

<sup>a1</sup> Experimental Physics X and <sup>a2</sup> Theoretical Physics II, Department of Physics, University of Bayreuth, 95447 Bayreuth, Germany.

<sup>b</sup> Institute of Molecular Physics, Polish Academy of Sciences, 60-179 Poznań, Poland.

<sup>c</sup> Institute of Physics and Center for Interdisciplinary Nanostructure Science and Technology (CINSA-T), University of Kassel, 34132 Kassel, Germany.

---

## My Contribution

Mahla Mirzaee-Kakhki performed the experiments. I worked out the computer control and simulations of the experiments. Daniel de las Heras supervised the simulations and Thomas Fischer the experiments. The authors from Poznań grew the magnetic films and the authors from Kassel Helium bombarded them to create the magnetic patterns. The preparation and writing of the paper was done by all authors.





Cite this: *Soft Matter*, 2020,  
16, 1594

Received 15th November 2019,  
Accepted 8th January 2020

DOI: 10.1039/c9sm02261a

rsc.li/soft-matter-journal

## Colloidal trains†

Mahla Mirzaee-Kakhki,<sup>a</sup> Adrian Ernst,<sup>a</sup> Daniel de las Heras,<sup>ib</sup> Maciej Urbaniak,<sup>ib</sup> Feliks Stobiecki,<sup>ib</sup> Andreea Tomita,<sup>ib</sup> Rico Huhnstock,<sup>d</sup> Iris Koch,<sup>d</sup> Jendrik Gördes,<sup>d</sup> Arno Ehresmann,<sup>ib</sup> Dennis Holzinger,<sup>ib</sup> Meike Reginka<sup>d</sup> and Thomas M. Fischer<sup>ib</sup>\*<sup>a</sup>

Single and double paramagnetic colloidal particles are placed above a magnetic square pattern and are driven with an external magnetic field processing around a high symmetry direction of the pattern. The external magnetic field and that of the pattern confine the colloids into lanes parallel to a lattice vector of the pattern. The precession of the external field causes traveling minima of the magnetic potential along the direction of the lanes. At sufficiently high frequencies of modulation, only the doublets respond to the external field and move in direction of the traveling minima along the lanes, while the single colloids cannot follow and remain static. We show how the doublets can induce a coordinated motion of the single colloids building colloidal trains made of a chain of several single colloids transported by doublets.

## 1 Introduction

Biomimetics is used to implement biological functions to artificial devices, fulfilling tasks in a non biological environment. Well known examples are artificial swimmers<sup>1–3</sup> and active systems<sup>4</sup> that can be used to *e.g.* transport a load. Microscopic dynamics can also be inspired by large scale transport systems such as trains. A railroad train is powered either by a separate locomotive or by multiple units of self propelled equally powered carriages. In nature the motility of family members of animals trailing behind each other is neither concentrated in the animal heading the trail nor is it distributed equally amongst family members. Young goslings trailing behind one of their parents need less but not zero power to follow their more powerful mother goose.<sup>5</sup> When elephants travel they walk in a line placing their youngest in between the grownups with a grownup at the head and at the tail. In the spirit of other bioinspired magnetic colloidal dynamics<sup>1–3,6,7</sup> we generate a biomimetic train of a collective ensemble of paramagnetic colloids. Single colloids are too weak to move on their own along the line and must be assisted to move by

pushing of the train with a larger paramagnetic colloidal doublet. The train is confined to an effectively one dimensional lane created *via* a colloidal potential which is generated by the combination of a magnetic square pattern and an external magnetic field. The power of each unit in the train is generated by modulating the external field on a control loop. Colloidal trains can only move above a square lattice if a sufficiently flat potential valley is created by orienting the external field roughly in direction of a primitive unit vector of the square magnetic pattern.

In contrast to other magnetically actuated motions that are either coupled *via* elastic bonds<sup>1</sup> or consist of particles in intimate contact<sup>2–4,6,7</sup> our particles are well separated individuals that can couple and decouple from the colloidal train and thus switch between individual and collective behavior.

## 2 Setup

We illustrate the doublet assisted motion of a train of single colloids using a square magnetic lattice,<sup>8,9</sup> Fig. 1(a). In the experiments, single paramagnetic colloidal particles or doublets of particles move on a plane above a thin Co/Au layered system with perpendicular magnetic anisotropy lithographically patterned *via* ion bombardment.<sup>9–11</sup> The pattern is a square lattice of magnetized domains with a mesoscopic pattern lattice constant  $a \approx 7 \mu\text{m}$ , see a sketch in Fig. 1(a). The pattern is magnetized in the  $\pm z$ -direction, normal to the film. The pattern is spin coated with a 1.6  $\mu\text{m}$  polymer film that serves as a spacer between the pattern and the colloids. The paramagnetic colloidal

<sup>a</sup> *Experimentalphysik X, Physikalisches Institut, Universität Bayreuth, D-95440 Bayreuth, Germany. E-mail: Thomas.Fischer@uni-bayreuth.de*

<sup>b</sup> *Theoretische Physik II, Physikalisches Institut, Universität Bayreuth, D-95440 Bayreuth, Germany*

<sup>c</sup> *Institute of Molecular Physics, Polish Academy of Sciences, 60-179 Poznań, Poland*

<sup>d</sup> *Institute of Physics and Center for Interdisciplinary Nanostructure Science and Technology (CINSaT), University of Kassel, D-34132 Kassel, Germany*

† Electronic supplementary information (ESI) available. See DOI: 10.1039/c9sm02261a

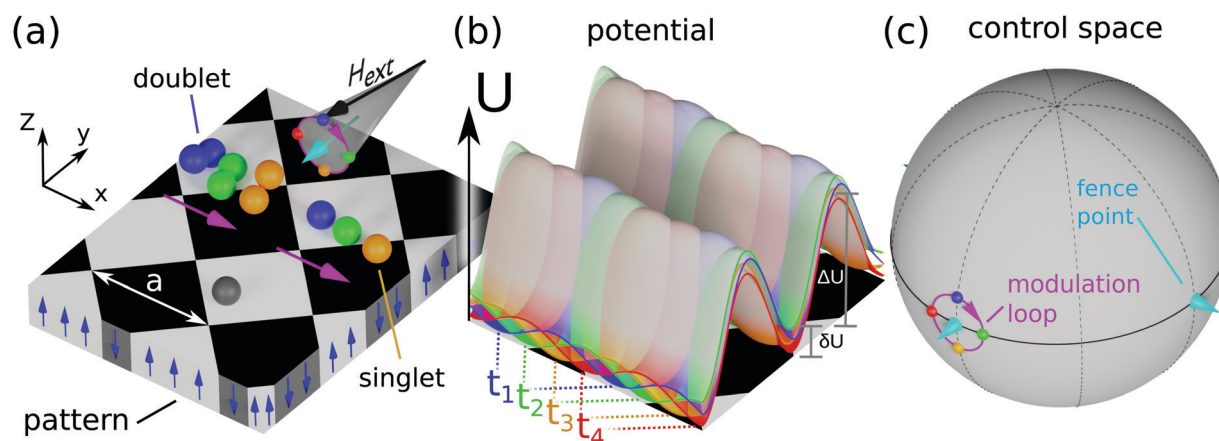


**Fig. 1** Schematic of the setup. (a) Single and double spherical colloidal particles are placed on top of a lithographic magnetic square pattern (lattice constant  $a \approx 7 \mu\text{m}$ ) of up (white) and down (black) magnetized domains along the  $z$ -axis. An isolated single colloid (gray) does not move at the modulation frequency applied in the experiments. Doublets are able to respond to the external field and can also induce motion of single colloids. The color (blue, green, and orange) of the doublet and of the singlet represents the position at three different times ( $t_1, t_2$ , and  $t_3$ ) during the modulation loop. (b) Magnetic potential  $U$  created by the pattern and the external potential for four different times ( $t_i, i = 1, 2, 3, 4$ ) during one modulation loop (red, blue, green, and orange) of the external field. The ratio between the large and the small barriers of the potential is  $\Delta U/\delta U \approx 10$ . (c) Each point in control space  $\mathcal{C}$  (gray sphere) corresponds to a different orientation of the external field. The experimental modulation loop is highlighted in purple. The loop winds around a fence point (cyan) of control space. The colors of the four potentials in (b) and the coloring of the moving colloidal positions (a) correspond to the four colored points on the loop in control space.

particles (diameter  $2.8 \mu\text{m}$ ) are immersed in water. A uniform time-dependent external magnetic field  $\mathbf{H}_{\text{ext}}$  of constant magnitude ( $H_{\text{ext}} = 4 \text{ kA m}^{-1}$ ) is superimposed to the non-uniform and time-independent magnetic field generated by the pattern  $\mathbf{H}_{\text{p}}$  ( $H_{\text{p}} \approx 1 \text{ kA m}^{-1}$ ). The external field is strong enough such that some of the paramagnetic particles self-assemble into doublets due to induced dipolar interactions between the single colloidal particles. The doublets then align with the direction of the external field. Our control space  $\mathcal{C}$  is the surface of a sphere that represents all possible orientations of the external field. We vary the external field  $\mathbf{H}_{\text{ext}}(t)$  with time  $t$  performing periodic closed modulation loops in  $\mathcal{C}$ .

Both  $\mathbf{H}_{\text{p}}$  and  $\mathbf{H}_{\text{ext}}$  create a potential  $U \propto -\mathbf{H}_{\text{ext}} \cdot \mathbf{H}_{\text{p}}$ . The potential is a periodic function of the position of the colloids in the magnetic lattice and it depends parametrically on the orientation of the external field in control space  $\mathcal{C}$ . At every time during the modulation loop, the colloids are attracted toward the minima of the potential. Full details about the computation of  $U$  and the motion of single colloids are given in ref. 8 and 9. Here, we briefly explain the points relevant to the present study. For a square lattice, there exist four special points (fence points) in  $\mathcal{C}$ . The four points represent four directions of  $\mathbf{H}_{\text{ext}}$  which are parallel and antiparallel to the lattice vectors of the square pattern. If the modulation loop of  $\mathbf{H}_{\text{ext}}$  in  $\mathcal{C}$  winds around one of the fence points, then the minima of the potential move one unit cell above the square pattern.<sup>8,9</sup> The motion is topologically protected, with the set of winding numbers around the fence points defining the topological invariants.

If  $\mathbf{H}_{\text{ext}}$  points in the direction of a fence point, the magnetic potential  $U$  is effectively one-dimensional with valleys along the direction perpendicular to  $\mathbf{H}_{\text{ext}}$ . For example, let the lattice vectors of the magnetic pattern point along  $x$  and  $y$ , Fig. 1(a).

The magnetic potential  $U$  exhibits deep valleys along  $x$ , Fig. 1(b), when  $\mathbf{H}_{\text{ext}}$  points along  $-y$ , Fig. 1(c). If  $\mathbf{H}_{\text{ext}}$  slightly deviates from the direction of a fence point, see modulation loop in Fig. 1(c), then secondary minima of  $U$  appear along the direction of the valleys, Fig. 1(b). The variation of the potential along the valley  $\delta U$  is much smaller than in the transversal direction  $\Delta U$ . In our experimental setup, we find  $\Delta U/\delta U \approx 10$ . Modulating the external field directions along a loop that encloses a fence point, Fig. 1(c), causes the minima of  $U$  to travel by one unit vector of the lattice upon completion of the loop. The frequency of the loop  $\omega$  can be chosen such that single colloids cannot follow the potential minimum on their own but doublets move in direction of the traveling minima. If a doublet is on a collision course with a single colloid, then the doublet can render the single colloid mobile and drive it through the potential valley, Fig. 1(a).

### 3 Results

In Fig. 2 we plot the speed of an isolated single colloid and that of an isolated doublet *versus* the driving angular frequency  $\omega$  of the modulation loop in  $\mathcal{C}$ . At low frequencies, lower than the topological critical frequency  $\omega_t$ , the motion is adiabatic and topologically protected. Singlets and doublets follow the potential minimum at all times. Hence, the displacement caused by a loop is topologically locked to the primitive lattice vector and particles move at the topological speed given by the lattice constant  $a$  times the frequency, *i.e.*,  $v_t = \omega a/2\pi$ . However, at higher frequencies  $\omega > \omega_t$  the speed drops below  $v_t$ , mostly due to viscous and adhesive forces impeding the motion. For singlets, the speed decreases with increasing frequency until the critical frequency  $\omega_c$  is reached. At  $\omega_c$  the isolated single

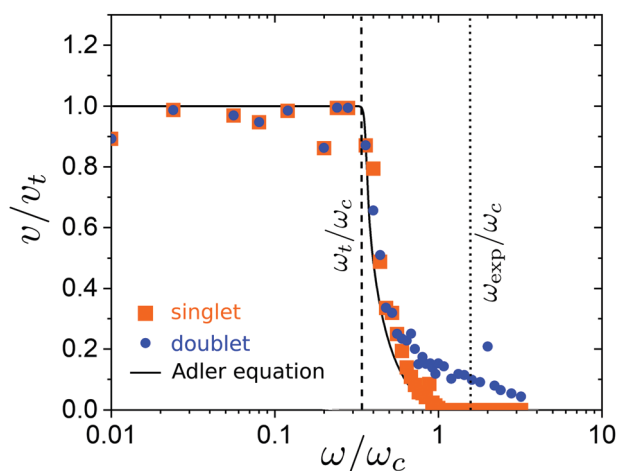


Fig. 2 Scaled magnitude of the velocity of singlets (orange squares) and doublets (blue circles) as a function of the scaled driving frequency. The black solid line is a fit of the singlet velocity using the generalized Adler eqn (1). The vertical lines indicate the scaled experimental frequency  $\omega_{\text{exp}}$  and the topological frequency  $\omega_t$  below which the motion is topologically protected.

colloids stop moving. The speed of the singlets is well described by a generalized Adler equation<sup>12</sup>

$$v/v_t = \begin{cases} 1 & \text{if } \omega \leq \omega_t \\ 1 - \sqrt{\frac{(\omega - \omega_t)((\omega_c - \omega)\omega_t + \omega\omega_c)}{(\omega_c - \omega_t)\omega^2}} & \text{if } \omega_t < \omega < \omega_c \\ 0 & \text{if } \omega \geq \omega_c \end{cases} \quad (1)$$

The force due to the potential acting on a doublet is roughly twice the force acting on a single colloidal particle. The viscous friction on the doublet, however, is less than twice the friction of a single colloid because of hydrodynamic interactions.<sup>13</sup> Hence, the doublet can still move at frequencies higher than the critical frequency of the singlets, and we have a regime

where the doublet moves while the singlet is at rest. The experiments are performed at an angular frequency of  $\omega \approx 52 \text{ s}^{-1} > \omega_c$ , such that singlets do not move, and doublets move with a speed of roughly one eighth of the topological speed ( $v_d/v_t \approx 0.125$ ), see Fig. 2.

In Fig. 3 we show a time sequence of microscope images showing the dynamics of the colloids. We distinguish single colloids (red) that are immobile from colloidal trains (green, cyan and yellow) consisting of one, two, and three doublets at the tail, and of one up to five single colloids at the front of the trains. The singlets and doublets in a train are well separated from each other by a primitive unit vector of the lattice. All trains move into the positive  $x$ -direction with the doublets pushing the singlets. Nothing particular happens to the cyan train with one doublet and one singlet moving through the field of view at the doublet speed  $v_d$ . The green train with one doublet and three singlets moves with half the doublet speed, Fig. 3(a) and (b), collects two further singlets, Fig. 3(c), and stalls, Fig. 3(d), until the two singlets close to the pushing doublets form a second doublet, Fig. 3(e). This increases the power of the train such that it resumes to move, Fig. 3(e) and (f) at the doublet speed. In Fig. 3(g) a third doublet is formed leaving only one singlet in the green train before it exits the field of view. Interestingly, when the green train passes the red singlets (sitting on the next track to the right) the front immobile red single colloid is mobilized and performs a single translation by one unit vector in the positive  $x$ -direction, compare the position of the red colloids next to the green train in Fig. 3(e) and (f). The yellow train originally consists of one doublet and two singlets, Fig. 3(a). It collects two further singlets, Fig. 3(b) and (c), and then moves as one doublet and four singlets train at a relatively slow speed  $v \approx 0.15v_d$  through the image. No further doublets are formed from the singlets of the yellow train as it moves. In Fig. 4 we plot the speed of a train as a function of both the number of singlets in front of the train and the number of doublets at its tail. A train with no doublet is immobile and a train with more than one doublet can push up

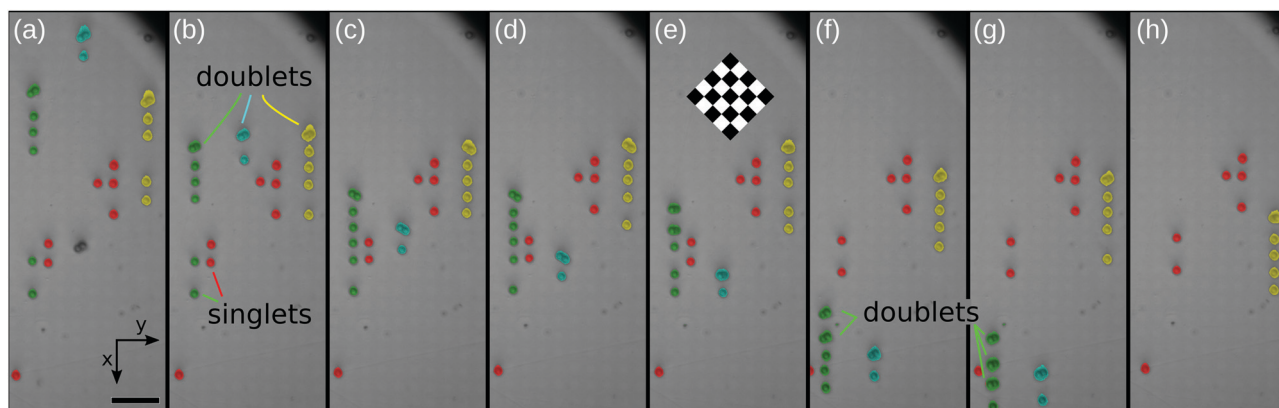


Fig. 3 Time sequence of microscope images of the pattern illustrating the motion of colloidal trains. Each train has been artificially colored differently. The images correspond to the times (a)  $t = 0 \text{ s}$ , (b)  $t = 8 \text{ s}$ , (c)  $t = 13 \text{ s}$  (d)  $t = 15 \text{ s}$  (e)  $t = 17 \text{ s}$  (f)  $t = 23 \text{ s}$  (g)  $t = 25 \text{ s}$  and (h)  $t = 30 \text{ s}$ . The period of one modulation loop is  $2\pi/\omega_{\text{exp}} \approx 0.12 \text{ s}$ . Scale bar is  $20 \mu\text{m}$ . A sketch of the pattern has been superimposed in (e). A video clip recorded at twenty frames per second showing the motion of trains and the non motion of singlets is provided in the ESI† (adfig3a.mp4). A second video clip (adfig3b.mp4) recorded at sixty frames per second shows a time-resolved slow motion of the doublet during the course of a few modulation loops.

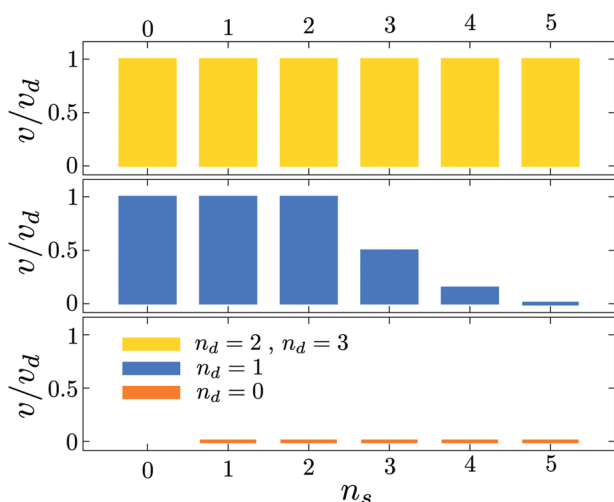


Fig. 4 Speed of the train (scaled with the speed of a doublet  $v_d$ ) versus the load, *i.e.* the number of singlets in the train  $n_s$ . Data for different numbers of doublets in front of the train:  $n_d = 0$  (orange),  $n_d = 1$  (blue),  $n_d = 2$  and 3 (yellow).

to five single colloids at the unloaded doublet speed. For one doublet we see a gradual transition from motion at the doublet speed  $v_d$  for trains with up to two singlets toward no motion for trains with five singlets.

Remarkably, none of the trains ever derails. This is due to the special properties of the confining colloidal potential which are inherited from the square pattern. In Fig. 5 we show the colloidal motion on a glass slide with no magnetic confining pattern. Doublets also move when performing a modulation loop without the magnetic pattern (albeit not by a unit vector) and singlets are generically at rest. However due to the absence of the confining potential, when one doublet moves onto a singlet, the singlet does not stay on track but is pushed to the side to let the doublet pass.

So far we have shown the coordinated motion of colloids in one direction. However, by changing the global orientation of the driving loop (winding around other fence points in  $\mathcal{C}$ ) we can force the doublet to move along any of the four symmetry directions of the magnetic pattern. Hence, the doublet-induced motion of single colloids can potentially be used to arbitrarily

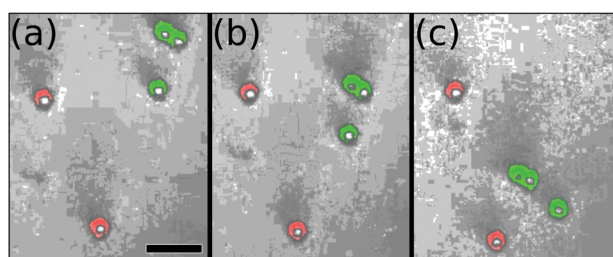


Fig. 5 Time sequence of microscope images showing a doublet (green) moving a singlet (green) out of its way. The other single colloids (red) remain at rest. Scale bar is 10  $\mu\text{m}$ . The images correspond to the times (a)  $t = 0$  s, (b)  $t = 2$  s, and (c)  $t = 4$  s. A video clip of the event recorded at twenty frames per second is provided in the ESI† (adfig5.mp4).

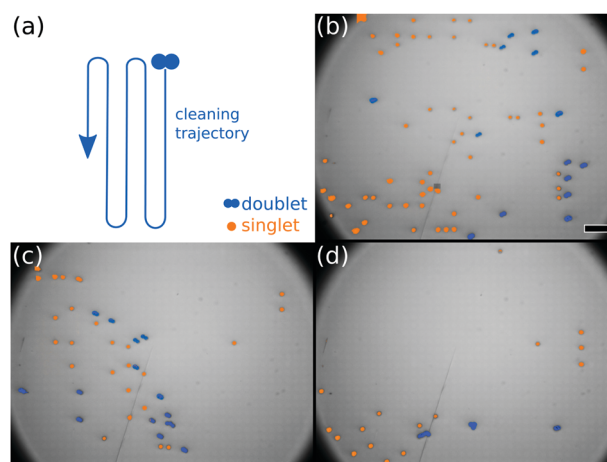


Fig. 6 Surface cleaning. (a) Schematic of the trajectory of a doublet. Sequence of microscope images showing the cleaning of an area from single colloids (orange) by meandering doublets (blue) taken at times  $t = 0$  (b),  $t = 2$  min (c), and  $t = 6$  min (d). The scale bar is 20  $\mu\text{m}$ . A video clip of the event is provided in the ESI† (adfig6.mp4).

set the position of the singlets across the pattern. A step in this direction is shown in Fig. 6 where a complex modulation loop is programmed to clean the surface of singlets.

## 4 Discussion

Our colloidal trains are immersed into a low Reynolds number liquid where the propulsion of shape changing objects is governed by the area enclosed by the loop in shape space of the object.<sup>14,15</sup> Swimmers are able to move by changing their shape. In contrast, our biomimetic colloidal trains are driven by the shape of the potential created by the pattern and the external field which creates the topological nature of this classical non-adiabatic phenomenon. We have shown in ref. 8, 9, 16–20 that, like other classical topological transport phenomena,<sup>21–27</sup> there exist similarities with quantum mechanical topological transport.<sup>28,29</sup>

## 5 Conclusion

We described the magnetic coupling between well separated colloids that self assemble a colloidal train consisting of magnetically driven colloidal doublets acting as the locomotive of the train and colloidal singlets acting as less powerful carriages. A magnetic pattern below the colloidal train provides two perpendicular sets of periodic railway tracks that can be accessed alternatively and that guide the trains. We showed how we can manipulate the colloidal singlets on those tracks *via* the doublets using magnetic modulation loops that wind around specific directions with a supercritical frequency. We achieve superior coordinated control over a large ensemble of single colloidal particles. Our work adds a new avenue toward the transport of colloidal particles with potential applications on lab on the chip devices and on drug delivery on colloidal carriers.

We demonstrated how long range many-body interactions between the well separated colloidal particles can help sustain

the topological nature of the transport up to higher frequencies of driving. Such speeding up comes in handy for lab-on-the-chip applications such as transporting loads from one place of a chip to another. Whether the doublet-induced motion of the singlets is caused by direct superadiabatic non-equilibrium interparticle interactions<sup>30</sup> or mediated by hydrodynamic interactions constitutes the subject of future studies.

## Author contributions

MMK, AdE, DdlH, & TMF designed and performed the experiment, and wrote the manuscript with input from all the other authors. MU & FS produced the magnetic film. AT, RH, IK, JG, ArE, DH, & MR performed the fabrication of the micromagnetic domain patterns within the magnetic thin film.

## Conflicts of interest

There are no conflicts to declare.

## References

- 1 R. Dreyfus, J. Baudry, M. L. Roper, M. Fermigier, H. A. Stone and J. Bibette, Microscopic artificial swimmers, *Nature*, 2005, **437**, 862.
- 2 A. Snezhko, M. Belkin, I. S. Aranson and W. K. Kwok, Self-Assembled Magnetic Surface Swimmers, *Phys. Rev. Lett.*, 2009, **102**, 118103.
- 3 K. J. Solis and J. E. Martin, Chevrons, filaments, spinning clusters and phase coexistence: emergent dynamics of 2- and 3-d particle suspensions driven by multiaxial magnetic fields, *Soft Matter*, 2017, **13**, 5676.
- 4 C. Bechinger, R. Di Leonardo, H. Löwen, C. Reichhardt, G. Volpe and G. Volpe, Active particles in complex and crowded environments, *Rev. Mod. Phys.*, 2016, **88**, 045006.
- 5 F. E. Fish, Kinematics of ducklings swimming in formation - consequences of position, *J. Exp. Zool.*, 1995, **273**, 1.
- 6 A. Snezhko and I. S. Aranson, Magnetic manipulation of self-assembled colloidal asters, *Nat. Mater.*, 2011, **10**, 698.
- 7 N. Casic, N. Quintero, R. Alvarez-Nodarse, F. G. Mertens, L. Jibuti, W. Zimmermann and T. M. Fischer, Propulsion efficiency of a dynamic self-assembled helical ribbon, *Phys. Rev. Lett.*, 2013, **110**, 168302.
- 8 D. de las Heras, J. Loehr, M. Lönne and T. M. Fischer, Topologically protected colloidal transport above a square magnetic lattice, *New J. Phys.*, 2016, **18**, 105009.
- 9 J. Loehr, D. de las Heras, M. Lönne, J. Bugase, A. Jarosz, M. Urbaniak, F. Stobiecki, A. Tomita, R. Huhnstock, I. Koch, A. Ehresmann, D. Holzinger and T. M. Fischer, Lattice symmetries and the topologically protected transport of colloidal particles, *Soft Matter*, 2017, **13**, 5044.
- 10 C. Chappert, H. Bernas, J. Ferré, V. Kottler, J.-P. Jamet, Y. Chen, E. Cambril, T. De-Volder, F. Rousseaux, V. Mathet and H. Launois, Planar patterned magnetic media obtained by ion irradiation, *Science*, 1998, **280**, 1919.
- 11 P. Kuświk, A. Ehresmann, M. Tekielak, B. Szymański, I. Sveklo, P. Mazalski, D. Engel, J. Kisielewski, D. Lengemann, M. Urbaniak, C. Schmidt, A. Maziewski and F. Stobiecki, Colloidal domain lithography for regularly arranged artificial magnetic out-of-plane monodomains in Au/Co/Au layers, *Nanotechnology*, 2011, **22**, 095302.
- 12 R. Adler, A study of locking phenomena in oscillators, *Proc. IRE*, 1946, **34**, 351.
- 13 The drag force on a train of  $N$  spheres of radius  $r$  scales as  $Nr/\ln(N)$ . See e.g. J. Happel and H. Brenner, *Low Reynolds number hydrodynamics*, Martinus Nijhoff Publishers, 1983, p. 156.
- 14 A. Shapere and F. Wilczek, Geometry of self-propulsion at low Reynolds number, *J. Fluid Mech.*, 1989, **198**, 557.
- 15 A. Shapere and F. Wilczek, Efficiency of self-propulsion at low Reynolds number, *J. Fluid Mech.*, 1989, **198**, 587.
- 16 J. Loehr, M. Lönne, A. Ernst, D. de las Heras and T. M. Fischer, Topological protection of multiparticle dissipative transport, *Nat. Commun.*, 2016, **7**, 11745.
- 17 A. M. E. B. Rossi, J. Bugase and Th. M. Fischer, Macroscopic Floquet topological crystalline steel and superconductor pump, *Europhys. Lett.*, 2017, **119**, 40001.
- 18 A. M. E. B. Rossi, J. Bugase, T. Lachner, A. Ernst, D. de las Heras and T. M. Fischer, Hard topological versus soft geometrical magnetic particle transport, *Soft Matter*, 2019, **15**, 8543.
- 19 H. Massana-Cid, A. Ernst, D. de las Heras, A. Jarosz, M. Urbaniak, F. Stobiecki, A. Tomita, R. Huhnstock, I. Koch, A. Ehresmann, D. Holzinger and T. M. Fischer, Edge transport at the boundary between topologically equivalent lattices, *Soft Matter*, 2019, **15**, 1539.
- 20 J. Loehr, D. de las Heras, A. Jarosz, M. Urbaniak, F. Stobiecki, A. Tomita, R. Huhnstock, I. Koch, A. Ehresmann, D. Holzinger and T. M. Fischer, Colloidal topological insulators, *Commun. Phys.*, 2018, **1**, 4.
- 21 M. C. Rechtsman, J. M. Zeuner, Y. Plotnik, Y. Lumer, D. Podolsky, F. Dreisow, S. Nolte, M. Segev and A. Szameit, Photonic Floquet topological insulators, *Nature*, 2013, **496**, 196–200.
- 22 M. Xiao, G. Ma, Z. Yang, P. Sheng, Z. Q. Zhang and C. T. Chan, Geometric phase and band inversion in periodic acoustic systems, *Nat. Phys.*, 2015, **11**, 240.
- 23 A. Murugan and S. Vaikuntanathan, Topologically protected modes in non-equilibrium stochastic systems, *Nat. Commun.*, 2017, **8**, 13881.
- 24 C. L. Kane and T. C. Lubensky, Topological boundary modes in isostatic lattices, *Nat. Phys.*, 2014, **10**, 39.
- 25 J. Paulose, B. G. Chen and V. Vitelli, Topological modes bound to dislocations in mechanical metamaterials, *Nat. Phys.*, 2015, **11**, 153.
- 26 L. M. Nash, D. Kleckner, A. Read, V. Vitelli, A. M. Turner and W. T. M. Irvine, Topological mechanics of gyroscopic metamaterials, *Proc. Natl. Acad. Sci. U. S. A.*, 2015, **112**, 14495.
- 27 S. D. Huber, Topological mechanics, *Nat. Phys.*, 2016, **12**, 621.
- 28 M. Z. Hasan and C. L. Kane, Colloquium: Topological insulators, *Rev. Mod. Phys.*, 2010, **82**, 3045.
- 29 S.-Q. Shen, *Topological insulators: Dirac equation in condensed matters*, Springer Science, and Business Media, 2013.
- 30 M. Schmidt and J. M. Brader, Power functional theory for Brownian dynamics, *J. Chem. Phys.*, 2013, **138**, 214101.



## Part III

---

# Methods



# Chapter 8

## Simulations

In all five publications of this thesis I have simulated the overdamped motion of magnetic colloidal particles. Here I summarize the most important details about these simulations. A common way to simulate a colloidal dispersion is the use of the *Langevin equation*[44]. It incorporates Brownian motion of particles caused by interactions with the medium they are surrounded with. It can be written as

$$m \frac{d^2 \mathbf{r}}{dt^2} = -\xi \frac{d\mathbf{r}}{dt} + \boldsymbol{\eta}(t),$$

where  $m$  is the mass of a particle,  $\xi$  is a dampening factor describing the Stoke's friction of the particle and  $\boldsymbol{\eta}(t)$  is a random force with Gaussian probability distribution, with a variance given by the fluctuation–dissipation theorem, representing the Brownian motion. Because the experiments are performed in an overdamped regime, we can neglect the left inertial part of the equation and obtain the differential equation for *Brownian dynamics*

$$\xi \frac{d\mathbf{r}}{dt} = \boldsymbol{\eta}(t).$$

In our case we have to add an additional magnetic force  $-\nabla V$  on the particles, so

$$\xi \frac{d\mathbf{r}}{dt} = -\nabla V + \boldsymbol{\eta}(t),$$

where  $V$  is a sum of potentials originating from interactions as described in the following.

We distinguish between two types of interactions. Pattern-particle interactions only act on the particle depending on its position and time, whereas particle-particle interactions also depend on the position all the other particles. The program flow of the simulation is shown in figure 8.1. After initialization, every simulation step consists of calculation of all the pattern-particle, interparticle and random forces, subsequent integration, and storing the results every  $n$  steps. After every step it is checked if a stop condition is fulfilled, otherwise the next step is executed.

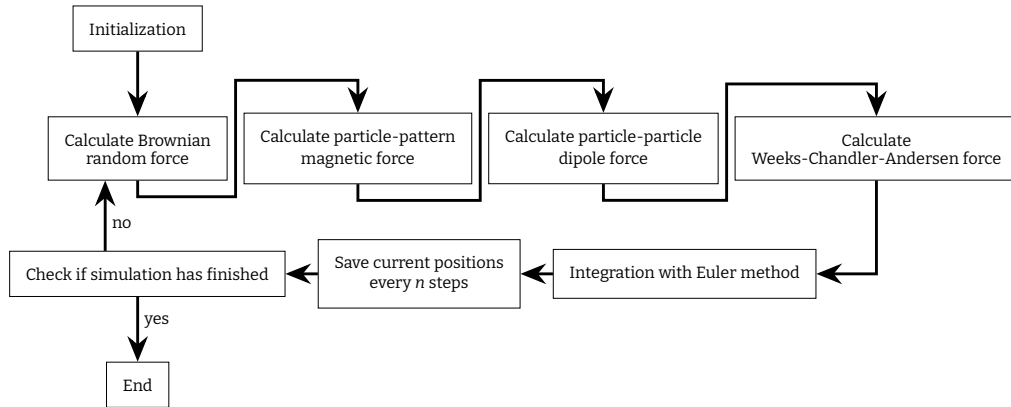


Figure 8.1: Schematic representation of the program flow.

## 8.1 Pattern representation

The magnetic field of the pattern does not depend on time and can therefore be computed before starting the simulations. For the patterns used in the experiments, it can be calculated for use in the simulations in different ways. If the distance between a periodic pattern and the particles is large compared to the pattern's period length, higher orders of the Fourier series of the pattern field can be neglected and the magnetic field of symmetric patterns can be approximated by the universal magnetic potential[3]. If the pattern is not periodic or the distance to the pattern is small, one can calculate the magnetic field at one point by direct integration. Because this is a numerically expensive calculation, the values are precalculated on a grid and interpolated either with linear or cubic spline interpolation when needed in the simulations. The precalculation is performed by a convolution of the pattern magnetization with a kernel which only depends on the height above the pattern. For periodic patterns this can be done using fast Fourier transform.

## 8.2 Pattern-particle interactions

The pattern field can now be used to calculate the magnetic force between particles and pattern. We make use of an effective particle potential being calculated as

$$U_{pp} \propto - (\mathbf{H}_{pat} + \mathbf{H}_{ext})^2$$

where  $\mathbf{H}_{pat}$  is the magnetic field of the pattern and  $\mathbf{H}_{ext}$  is an external magnetic field, both taken at the particle's position. We make use of an homogeneous

magnetic field, so that  $\mathbf{H}_{\text{ext}}(t)$  depends only on time, whereas  $\mathbf{H}_{\text{pat}}(\mathbf{r})$  depends only on the location of the particle. As a consequence, the effective particle potential varies with space and time.

The external field is of constant magnitude and we vary only its direction. Because in our case the external field is much stronger than the pattern field, the particle is magnetized in direction of the external field, so the potential can be approximated as

$$U_{\text{pp}}(\mathbf{r}, \mathbf{t}) \propto -\mathbf{H}_{\text{pat}}(\mathbf{r}) \cdot \mathbf{H}_{\text{ext}}(\mathbf{t}).$$

### 8.3 Dipole-dipole interactions

There is not only magnetic interaction between the pattern and the particles, but also between a pair of particles. This pair dipole interaction potential is

$$U_{\text{dd}}(\mathbf{r}) = \mathbf{m}' \cdot \frac{3(\mathbf{m} \cdot \mathbf{r})\mathbf{r} - |\mathbf{r}|^2\mathbf{m}}{4\pi|\mathbf{r}|^5}$$

for a particle with dipole moment  $\mathbf{m}'$  where  $\mathbf{r}$  is the vector to another particle with dipole moment  $\mathbf{m}$ .

### 8.4 Excluded volume interactions

As the dipole-dipole interactions can be attractive, we need a repulsive force to keep them separated to model the spherical particles used in the experiments. This force is derived from the Weeks-Chandler-Andersen potential, a modified Lennard-Jones potential[11]. It depends only on the distance  $r$  between two points and can be written in the form of

$$U_{\text{WCA}}(r) = \begin{cases} 4\epsilon \left( \left(\frac{\sigma}{r}\right)^{12} - \left(\frac{\sigma}{r}\right)^6 + \frac{1}{4} \right) & r \leq 2^{1/6}\sigma \\ 0 & r > 2^{1/6}\sigma \end{cases}$$

where  $\sigma$  is a measure of the minimum distance between the dipoles and  $\epsilon$  a characteristic energy determining the “hardness” of the modeled particle. As it is 0 for larger distances, it has to be calculated only below a certain distance, speeding up the simulations. We have to use such a soft potential, because a hard sphere potential leads to numerical instability when using Brownian dynamics simulations.

## 8.5 Thermal random force

We use a Mersenne Twister random generator[45] that generates random numbers  $r_1$  and  $r_2$  in the interval  $[0, 1)$ . The random force acting during one time step  $\delta t$  is then given by

$$\boldsymbol{\eta} = \sqrt{\frac{2k_B T \delta t}{\xi}} \sqrt{-2 \ln r_1} \begin{pmatrix} \cos(2\pi r_2) \\ \sin(2\pi r_2) \end{pmatrix},$$

such that the force distribution is Gaussian with a variance fulfilling the fluctuation dissipation theorem.

## 8.6 Particle Initialization

The particle's positions were initialized using custom programs for every case. For the bipeds the first particle was placed at the minimum  $z$ -position, the other particles were then stacked above in direction of the initial external magnetic field.

To initialize the timecrystals, the simulation for a unit cell was run isolated and the particles then repeatedly placed by shifting the positions by lattice vectors.

Further specific details on the simulations are given in my publications, respectively.

# Chapter 9

## Transcription Matrix

In publication 3 I wrote a program that finds a complex loop transporting bipeds of different lengths along predefined paths. The problem of finding the paths of different bipeds for a particular loop is a simple geometric problem. However, the inverse problem is more involved. A short version of its solution is given in publication 3. Here comes the extended version of this problem.

Finding the right modulation for transporting bipeds of different lengths in the directions we want them to move is not easy. In the case of periodic fourfold symmetric pattern with the experiments performed at universal height, the fence consists only out of points at the equator of the control space.

The  $n$  different lengths of the bipeds we are using are given by

$$B = \{b_1, b_2, \dots, b_n\}.$$

We then define

$$d_b = \lfloor b/a \rfloor$$

needed for calculating the number of  $4(2d_b + 1)$  fence points for a specific  $b$ , where  $\lfloor \dots \rfloor$  indicates rounding towards 0. This leads to the set  $D_b$  which is used to define the azimuthal positions of the fence points  $\Phi_b^{(m)}$  at the equator  $\vartheta = \pi/2$  of the control space:

$$D_b = \{0, 1, \dots, d_b\}$$

$$\Phi_b^{(m)} = \{\arcsin(\pm i \cdot a/b) + m\pi/2 \mid i \in D_b\}, m = 0, 1, 2, 3.$$

where  $\mathbf{R}_{\pi/2}^m \cdot \mathbf{a}_1$  denotes the resulting transport direction when encircling one of the the fence points  $(\vartheta = \pi/2, \phi)$  with  $(\phi \in \Phi_b^{(m)})$  in the mathematic positive sense. The vector  $\mathbf{a}_1$  is the primitive unit vector of the pattern and  $\mathbf{R}_{\pi/2}$  is a rotation matrix by the angle  $\pi/2$ .

Fence points in the unidirectional transcription space arise from cuts of fence lines in the polydirectional transcription space as dicussed in my publication 3

where they form a grid of fence lines characterized by grid numbers. We can combine the azimuthal coordinates  $\Phi_b^{(m)}$  of all fence points for all biped lengths in  $B$  and for all grid numbers into the set:

$$\Phi_F = \bigcup_{m=0,1,2,3} \bigcup_{b \in B} \Phi_b^{(m)}$$

Neighboring fence coordinates are separated by

$$\delta_d(\phi_1, \phi_2) = \phi_2 - \phi_1.$$

To rule out loops with low robustness  $\delta_d < 2\Delta$ , we define the set of neighbors with sufficient clearance:

$$S = \{(\phi_1, \phi_2) \mid (\phi_1 < \phi_2) \wedge (\delta_d(\phi_1, \phi_2) > 2\Delta) \wedge (\phi_1, \phi_2 \in (\Phi_F \cup \{2\pi\})) \wedge (\nexists \phi \in \Phi_F : \phi_1 < \phi < \phi_2)\}$$

Our trial loops in control space are allowed to cross the equator exactly between these neighbors and the set of allowed crossing azimuthal coordinates is:

$$\Phi_c = \{(\phi_1 + \phi_2)/2 \mid (\phi_1, \phi_2) \in S\}$$

The set of allowed trial loops

$$L_{\text{trial}} = \{\mathcal{L}_C(\phi_d, \phi_u) \mid (\phi_d, \phi_u \in \Phi_c)\}$$

with loops  $\mathcal{L}_C(\phi_d, \phi_u)$  that start at the north pole, cross to the southern hemisphere at the coordinate  $\phi_d$ , cross back to the northern hemisphere via the coordinate  $\phi_u$ , and return to the north pole. For each loop  $\mathcal{L}_C(\phi_d, \phi_u)$  and each biped  $b \in B$  and fence point coordinate  $\phi \in \Phi_b^{(m)}$  we define the winding number  $w_b^{(m)}(\mathcal{L}_C(\phi_d, \phi_u), \phi)$  around this particular fence point. The displacement of a biped of length  $b$  is then given by

$$\Delta \mathbf{r}_b(\mathcal{L}_C(\phi_d, \phi_u)) = \sum_m \sum_{\phi \in \Phi_b^{(m)}} w_b^{(m)}(\mathcal{L}_C(\phi_d, \phi_u), \phi) \mathbf{R}_{\pi/2}^m \cdot \mathbf{a}_1$$

We sort all loops in  $L_{\text{trial}}$  into a numbered set of loops  $\mathcal{L}_{C,i}, i = 1 \dots |L_{\text{trial}}|$ . We can now write a matrix containing all resulting integer trial displacements in units of  $a$  as

$$\frac{1}{a} \mathbf{R} = \frac{1}{a} \begin{pmatrix} \Delta \mathbf{r}_{b_1}(\mathcal{L}_{C,1}) & \Delta \mathbf{r}_{b_1}(\mathcal{L}_{C,2}) & \dots & \Delta \mathbf{r}_{b_1}(\mathcal{L}_{C,|L_{\text{trial}}|}) \\ \Delta \mathbf{r}_{b_2}(\mathcal{L}_{C,1}) & \Delta \mathbf{r}_{b_2}(\mathcal{L}_{C,2}) & \dots & \Delta \mathbf{r}_{b_2}(\mathcal{L}_{C,|L_{\text{trial}}|}) \\ \vdots & \vdots & \ddots & \vdots \\ \Delta \mathbf{r}_{b_{|B|}}(\mathcal{L}_{C,1}) & \Delta \mathbf{r}_{b_{|B|}}(\mathcal{L}_{C,2}) & \dots & \Delta \mathbf{r}_{b_{|B|}}(\mathcal{L}_{C,|L_{\text{trial}}|}) \end{pmatrix}.$$

The resulting matrix has  $|L_{\text{trial}}|$  columns and  $2|B|$  rows.

Our target integer displacement in units of  $a$  for each biped is

$$\frac{1}{a}\Delta\mathbf{r}^{\text{target}} = \frac{1}{a} \begin{pmatrix} \Delta\mathbf{r}_{b_1}^{\text{target}} \\ \Delta\mathbf{r}_{b_2}^{\text{target}} \\ \vdots \\ \Delta\mathbf{r}_{b_{|B|}}^{\text{target}} \end{pmatrix}$$

We are looking for a target loop

$$\mathcal{L}_{\mathcal{C},\text{target}} = \mathcal{L}_{\mathcal{C},1}^{w_1^{\text{target}}} * \mathcal{L}_{\mathcal{C},2}^{w_2^{\text{target}}} * \dots * \mathcal{L}_{\mathcal{C},|L_{\text{trial}}|}^{w_{|L_{\text{trial}}|}^{\text{target}}}$$

that is a concatenation of all trial loops  $\mathcal{L}_{\mathcal{C},i}$  with integer winding numbers  $w_i^{\text{target}}$  that produces our target displacement  $\Delta\mathbf{r}^{\text{target}}$ . The target winding numbers are the solutions to the equation

$$\frac{1}{a}\mathbf{R} \cdot \mathbf{w}^{\text{target}} = \frac{1}{a}\Delta\mathbf{r}^{\text{target}} \quad (9.1)$$

where

$$\mathbf{w}^{\text{target}} = \begin{pmatrix} w_1^{\text{target}} \\ w_2^{\text{target}} \\ \vdots \\ w_{|L_{\text{trial}}|}^{\text{target}} \end{pmatrix}.$$

Since the vector components of  $\mathbf{w}^{\text{target}}$  are winding numbers, the solution to the previous equation must be with a vector  $\mathbf{w}^{\text{target}} \in \mathbb{Z}^{|L_{\text{trial}}|}$  that contains only integer vector components. Since the entries of  $\mathbf{R}/a$  and  $\Delta\mathbf{r}^{\text{target}}/a$  are all integers,  $\det(\mathbf{R}/a)\mathbf{R}^{-1} \cdot \Delta\mathbf{r}^{\text{target}} = \det(\mathbf{R}/a)\mathbf{w}^{\text{target}}$  contains only integer numbers such that there is always a rescaled solution of the target motion on a larger scale. The solution on the smallest scale is  $\det(\mathbf{R}/a)\mathbf{w}^{\text{target}}/\text{gcd}$  where  $\text{gcd}$  is the greatest common divisor of all integer entries.

As this solution of equation (9.1) using linear algebra generally does not give an optimal integer solution to the problem, it requires the formulation of a so called *Integer Linear Program* (ILP) which is a linear optimization problem with integer solutions[46, 47]. Any ILP can be written in the form

$$\max_{\mathbf{x} \in \mathbb{Z}^n} \{\mathbf{c}^T \cdot \mathbf{x} | (\mathbf{A} \cdot \mathbf{x} \leq \mathbf{b}) \wedge (\mathbf{x} \geq \mathbf{0})\}$$

where  $\mathbf{c}^T$  is a transposed vector containing the objective coefficients,  $\mathbf{A}$  a coefficient matrix forming the linear conditions together with the coefficient vector  $\mathbf{b}$  and  $\mathbf{x}$  is the solution. All inequalities are applied component-by-component. To write our optimization problem for finding the lowest number of loops in this form we will first describe it in a non-standard form and then transform it to the form above to show that it is indeed an ILP.

The condition we have to fulfil is equation (9.1) from above so we can write our optimization problem as

$$\min_{\mathbf{w} \in \mathbb{Z}^n} \left\{ \sum_{i=1}^{|L_{\text{trial}}|} w_i \mid (\mathbf{R} \cdot \mathbf{w} = \Delta \mathbf{r}) \wedge (\mathbf{w} \geq \mathbf{0}) \right\}.$$

To convert the equal sign to the general inequality form, we can create a matrix  $\mathbf{A}$  out of  $\mathbf{R}$  and a vector  $\mathbf{b}$  out of  $\Delta \mathbf{r}$ . If we have an example equality  $u = v$ , we can make a set of two inequalities ( $u \leq v, -u \leq -v$ ) describing the same condition. We can do the same for  $\mathbf{R}$  and  $\Delta \mathbf{r}$  and get

$$\mathbf{A} = \begin{pmatrix} \mathbf{R} \\ -\mathbf{R} \end{pmatrix}$$

$$\mathbf{b} = \begin{pmatrix} \Delta \mathbf{r} \\ -\Delta \mathbf{r} \end{pmatrix}.$$

To minimize instead of maximize the number of loops every objective coefficient is  $-1$

$$c_i = -1, i = 1, \dots, |L_{\text{trial}}|.$$

Now we have our problem in our desired form

$$\max_{\mathbf{w} \in \mathbb{Z}^n} \{ \mathbf{c}^T \cdot \mathbf{w} \mid (\mathbf{A} \cdot \mathbf{w} \leq \mathbf{b}) \wedge (\mathbf{w} \geq \mathbf{0}) \}$$

and can be passed to a standard ILP solver such as *GLPK*[48]. This software uses a variety of heuristic algorithms to find an optimal integer solution in a short time.

## Part IV

---

# Summary



# Summary

This cumulative thesis studies the topological transport of colloidal particles on top of periodic magnetic patterns for various different situations. My part of this collaborative work was the simulation of the colloidal motion and the computation of bifurcation points and fences on various patterns of different symmetry. Some of my simulations have not yet been verified by experiments, but most of them have been proven to be correct. I have investigated several interesting aspects of the topological transport of colloids:

On a hexagonal magnetic pattern with flower shaped, upward magnetized domains three particles per unit cell adiabatically respond by performing a topological rearrangement within one flower shaped domain. If the dipolar interactions between the paramagnetic colloidal particles are of the right strength, there are 6 bifurcation or fence points in the control space such that a trivial loop with zero winding number causes a trivial i.e. harmonic response of the three particle conformation. If however one winds around one of the fence points, a subharmonic response of the particle conformation with a response period of double the driving period occurs no matter at which adiabatic frequency the system is driven. When we arrange three particles per unit cell in a periodic spatial way, we discover all kinds of space-time crystalline responses. We distinguish the flower shaped domains by the orientation of the lobes of the flower. Orientations of the lobes in the direction of the primitive unit vectors suppresses time crystalline response, while orientation of the lobes toward the primitive reciprocal unit vectors of the lattice supports the formation of space time crystals. In the first case, time crystals might be totally suppressed in the bulk but supported at the edge. In the latter case we observe topological transitions from a ferromagnetic toward an antiferromagnetic time crystalline order.

In simulations of an increasing number of particles per unit cell in a related hexagonal magnetic pattern, we can show that the number of bifurcation points in control space increases with the number of particles per unit cell. In the thermodynamic limit with an infinite number of particles per unit cell, we find a geometric behavior of the transport displacement per loop, while for small number per unit cell the transport behavior is with topological steps. The step width of the transport decreases with the number of particles while the step

number per loop increases. This is a very different way of loosing the topological aspects of the transport as compared to the topological steps in the Quantum Hall effect that changes toward geometrical due to thermal excitations.

In a strong external magnetic field, single colloidal particles assemble into bipeds due to dipolar interactions. The bipeds are rods of  $n = 2 - 18$  beads that walk across a square pattern with their two ends, which for obvious reasons we call their feet. Since the biped orientation is enslaved to the external field, the control space together with their fence points and bifurcation points are transferred to the polyglot transcription space of the end to end vectors  $\mathbf{b}$  of the bipeds, a three dimensional Cartesian space built from concentric spherical shells for the individual bipeds of fixed length. Fence points from a single bead are transferred to fence lines along the  $b_x$  and  $b_y$  axes in polyglot transcription space and they are periodically continued with the period of the lattice in action space. Control loops are transferred into control cones. The intersection of such a cone with a spherical shell of radius of a particular biped length is the transcribed loop for that particular biped. The winding numbers of the transcribed loop around the transcribed fence lines defines the translation of the walking biped in action space. The geometric simplicity of this construction allows the inversion of the relation between control loop and the translation of a selected set of bipeds. For any desired set of translation of loops, my computer code can find a compact and robust loop that will cause these desired translations. We have preprogrammed several tasks on the computer and shown that the bipeds are transported exactly the way as wanted if the set of biped lengths is almost two orders of magnitude less than the number of computer languages in the polyglot challenge. The walking of bipeds on fourfold and sixfold lattices can be described in different gauges. We used the center of mass gauge for understanding the topology of the problem and the instantaneous center of rotation gauge to decompose the motion into passive sliding and active walking. The active walking is a continuous function of the length of the biped, while the passive sliding is discontinuous. The walking of bipeds on square patterns is adiabatic, while on hexagonal patterns irreversible ratchet jumps interrupt the adiabatic character of the walking for half of the possible driving loops. At higher speeds, the biped walking remains topological but with some of the windings no longer being executed. Ultimately, at very high speeds of driving the walking of the bipeds ceases completely. Passive motion stops prior to active motion when driving at non-adiabatic speeds. Single colloids stop moving if not assisted by active bipeds. When the load of one biped pushing several single colloidal particles through a Goldstone valley surmounts the pushing capacity of a biped, single colloidal particles right in front of the pushing bipeds are compressed to form further bipeds that help pushing.

# Bibliography

1. Hoffmann. *Modern magic* American ed. (George Routledge and Sons, New York, 1885).
2. M. Nakahara. *Geometry, Topology and Physics* (CRC Press, 2018).
3. J. Loehr, D. de las Heras, M. Loenne, J. Bugase, A. Jarosz *et al.* Lattice symmetries and the topologically protected transport of colloidal particles. *Soft Matter* **13**, 5044–5075 (2017).
4. G. Fonnum, C. Johansson, A. Molteberg, S. Mørup and E. Aksnes. Characterisation of Dynabeads® by magnetization measurements and Mössbauer spectroscopy. *Journal of Magnetism and Magnetic Materials* **293**, 41–47 (2005).
5. C. Chappert, H. Bernas, J. Ferré, V. Kottler, J.-P. Jamet *et al.* Planar patterned magnetic media obtained by ion irradiation. *Science* **280**, 1919–1922 (1998).
6. M. Urbaniak, P. Kuświk, Z. Kurant, M. Tekielak, D. Engel *et al.* Domain-wall movement control in Co/Au multilayers by He<sup>+</sup>-ion-bombardment-induced lateral coercivity gradients. *Physical Review Letters* **105**, 067202 (2010).
7. P. Kuświk, A. Ehresmann, M. Tekielak, B. Szymański, I. Sveklo *et al.* Colloidal domain lithography for regularly arranged artificial magnetic out-of-plane monodomains in Au/Co/Au layers. *Nanotechnology* **22**, 095302 (2011).
8. A. Jarosz, D. Holzinger, M. Urbaniak, A. Ehresmann and F. Stobiecki. Manipulation of superparamagnetic beads on patterned Au/Co/Au multilayers with perpendicular magnetic anisotropy. *Journal of Applied Physics* **120**, 084506 (2016).
9. C. L. Kane and E. J. Mele. Z<sub>2</sub> topological order and the quantum spin Hall effect. *Physical Review Letters* **95**, 146802 (2005).
10. M. Z. Hasan and C. L. Kane. Colloquium: Topological insulators. *Reviews of Modern Physics* **82**, 3045–3067 (2010).
11. J. D. Weeks, D. Chandler and H. C. Andersen. Role of repulsive forces in determining the equilibrium structure of simple liquids. *J. Chem. Phys.* **54**, 5237–5247 (1971).

## Bibliography

12. J. Happel and H. Brenner. *Low Reynolds number hydrodynamics* (Springer Netherlands, 1981).
13. W. A. Marrison. The Evolution of the Quartz Crystal Clock. *Bell System Technical Journal* **27**, 510–588 (1948).
14. A. Shapere and F. Wilczek. Classical time crystals. *Phys. Rev. Lett.* **109**, 160402 (2012).
15. N. Yao, A. Potter, I.-D. Potirniche and A. Vishwanath. Discrete time crystals: rigidity, criticality, and realizations. *Physical Review Letters* **118**, 030401 (2017).
16. N. Y. Yao, C. Nayak, L. Balents and M. P. Zaletel. Classical discrete time crystals. *Nat. Phys.* **16**, 438–447 (2020).
17. L. Oberreiter, U. Seifert and A. C. Barato. Subharmonic oscillations in stochastic systems under periodic driving. *Physical Review E* **100**, 012135 (2019).
18. F. Wilczek. Quantum time crystals. *Phys. Rev. Lett.* **109**, 160401 (2012).
19. J. Zhang, P. W. Hess, A. Kyprianidis, P. Becker, A. Lee *et al.* Observation of a discrete time crystal. *Nature* **543**, 217–220 (2017).
20. H. Keßler, P. Kongkhambut, C. Georges, L. Mathey, J. G. Cosme *et al.* Observation of a dissipative time crystal. *Phys. Rev. Lett.* **127**, 043602 (2021).
21. T. L. Heugel, M. Oscity, A. Eichler, O. Zilberberg and R. Chitra. Classical many-body time crystals. *Phys. Rev. Lett.* **123**, 124301 (2019).
22. T. Prosen. Time evolution of a quantum many-body system: Transition from integrability to ergodicity in the thermodynamic limit. *Physical Review Letters* **80**, 1808–1811 (1998).
23. T. Prosen. Ergodic properties of a generic nonintegrable quantum many-body system in the thermodynamic limit. *Physical Review E* **60**, 3949–3968 (1999).
24. S. Choi, J. Choi, R. Landig, G. Kucsko, H. Zhou *et al.* Observation of discrete time-crystalline order in a disordered dipolar many-body system. *Nature* **543**, 221–225 (2017).
25. J. Rovny, R. L. Blum and S. E. Barrett. Observation of discrete-time-crystal signatures in an ordered dipolar many-body system. *Physical Review Letters* **120**, 180603 (2018).
26. K. Sacha and J. Zakrzewski. Time crystals: a review. *Reports on Progress in Physics* **81**, 016401 (2017).
27. K. Sacha. *Time Crystals* (Springer International Publishing, 2020).

28. K. Sacha. *Comment on “Adiabatic and irreversible classical discrete time crystals”* [Online; accessed 16-November-2022]. [https://scipost.org/submissions/2203.04063v1/#comment\\_id2423](https://scipost.org/submissions/2203.04063v1/#comment_id2423).
29. R. Aldrovandi and J. G. Pereira. *An Introduction to Geometrical Physics* (WORLD SCIENTIFIC, 2016).
30. S. Weinberg. Recent progress in gauge theories of the weak, electromagnetic and strong interactions. *Reviews of Modern Physics* **46**, 255–277 (1974).
31. H. Weyl. Elektron und Gravitation. I. *Zeitschrift für Physik* **56**, 330–352 (1929).
32. A. Shapere and F. Wilczek. Geometry of self-propulsion at low Reynolds number. *Journal of Fluid Mechanics* **198**, 557 (1989).
33. A. Shapere and F. Wilczek. Efficiencies of self-propulsion at low Reynolds number. *Journal of Fluid Mechanics* **198**, 587 (1989).
34. S.-Q. Shen. *Topological Insulators* (Springer Berlin Heidelberg, 2012).
35. J. von Bergmann and H. von Bergmann. Foucault pendulum through basic geometry. *American Journal of Physics* **75**, 888–892 (2007).
36. L. Mangiarotti and G. A. Sardanashvily. *Gauge Mechanics* (WORLD SCIENTIFIC, 1998).
37. E. Noether. Invariante Variationsprobleme. *Nachrichten von der Gesellschaft der Wissenschaften zu Göttingen, Mathematisch-Physikalische Klasse* **1918**, 235–257 (1918).
38. K. v. Klitzing, G. Dorda and M. Pepper. New method for high-accuracy determination of the fine-structure constant based on quantized Hall resistance. *Physical Review Letters* **45**, 494–497 (1980).
39. M. Kohmoto. Topological invariant and the quantization of the Hall conductance. *Annals of Physics* **160**, 343–354 (1985).
40. G. Nachtwei. Breakdown of the quantum Hall effect. *Physica E: Low-dimensional Systems and Nanostructures* **4**, 79–101 (1999).
41. “Add a language to a polyglot” on StackExchange [Online; accessed 16-November-2022]. <https://codegolf.stackexchange.com/questions/102370/add-a-language-to-a-polyglot/250674%5C#250674>.
42. H. Massana-Cid, A. Ernst, D. de las Heras, A. Jarosz, M. Urbaniak *et al.* Edge transport at the boundary between topologically equivalent lattices. *Soft Matter* **15**, 1539–1550 (2019).

## Bibliography

43. J. Loehr, M. Loenne, A. Ernst, D. de Las Heras and T. M. Fischer. Topological protection of multiparticle dissipative transport. *Nat. Commun.* **7**, 11745 (2016).
44. D. S. Lemons and A. Gythiel. Paul Langevin's 1908 paper "On the Theory of Brownian Motion" ["Sur la théorie du mouvement brownien", *C. R. Acad. Sci. (Paris)* **146**, 530–533 (1908)]. *American Journal of Physics* **65**, 1079–1081 (1997).
45. M. Matsumoto and T. Nishimura. Mersenne twister: a 623-dimensionally equidistributed uniform pseudo-random number generator. *ACM Trans. Model. Comput. Simul.* **8**, 3–30 (1998).
46. G. B. Dantzig. Reminiscences about the origins of linear programming. *Operations Research Letters* **1**, 43–48 (1982).
47. R. E. Gomory. in *50 Years of Integer Programming 1958-2008* 77–103 (Springer Berlin Heidelberg, 2009).
48. *GNU Linear Programming Kit* [Online; accessed 16-November-2022]. <https://www.gnu.org/software/glpk/glpk.html>.